Description of GOSAT-GW AMSR3

Level 1R and Geophysical Data Retrieval Algorithms

Japan Aerospace Exploration Agency
Earth Observation Research Center
June 30, 2026

Chapter 1. Level 1R

Chapter 2. Level 2 (Integrated Water Vapor and Cloud Liquid Water)

Chapter 3. Level 2 (Precipitation: Rainfall)

Chapter 4. Level 2 (Precipitation: Snowfall)

Chapter 5. Level 2 (Sea Surface Temperature)

Chapter 6. Level 2 (Sea Surface Wind Speed)

Chapter 7. Level 2 (All-weather Sea Surface Wind)

Chapter 8. Level 2 (Sea Ice Concentration)

Chapter 9. Level 2 (High Resolution Sea Ice Concentration)

Chapter 10. Level 2 (Snow Depth)

Chapter 11. Level 2 (Soil Moisture)

Chapter 12. Level 3 (Sea Ice Motion Vector)

Chapter 1.

Description of the GOSAT-GW AMSR3

Level-1R Algorithm

Japan Aerospace Exploration Agency

Earth Observation Research Center

Mitsubishi Electric Software Co., Ltd.

Table of Contents

1. Introduction 1-3
2. Overview 1-3
3. Correction of Brightness Temperatures Using an Antenna Pattern-Matching Technique 1-4
   3.1. Theory 1-4
   3.2. Possible Random Error Included in TB 1-6
4. Implementation 1-7
   4.1. Antenna Pattern 1-7
   4.2. Geometry 1-9
   4.3. Smoothing Factor Calculation 1-9

1. Introduction

This document describes the processing implemented in the AMSR3 Level-1R procedure that matches the spatial resolution of brightness temperatures and aligns the observation center positions across frequency channels.

2. Overview

In the AMSR3 Level-1R product, brightness temperatures are provided with spatial resolutions matched to the equivalent frequencies of 6.9 GHz, 10.65 GHz, 23.8 GHz, and 36.42 GHz, along with supplementary information. In the Level-1R product, the brightness temperatures are converted in terms of spatial resolution and observation location at the frequencies listed in Table 2-1.

Table 2-1 Frequencies for which the spatial resolution is modified in the Level-1R product

-	FOV06	FOV10	FOV23	FOV36
6.925G V/H	☆			
7.3G V/H	○			
10.25G V/H	○	○		
10.65G V/H	○	☆		
18.7G V/H	○	○	○	
23.8G V/H	○	○	☆	
36.42G V/H	○	○	○	☆
89.0G V/H	○	○	○	○
165.5G V			○	○
183.3±3G V			○	○
183.3±7G V			○	○
spatial resolution (FOV)	6.925GHz-equivalent	10.65GHz-equivalent	23.8GHz-equivalent	36.42GHz-equivalent
observation center position	89GHz A-scan odd-points	89GHz A-scan odd-points	89GHz A-scan odd-points	89GHz A-scan odd-points

☆：The spatial resolution is matched to that of the target frequency, and the observation center position is aligned with the 89 GHz A-scan odd points.

○：The spatial resolution is set to the antenna pattern of the target frequency, while the observation position is aligned with the 89 GHz A-scan odd points.

3. Correction of Brightness Temperatures Using an Antenna Pattern-Matching Technique

3.1. Theory

A receiving antenna FOV, i.e., a receiving antenna pattern, is not spatially uniform as its sensitivity varies according to the position. For simplicity, we assumed that a receiving antenna had a sufficiently narrow main lobe so that its pattern was formed on a 2-D (xy) plane. First, the brightness temperature T_B with a receiving antenna pattern G is expressed as

$$T_B = \iint G(x,y)\, T_B(x,y)\, dxdy \equiv \int_S G(\rho) T_B(\rho) \tag{1}$$

where $G(x,y) \equiv G(\rho)$ is the antenna sensitivity at a position $(x,y) \equiv \rho$ and $T_B(x,y) \equiv T_b(\rho)$ is the brightness temperature at ρ on the 2-D plane. For AMSR3, this 2-D plane corresponds to the Earth's surface observed through the atmosphere. Therefore, $T_b(\rho)$ includes the contributions from both the Earth's surface at ρ and the atmosphere between ρ and AMSR3. $G(\rho)$ is the normalized gain value of the antenna, such that

$$\int_S G(\rho)\, dS = 1. \tag{2}$$

The receive antenna pattern G is approximately an elliptical Gaussian distribution when projected onto the Earth's surface, but its center position and azimuth angle vary at each observation point.

If the antenna pattern at each observation point is denoted as G_i(i=1,...,N), the measured brightness temperature T_{B_i} can be expressed as follows.

$$T_{Bi} = \int_S G_i(\rho) T_B(\rho)\, dS \tag{3}$$

Meanwhile, the brightness temperature $\hat{T}_B$ corresponding to an arbitrarily defined target antenna pattern $F(\rho)$ can be expressed as follows.

$$\hat{T}_B = \int_S F(\rho) T_B(\rho)\, dS \tag{4}$$

where

$$\int_S F(\rho)\, dS = 1 \tag{5}$$

Under these assumptions, the synthesized brightness temperature$\hat{T}_B$ is generated by combining the individual brightness temperatures T_{Bi} using appropriate weighting coefficients a_i.

$$\hat{T}_B = \sum_{i=1}^{N} a_i T_B$$

(6)

$$= \sum_{i=1}^{N} a_i \left(\int_S G_i(\rho) T_B(\rho) dS \right)$$

(7)

a_i is used to compute the synthesized brightness temperature $\hat{T}_B$ from the individual brightness temperatures T_{Bi}. Focusing on the sum of $a_i G_i(\rho)$ at ρ,(7) can be rewritten as

$$\hat{T}_B = \int_S \left(\sum_{i=1}^{N} a_i G_i(\rho) \right) T_B(\rho) dS.$$

(8)

The weighting coefficient vector $a = (a_1, \ldots, a_N)$ is determined so as to satisfy

$$\sum_{i=1}^{N} a_i = 1.$$

(9)

From (4) and (7), the ideal a also satisfies the following condition.

$$F(\rho) - \sum_{i=1}^{N} a_i G_i(\rho) = 0$$

(10)

For any ρ, (10) should hold (i.e., this implies that F is perfectly reproduced by G_is.). However, such coefficients a do not necessarily exist in general; therefore, in practice, the coefficients a are chosen so as to minimize the squared L2 norm of the residual (the left-hand side of (10)), referred to as the $Fit\ Error$, defined as

$$Fit\ Error = \int_S \left(F(\rho) - \sum_{i=1}^{N} a_i G_i(\rho) \right)^2 dS.$$

(11)

The Backus-Gilbert method calculates the coefficient vector a that minimizes the $Fit\ Error$ while suppressing large coefficient values. The resulting coefficient vector is given by

$$a = \boldsymbol{V}^{-1} \left[\boldsymbol{v} + \left(\frac{1 - \boldsymbol{u}^T \boldsymbol{V}^{-1} \boldsymbol{v}}{\boldsymbol{u}^T \boldsymbol{V}^{-1} \boldsymbol{u}} \right) \boldsymbol{u} \right]$$

(12)

where u and v are vectors of length N and

$$\boldsymbol{V} = \boldsymbol{G} + \kappa \boldsymbol{I} \quad (13)$$

$$u_i = \iint_S G_i(\rho)\, dS \equiv 1 \quad (14)$$

$$v_i = \iint_S G_i(\rho)\, F(\rho) dS \tag{15}$$

$$G_{ij} = \iint_S G_i(\rho)\, G_j(\rho) dS \tag{16}$$

Here, $\boldsymbol{V}$ and $\boldsymbol{G}$ are square matrices of size $N \times N$, and **I** represents an identity matrix. The elements u_i are always equal to 1 according to (2). The element v_i (G_{ij}) represents the overlap between G_i and $\boldsymbol{F}$ (G_i and G_j). The parameter κ is a factor controlling the smoothness of a, ranging from 0 to ∞. For example, when $\kappa \to \infty$, the variation in a is completely smoothed with equal a_i values. For a given κ, the vector a that minimizes the Fit Error is calculated by (12). The primary requirement when setting κ is the minimization of the *Fit Error*. κ is referred to as the *Smoothing Factor*.

In addition, while a_i is always positive ($a_i \to 1/N$) when $\kappa \to \infty$, a_i can be positive or negative as $\kappa \to 0$. For example, G_{k-1} and G_{k+1} are located on either side of G_k almost overlapping it. When κ allows a_i to appear negative, if an area covered by G_k is also measured by G_{k-1} and G_{k+1} with strong sensitivity, the a_i for G_k can be negative to mitigate their strong influence on the area covered by G_k to replicate $\boldsymbol{F}$.

However, as the sum of $|negative\ a_i|$ increases, the a_i with large absolute values appear to satisfy $\Sigma a_i = 1$ [see (9)]. In general, the $Fit\ Error$ does not reach 0. Therefore, the G_ks corresponding with such a_i are more likely to include an area that substantially yields the $Fit\ Error$. As a result, $a_i TB_i$ in $\hat{T}_B$ [see (6)] is overvalued when $a_i \gg 0$ (undervalued when $a_i \ll 0$), particularly when the $Fit\ Error$ is more in the area covered by the G_is or when the T_{Bi} measured by the G_is is larger. Hence, $\hat{T}_B$ get contaminated, meaning that negative a_i must be regularly controlled.

$$Noise\ Factor = \sum_{i=1}^{N} |a_i| \tag{17}$$

If all a_i values are positive, expression (17) is unity according to (9), increasing to more than 1 along with the sum of $|negative\ a_i|$. Consequently, $Smoothing\ Factor(\kappa)$ should be determined to control the increase of $\sum|a_i|$ while $\boldsymbol{F}$ is replicated by G_ks as accurately as possible. These two requirements are often traded off. In the L1R product, the most appropriate $Smoothing\ Factor(\kappa)$ were determined dynamically for all T_B.

3.2. Possible Random Error Included in $\hat{\boldsymbol{T}}_{\boldsymbol{B}}$

The T_B measured instantaneously by G_i includes an uncertainty or random error caused by a receiver's thermal noise with a normal distribution. According to the law of great numbers, when a black body with a known brightness temperature (B) is measured repeatedly by G_i, the effect of the random errors in the measured T_B is reduced, and the mean T_B approximates B. At the same time, the width of the normal distribution of the mean T_B is narrower than that of instantaneously measured T_B and its standard deviation is defined as NEΔT (σ).

The possible NEΔT of $\hat{T}_B$ measured by the $\boldsymbol{F}$ is denoted in $\hat{\boldsymbol{\delta}}$. When B is measured repeatedly by G_i, each T_{Bi} has the same normal distribution. In addition, $\hat{T}_B$ defined by (7) follows a normal distribution with a different standard deviation from original NEΔT. $\hat{\delta}$ is the standard deviation of the normally distributed $\hat{T}_B$ expressed as

$$\hat{\delta} = \sqrt{\sum_{i=1}^{N} a_i{}^2 \delta^2} = \sqrt{aa^T}\delta^2 \tag{18}$$

4. Implementation

4.1. Antenna Pattern

The antenna patterns used in this processing were derived by approximating the patterns measured during ground tests with Gaussian functions. These approximated patterns were then projected onto the Earth's surface using the actual orbital information of GOSAT-GW to generate two-dimensional antenna patterns. Although the ground test measurements exhibited differences between the V- and H-polarizations at each frequency, the values were averaged when applying the Gaussian approximation, and a single unified antenna pattern was created for each frequency. Cross-sections of the resulting two-dimensional antenna patterns in the elevation direction (Y-axis) and azimuth direction (X-axis) are shown in Figures 4.1-1 and 4.1-2.

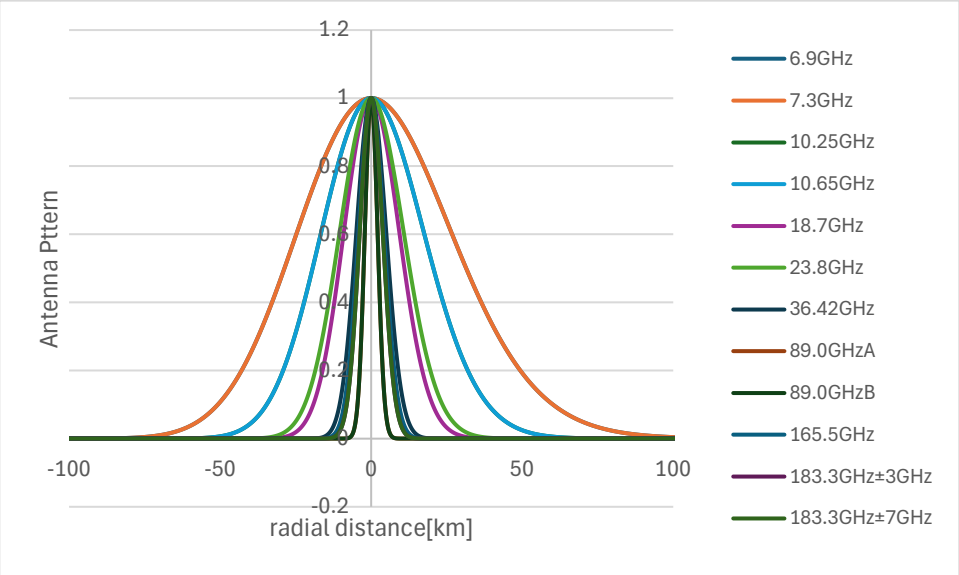

Figure 4.1-1 Antenna Patterns for Each Frequency (Elevation Direction)

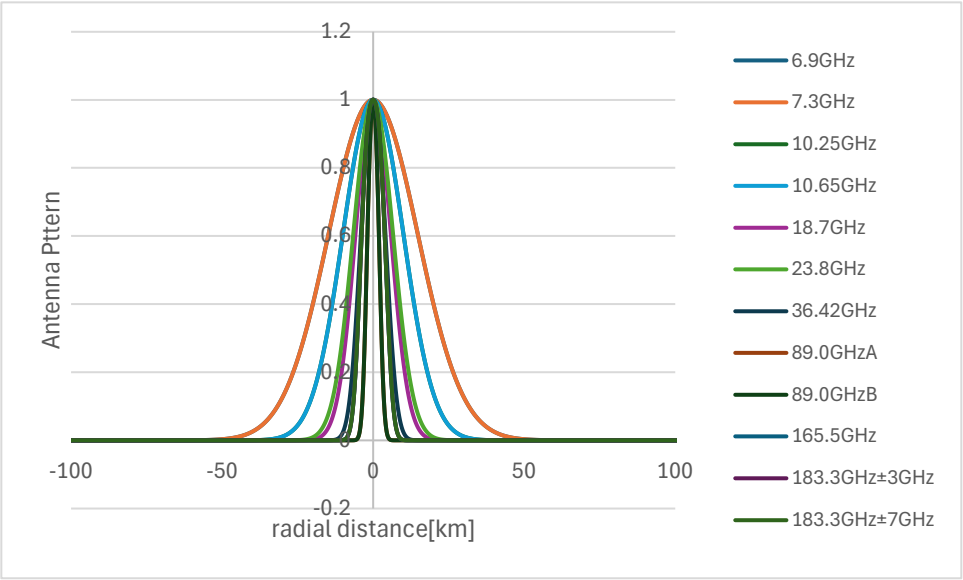

Figure 4.1-2 Antenna Patterns for Each Frequency (Azimuth Direction)

4.2. Geometry

Using the latitude and longitude information stored in the AMSR3 Level-1B product, the relative positions (distance and direction from the center) between the brightness-temperature footprint of each frequency and the target position (the 89 GHz A-scan odd points) are calculated for each observation point. The orbit-averaged values of these relative positions are then used.

Although the relative positions actually vary with latitude due to the Earth's rotation, accounting for latitude-dependent variation would require significant processing time. Therefore, a simplified approach is adopted in which the orbit-averaged values are used.

4.3. Smoothing Factor Calculation

Because the antenna patterns and geometric conditions differ for each case, it is necessary to determine the optimal Smoothing Factor (κ) for every frequency listed in Table 2-1 and for each of the 243 A-scan odd-indexed observation points at 89 GHz, where the geometric conditions vary, as described in Section 3.1.

When combining antenna patterns of significantly different footprint sizes—for example, when synthesizing the larger 6.9 GHz target antenna pattern as a linear combination of the 23.7 GHz antenna patterns, the relationship between Fit Error and Noise Factor for varying κ is shown in Figure 4.3-1. In this case, the Fit Error decreases with almost no increase in the Noise Factor, and when the Noise Factor becomes larger, the Fit Error increases accordingly. Under such conditions, the optimal Smoothing Factor (κ) is the value at which the Fit Error is minimized.

However, when synthesizing antenna patterns with comparable spatial resolutions—for instance, when adjusting only the position of the 6.9 GHz antenna pattern to match the 89.0 GHz A-scan odd-indexed points—the relationship behaves differently, as illustrated in Figure 4.3-2. In the example shown, the Fit Error reaches its minimum when the Noise Factor is approximately 4.4.

Since a high Noise Factor amplifies random errors, as discussed in Section 3.2, the AMSR3 Level-1R product imposes a constraint that the Noise Factor must not exceed 2.8. Within this allowable range, the Smoothing Factor that yields the minimum Fit Error is selected as the optimal solution.

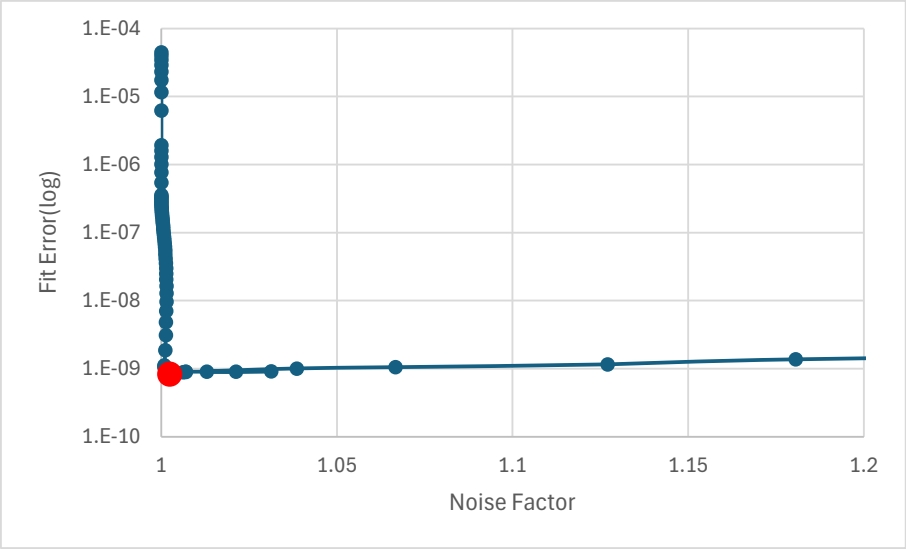

Figure 4.3-1 Relationship Between Fit Error and Noise Factor as a function of Smoothing Factor
(Example: Synthesizing the larger 6.9 GHz target antenna pattern as a linear combination of the 23.7 GHz antenna patterns near the observation center. The red point in the figure indicates the Smoothing Factor that yields the minimum Fit Error.)

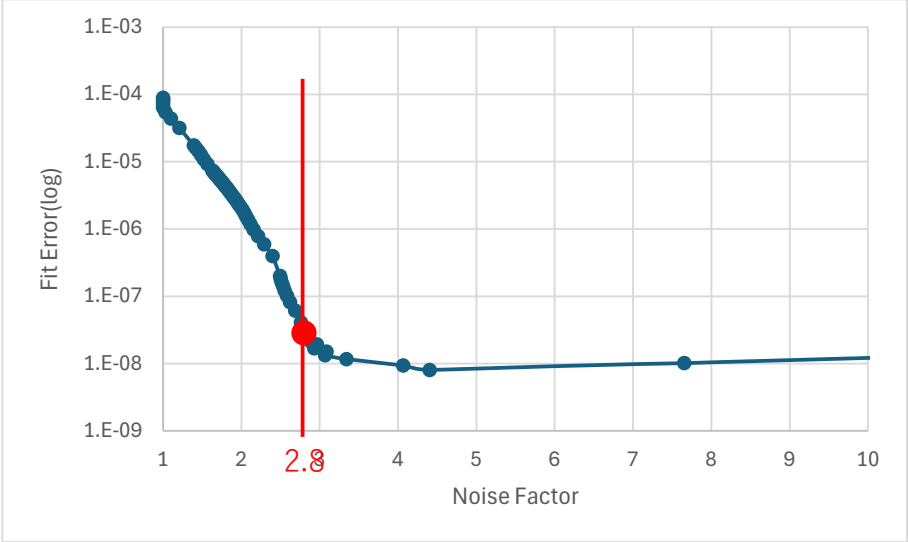

Figure 4.3-2 Relationship Between Fit Error and Noise Factor as a function of Smoothing Factor
(Case of synthesizing the 6.9 GHz antenna pattern with itself,
with the observation position aligned to the 89.0 GHz A-scan, near the observation center.)

Chapter 2.

Description of GOSAT-GW AMSR3 Integrated Water Vapor and Cloud Liquid Water Retrieval Algorithm

Hidehiko Murata

Numerical Prediction Division
Japan Meteorological Agency

Table of Contents

1. Introduction 2-3
2. Algorithm Overview 2-3
3. Theoretical Description 2-4
   3.1. Ocean algorithm 2-4
   3.2. Land algorithm 2-7
4. Algorithm Implementation 2-8
   4.1. Implementation 2-8
   4.2. Input/output parameters 2-8
   4.3. Ancillary data 2-9
   4.4. Processing flow 2-9
   4.5. Example output 2-10
   4.6. Limitations 2-11
5. Validation Concept 2-11
   5.1. Verification of integrated water vapor 2-11
   5.2. Verification of cloud liquid water 2-12

References 2-12

1. Introduction

This document describes an algorithm for retrieval of integrated water vapor and cloud liquid water from the Advanced Microwave Scanning Radiometer-3 onboard the GOSAT-GW satellite, which is a developmental continuation of the water cycle variation observation mission of GCOM-W, and the greenhouse gases observation missions of GOSAT. Vertically integrated atmospheric water vapor and cloud liquid water are key geophysical parameters to understanding the global change of the water cycle, and climate change on Earth. Atmospheric water vapor is the source of atmospheric convection and cloud formation and it plays a crucial role in precipitation processes. Cloud liquid water is linked to the radiation budget of the Earth, and its distribution is one of the undetermined parameters in weather and climate prediction modeling for global warming. Therefore, accurate and long-term measurements of these fundamental geophysical parameters are essential, not only for environmental monitoring, but also for further development and verification of numerical weather and climate prediction models.

In order to produce accurate and long-term products of these geophysical parameters, an algorithm was developed based on a physical-statistical model. The algorithm is designed to be applicable for various historical microwave radiometers. Moreover, with a view to operational application, the algorithm is computationally fast for generation of retrieval products in real time. The original algorithm (Takeuchi, 2002) that was developed at the Japan Aerospace Exploration Agency (JAXA) produces a standard AMSR-E integrated water vapor product. The algorithm was improved and a new capability was introduced to retrieve cloud liquid water from GCOM-W1/AMSR2 (Kazumori et al., 2012). The algorithm has been improved to retrieve vertically integrated atmospheric water vapor over land from GOSAT-GW/AMSR3 (Kazumori and Kachi 2018).

2. Algorithm Overview

AMSR3 observes Earth radiation from space. Microwave measurements can provide information about moisture over oceans. Measurements at microwave frequencies, i.e., 19 GHz, 23 GHz, and 37 GHz channels, allow us to observe the emission of atmospheric water vapor and cloud liquid water. The radiance at the top of the atmosphere contains integrated information on the amount of atmospheric water vapor and cloud liquid water. As each AMSR3 channel has a different sensitivity to the water vapor and cloud liquid water, AMSR3's multi-channel ability and dual polarization measurements are utilized in the algorithm. The algorithm includes separate procedures for ocean and land.

The ocean algorithm is capable of simultaneously retrieving the integrated water vapor (Total Precipitable Water, TPW) and Cloud Liquid Water (CLW) over the ocean, whereas the land

algorithm retrieves TPW over land. The calibration of TPW products is based on integrated water vapor from ground based Global Positioning System (GPS).

3. Theoretical Description

3.1. Ocean algorithm

The ocean algorithm is capable of retrieving TPW and CLW over the ocean from the AMSR3 brightness temperature under rain free conditions (Kazumori et al., 2012). The retrieval algorithm uses a physical-statistical method and is based on a theoretical microwave radiative transfer model (Stephens, 1994 and Jannsen, 1993). The model is somewhat simplified in order to be computationally fast for operational applications. A single-layer atmosphere above the sea surface is considered in the model. A vertically homogeneous and isothermal atmosphere is assumed. Emission and absorption by atmospheric water vapor, oxygen, and ozone, and emission and absorption at the sea surface are simulated in the model. The effect of varying the salinity of sea water for ocean emissivity (in other words, the dielectric constant) is not considered because the microwave frequency range of used AMSR3 channels is not very sensitive to the salinity. The effect of a rough surface ruffled by wind and the variation of ocean emissivity due to SST are considered in the algorithm.

In general, the radiative transfer equation in the microwave range is written in terms of brightness temperature as follows:

$$T_b = T_u + [\varepsilon_s T_s + (1 - \varepsilon_s) T_d] T_r \,, \qquad [1]$$

where ε_s is the ocean emissivity, T_s is the SST, and T_r is the atmospheric transmittance. On the right-hand side of the equation, the first term denotes upward emission from the atmosphere, the second term denotes upward emission from the ocean, and the third term denotes the ocean reflection of the downward emission from the atmosphere.

The mean emission temperature of the atmosphere, T_a, is introduced, and it is assumed that the mean temperatures for water vapor and for cloud liquid water in the atmosphere are equal. Consequently, the mean emission temperature is a parameter in the modeling of the atmosphere that is not separated into vapor and liquid phases. As a vertically homogeneous and isothermal atmosphere is assumed, the upward and the downward emission can be set as equal to the mean emission temperature. Under these assumptions, the equation can be written as

$$T_b = (1 - T_r) T_a + T_r \varepsilon_s T_s + T_r (1 - \varepsilon_s)(1 - T_r) T_a. \qquad [2]$$

Three different kinds of look-up tables (LUT) are used in the algorithm. The first one is for the computation of ocean emissivity. The inputs of the LUT are SST, SSW, and the AMSR3 channel

microwave frequencies. The second LUT is for the computation of atmospheric mean emission temperatures. The inputs of the LUT are the square of the atmospheric transmittance estimated in the algorithm and the temperature at 850 hPa from Japan Meteorological Agency (JMA) global numerical weather prediction (JMA 2026) results. The last LUT is for conversion from index parameters to TPW and CLW.

The ocean emissivity can be obtained from the first LUT by using ancillary SST and SSW data. The LUT is produced by using a match-up data set of atmospheric profile data from RAOB, AMSR2 brightness temperature observations, and ancillary SST and SSW data. The LUT is also applicable for AMSR3 and provides the ocean emissivity for each AMSR3 frequency as a function of SST and SSW. For this algorithm, the SST and SSW used as ancillary input data are obtained from JMA global numerical weather prediction results. For near real time TPW and CLW generations, SST and SSW are obtained from JMA's short-range global forecasts. Temperatures at 850 hPa are also obtained from JMA data and are used as an input in the estimation of atmospheric transmittance at a later stage in the algorithm. Since TPW and CLW are retrieved for each Field of View (FOV) of AMSR3, these ancillary data were interpolated spatially and temporally for the AMSR3 FOV location.

It is relatively easy to describe the characteristics of an ocean surface compared with those of a land surface. Ocean surface emissivity is characterized by observational microwave frequency, SST, SSW, incidence angle, and ocean salinity. The dependency of sea surface reflectivity and emissivity on SSW and SST is not described explicitly in the model. Indeed, the ocean surface is assumed to be a specular surface and the Fresnel law is used to find the reflectivity and the emissivity of the ocean. The deviation from the Fresnel law of the rough ocean surface is estimated empirically by using the second LUT, produced by matching up data from radiosonde observation, SST and SSW, and AMSR2 data. The atmospheric profiles from RAOB, SST, SSW and a general microwave radiative transfer calculation were used to produce the LUT for the empirical emissivity estimation. This empirical emissivity estimation method (Kazumori et al., 2008) is based on real observed microwave brightness temperature. The resulting LUT can capture SST and SSW dependency accurately. It should be noted that the accuracy is highly dependent on the calibration accuracy of the input AMSR3 brightness temperature.

The previous equation can be written by introducing a parameter α as indicated below:

$$T_b = \alpha\{1 - (1 - \varepsilon_s)T_r^2\} \quad [3]$$

$$\alpha \equiv \left\{T_a + \frac{(T_s - T_a)T_r\varepsilon_s}{1 - (1 - \varepsilon_s)T_r^2}\right\} \quad [4]$$

The square of the transmittance is written as below:

$$T_r^2 = \frac{1 - T_b/\alpha}{1 - \varepsilon_s} \quad [5]$$

Figure 1 shows a schematic diagram of the TPW and CLW retrieval algorithm. The transmittance is estimated in the algorithm. In step 1, the ocean emissivity is estimated by using the first LUT, ancillary SST and SSW data, and AMSR3 channel frequencies at each AMSR3 observation location. In step 2, an initial value is set for the transmittance. In step 3, the mean emission temperature is obtained from the second LUT. The transmittance and temperature at 850 hPa at the AMSR3 observation location are used as input data for the LUT. The pre-defined LUT was created in advance by using atmospheric profiles (temperature, humidity) from RAOB and a microwave radiative transfer calculation. In step 4, the parameter α is calculated by using Eq. [4] for each frequency and each polarization. In step 5, the transmittance is calculated from the AMSR3 brightness temperature by using Eq. [5] for both polarizations. In step 6, the transmittances for each frequency are estimated as the geometric mean of transmittance found for each polarization. Then, we repeat from step 3 to step 6 iteratively to find an optimized value for the atmospheric transmittance. The iterative algorithm is fairly stable, so that a few iterations are sufficient to reach the convergence.

A further step of the algorithm consists in calculating two index parameters that can be converted into TPW and CLW through a monotonic law. The indices, PWI (Precipitable Water Index) and CWI (Cloud liquid Water Index), are calculated by the following equation:

$$PWI = \beta \ln(T_{r19HV}^2) - \ln(T_{r22V}^2) + \gamma CWI \quad [6]$$

$$CWI = \ln(T_{r19HV}^2) - \ln(T_{r37HV}^2) \quad [7]$$

where $\beta = \beta(T_s)$ is a function of SST and γ is a constant. The indices are defined to represent monotonically increasing (or decreasing) amounts with TPW and CLW increase (or decrease) (Takeuchi, 2002; Takeuchi et al., 2004). The third LUT, which is used in this conversion, defines the relationship between SST and the parameters β and γ. The LUT is produced in advance to maximize correlations between PWI and observed GPS TPW. An additional atmospheric moisture correction is applied to the CWI before it is being converted into CLW. As the CWI contains the atmospheric water vapor dependency in the intermediate parameters, the CWIs are stratified into some TPW categories and the dependency is removed with a linear correction function. Pre-defined coefficients are used in the conversion. The observation at 37 GHz contains some SSW dependency. The SSW dependency is removed by using a wind speed related parameter (S36, defined in Shibata, 2012) in the algorithm. The LUTs used in the algorithm are smoothed for possible input parameter ranges to avoid

discontinuities in the retrieval due to insufficient sampling data from RAOB.

3.2. Land algorithm

The land algorithm is capable of retrieving TPW over land from the AMSR3 brightness temperature. The retrieval algorithm uses dual-polarized microwave radiance at 19 GHz and 23 GHz from AMSR3. Eq. [8] is another expression of a simplified microwave radiative transfer equation that is widely used in geophysical parameter retrievals in non-scattering cases (The notation used in this document follows that of Kazumori and Kachi (2018)):

$$T_B^p = \varepsilon_A T_A + \varepsilon_S^p T_S \Gamma + \varepsilon_A T_A \left(1 - \varepsilon_S^p\right) \Gamma , \quad [8]$$

where T_B is the observed microwave brightness temperature and p is the vertical or horizontal polarization. Γ denotes atmospheric transmittance. The atmospheric temperature is written as T_A and the surface temperature as T_S. In the algorithm, we assume an isothermal atmosphere $T_A = T_S$ for simplification. ε_S is land surface emissivity and ε_A is atmospheric emissivity. The right-hand side of Eq. [8] consists of the upwelling atmospheric emission, the surface emission attenuated by the atmosphere, and the down-welling atmospheric emission reflected by the land surface and attenuated by the atmosphere.

By taking the difference between the vertical and horizontal polarized brightness temperatures of Eq. [8] at 19 GHz and 23 GHz, we can obtain Eq. [9] as follows:

$$\Delta T_B = T_B^V - T_B^H = (\varepsilon_S^V - \varepsilon_S^H)(T_S - \varepsilon_A T_A)\Gamma . \quad [9]$$

Because $\Gamma = 1 - \varepsilon_A$ from Kirchhoff's Law, Eq. [9] can be rewritten as follows:

$$\Delta T_B = \Delta\varepsilon_S T_S \Gamma^2 , \quad [10]$$

where $\Delta\varepsilon_S$ is the emissivity difference over land.

Using LWP (liquid water path) and TPW (total precipitable water vapor), Eq. [10] can be rewritten as follows:

$$\Delta T_B = \Delta\varepsilon_S T_S \exp[-2(\tau_0 - \alpha_1 LWP - \alpha_2 TPW)] , \quad [11]$$

where $\tau_0, \alpha_1, \alpha_2$ are the optical depth for dry air and the extinction coefficients for cloud liquid and water vapor, respectively. Eq. [11] indicates that the polarization difference at the brightness

temperatures of 19 GHz and 23 GHz are proportional to their emissivity differences from the polarized channels.

$$\Delta T_B = \Delta\varepsilon_S T_S \exp[\beta_0 + \beta_1 LWP + \beta_2 TPW] \ . \quad [12]$$

The parameters $\beta_0, \beta_1, \beta_2$ are exponentially dependent on the amount of precipitable water vapor and have considerable spatial variability due to vegetation, soil moisture, and other surface conditions. However, their ratios of spectrally close channels (19 GHz and 23 GHz) and an assumption of their frequency independence with respect to land surface emissivity (i.e., $\Delta\varepsilon_S^{19} = \Delta\varepsilon_S^{23}$) enable the utilization of their sensitivities to retrieve atmospheric water vapor. LWP can be set to zero over land because LWP is O(1) smaller than TPW. By taking the ratio of Eq. [12] for 19 GHz and 23 GHz, we obtain a linear relationship between TPW and the polarization difference signal of the observed microwave radiance:

$$TPW = \frac{\log\left(\frac{\Delta T_B^{23}}{\Delta T_B^{19}}\right) - (\beta_0^{23} - \beta_0^{19})}{\beta_2^{23} - \beta_2^{19}} \ . \quad [13]$$

This relationship can be described using two coefficients a, b as follows:

$$\log(\frac{\Delta T_B^{23}}{\Delta T_B^{19}}) = a \times TPW + b. \quad [14]$$

a and *b* are produced in advance to maximize correlations between $\log(\frac{\Delta T_B^{23}}{\Delta T_B^{19}})$ and observed GPS TPW.

4. Algorithm Implementation

4.1. Implementation

The algorithm is implemented into the operational JAXA computer in the GCOM ground system to determine TPW and CLW from GOSAT-GW/AMSR3 data in real time. Additional quality flags indicating the retrieval accuracy, as well as sea ice detection, rain flags, and vegetation areas, are generated. The products are saved in files for every ascending and descending orbit. The data file format is NetCDF4.

4.2. Input/output parameters

Input parameters

AMSR3 Level 1R brightness temperatures, i.e., measurements with dual polarization channels at 19 GHz, 23 GHz, 37 GHz, and 89 GHz, are used as input parameters for the algorithm. Information at 89 GHz is used mainly for rain detection by the algorithm. Several ancillary data (SST, SSW, and temperature at 850 hPa) are interpolated spatially and temporally at the AMSR3 observation location. The incidence angle of the AMSR3 measurement is used for the radiative transfer calculation in the algorithm.

As described in Section 2, three different look-up tables are used as input information by the algorithm. The first one is for the computation of ocean emissivity. The inputs of the LUT are SST, SSW, and AMSR3 channel microwave frequency (i.e., 19 GHz, 23 GHz, and 37 GHz). The LUT produces ocean emissivity for each AMSR3 channel. The second one is for the computation of atmospheric mean emission temperatures. The inputs of the LUT are the square of the atmospheric transmittance and the temperature at 850 hPa from ancillary data. The last one is for the conversion from index parameters for atmospheric integrated water vapor and cloud liquid water to real values.

The LUTs are predefined by using a radiative transfer model and a collocated data set with AMSR3 and atmospheric profiles from RAOB (the first and second one) and integrated water vapor from GPS (the third one).

Output parameters

The output parameters are atmospheric integrated water vapor and cloud liquid water in the AMSR3 field of view. The algorithm produces some quality flags indicating the retrieval accuracy. The data are categorized into three meteorological conditions (clear, cloudy, and rainy). Rain and sea ice contamination flags are also produced.

4.3. **Ancillary data**

The temperature at 850 hPa and SSW from JMA global atmospheric analysis and SST from JMA global sea surface temperature analyses are used as ancillary data for the standard product. For real time production of TPW and CLW, the analyzed values are not available. Temperatures at 850 hPa and SSW from the short range global forecast of the JMA global model are used as ancillary input data.

4.4. **Processing flow**

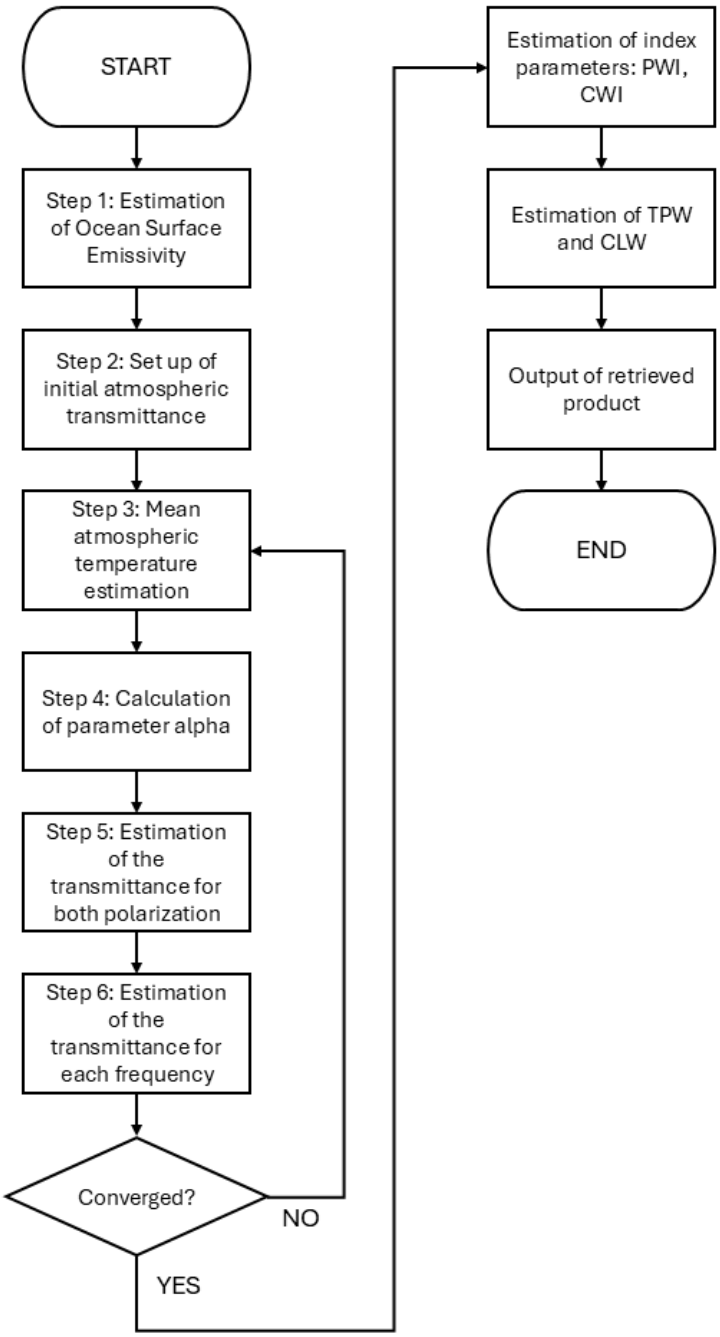

Figure 1. Schematic diagram of the atmospheric water vapor (TPW) and cloud liquid water (CLW) retrieval algorithm over the ocean.

4.5. **Example output**

The global map of atmospheric integrated water vapor (Figure 2(a)) represents the moist region associated with the Inter-Tropical Convergence Zone (ITCZ) and the maritime continent. In the global map of cloud liquid water (Figure 2(b)), cloudiness associated with low pressure systems is shown in

the mid- and high latitude areas.

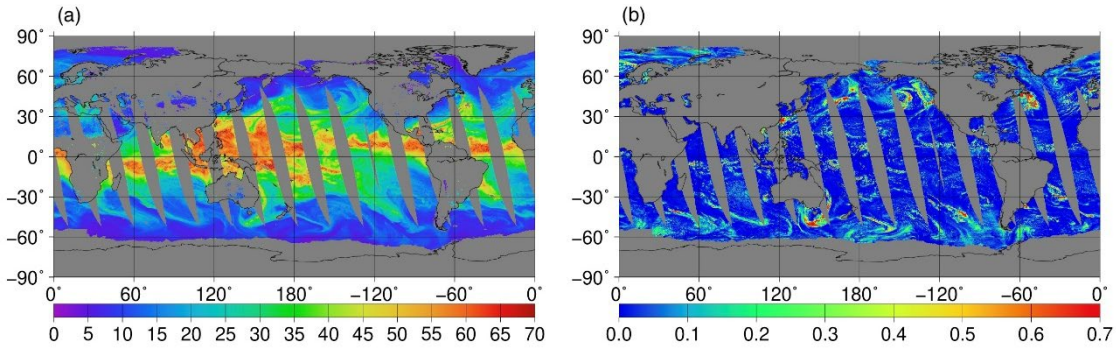

Figure 2. Global map of AMSR3 integrated water vapor (a) and cloud liquid water (b) in November 4, 2025 for ascending data. The units are [kg/m^2] for water vapor and [kg/m^2] for cloud liquid water.

4.6. **Limitations**

Because the ocean algorithm is applicable only to open ocean areas and rain free conditions, data over land and for rainy conditions are not available. The land algorithm is applicable only to non-vegetation areas. Furthermore, as the algorithm does not include cloud distribution inside the AMSR3 field of view, there is a possibility of overestimation or underestimation of the cloud liquid water amount. It is difficult to validate the product with independent real observations of cloud liquid water content.

5. Validation Concept

5.1. **Verification of integrated water vapor**

Historically, integrated water vapor calculated from radiosonde observation profiles has been used as truth data in the verification of satellite microwave radiometer integrated water vapor products. Since RAOB provides direct measurements of atmospheric humidity profiles, the estimated integrated water vapor can be considered highly accurate compared with other remote sensing observations. For the ocean algorithm, in order to minimize land contamination in the integrated water vapor verification, RAOB on small islands should be used in preference to stations on larger land masses, and appropriate temporal and spatial collocation criteria should be set to obtain sufficient sampling data between GOSAT-GW/AMSR3 and RAOB. In addition, careful quality control should be applied to the radiosonde observations before the verification. However, the temporal and spatial resolution of the RAOB network is not sufficient for the verification of satellite-based water vapor retrievals under various meteorological conditions, due to the sparse observation network. In particular, the local time of GOSAT-GW/AMSR3 observations is fixed (13:30). This limits the number of RAOBs available for the collocation process.

In addition to verification with RAOB, measurements from the Global Positioning System (GPS) have been made available to the public domain, and the Integrated Water Vapor (IWV) from ground-based GPS receivers can be used as new references for satellite product verification.
GPS IWV observations are also becoming valuable in operational NWP and weather forecasting, thanks to their high accuracy and frequent sampling (five-minute intervals). Preliminary validation results for the AMSR-E TPW products are shown in Kazumori et al. (2012).

5.2. **Verification of cloud liquid water**

Since there are few direct CLW measurements available, it is difficult to verify the accuracy of the CLW product comprehensively. Therefore, the accuracy of CLW products can be estimated only indirectly. A proposed method in Greenwald et al. (2007) and Greenwald (2009) can be used for the estimation of certain CLW error characteristics. Cloud clear scenes of AMSR3 are selected using VIIRS collocated images. The cloud fraction of VIIRS Level 2 products was utilized in the cloud clear scene determination (i.e., zero cloud fraction as determined by collocated VIIRS products). The data are stratified with respect to SSW, SST, and TPW categories. This technique has been used by Wentz and Meissner (2000) and enables us to identify false correlations among different geophysical parameters derived from the microwave radiometer.

References

Greenwald, T. J., T. S. L'Ecuyer, and S. A. Chirstopher 2007: Evaluating specific error characteristics of microwave-derived cloud liquid water products. *Geophys. Res. Lett.*, **34**, L22807, doi:10.1029/2007GL031180.

Greenwald, T. J. 2009: A 2 year comparison of AMSR-E and MODIS cloud liquid water path observations. *Geophys. Res. Lett.*, **36**, L20805, doi:10.1029/2009GL040394.

Janssen, M A., Ed. (1993) Atmospheric Remote Sensing By Microwave Radiometry. John Wiley & Sons, Inc., pp. 572.

Japan Meteorological Agency 2026: Outline of the Operational Numerical Weather Prediction at the Japan Meteorological Agency. Available from https://www.jma.go.jp/jma/jma-eng/jma-center/nwp/outline2026-nwp/index.htm

Kazumori, M., Q. Liu, R. Treadon, and J. C. Derber 2008: Impact Study of AMSR-E Radiances in the NCEP Global Data Assimilation System. *Monthly Weather Review*, 136, 541 – 559.

Kazumori, M., T. Egawa and K. Yoshimoto 2012: A retrieval algorithm of atmospheric water vapor and cloud liquid water for AMSR-E. *European Journal of Remote Sensing*, **45**, 63 – 74. doi: 10.5721/EuJRS20124507.

Kazumori, M., and M. Kachi 2018: Precipitable Water Vapor Retrieval over Land from GCOM-W/AMSR2. *Transactions of the Japan Society for Aeronautical and Space Sciences, Aeropace*

Technology Japan, **16(2)**, 143 – 146. doi: 10.2322/tastj.16.143

Menzel, M. P., R. A. Frey, and B. A. Baum 2010: Cloud top properties and cloud phase algorithm theoretical bases document. University of Wisconsin, Madison. Available from http://modis-atmos.gsfc.nasa.gov/_docs/CTP_ATBD_oct10.pdf.

Shibata, A. 2012: Ocean Wind Speed Retrieval Algorithm using the frequency 36GHz Vertical/Horizontal and 6GHz Horizontal Data of the Advanced Microwave Scanning Radiometer (AMSR). *European Journal of Remote Sensing*, **45**, 133 – 140. doi: 10.5721/EuJRS20124513.

Stephens G. L. 1994: Remote sensing of the lower atmospheric: an introduction. Oxford University Press, pp. 523.

Takeuchi, Y. 2002: Algorithm theoretical basis document (ATBD) of the algorithm to derive total water vapor content from ADEOS-II/AMSR. EORC Bulletin/Technical Report.

Takeuchi, Y., T. Tauchi, S. Saito, K. Imaoka, M. Kachi, and A. Shibata 2004: A total column precipitable water algorithm for ADEOS-II/AMSR and Aqua/AMSR-E. *Italian Journal of Remote Sensing* **30/31**, 143 –157.

Wentz, F. J., and T. Meissner 2000: AMSR Ocean Algorithm Theoretical Basis Document (ATBD). RSS Tech. Doc. 121599A –1, Remote Sens. Syst., Santa Rosa, Calif.

Chapter 3.

Description of GOSAT-GW AMSR3 Rainfall Retrieval Algorithm

Kazumasa Aonashi

Kyoto University

Table of Contents

1. Introduction 3-3

1.1 Background 3-3

1.2 The objective 3-3

2. Data and radiative transfer model used 3-4

2.1 AMSR3 TB 3-4

2.2 Radiative transfer model (RTM) 3-4

2.3 GANAL and MGDSST 3-4

2.4 AutoSNOW 3-4

2.5 Surface emissivity (Es) 3-4

3. Algorithm description 3-5

3.1 Outline 3-5

3.2 Improvements over the conventional algorithm 3-5

3.3 Algorithm Configuration 3-6

3.3.1 A priori information 3-6

3.4 Forward calculation 3-9

3.4.1 preprocessing 3-9

3.4.2 RTM calculation 3-9

3.5 Retrieval 3-9

3.5.1 Detection of precipitation areas 3-10

3.5.2 TBc correction using TBo over rain-free areas 3-10

3.5.3 Estimation of inhomogeneity of precipitation and CPF 3-11

3.5.4 Retrievals using scattering signals 3-11

3.5.5 Retrievals using emission signals over ocean 3-11

4 Validation 3-12

5 Summary 3-12

References: 3-12

1. Introduction

1.1 Background

Precipitation is one of the most important parameters of the Earth system and is fundamental information in various fields such as meteorology, climate, flooding, and agriculture. However, conventional ground-based observations (rain gauges and precipitation radar) are limited to a part of the land surface. Therefore, satellite observation data is indispensable to understand global precipitation (especially, tropical cyclones that occur and develop over the tropical oceans).

Currently, the main satellite sensors used for remote sensing of precipitation are precipitation radars, microwave radiometers (MWRs), and infrared radiometers. Figure 1 shows observations of a mesoscale convective system over the sea south of Kyushu.

The precipitation radars emit microwaves and measure backscattering by precipitation particles. Satellites equipped with precipitation radars are rare and their observation range is narrow, which limits the opportunities of observation.

MWRs receive microwaves from the Earth's atmosphere and can see signals of rain and frozen precipitation particles, which are large water particles (Aonashi and Ferraro, 2020). MWRs are more frequently observed than precipitation radars because they are installed on many Low Earth Orbit (LEO) earth observation satellites.

Infrared radiometers are carried on geostationary satellites etc. and are observed much more frequently. Infrared TBs are sensitive to cloud droplets, which makes it difficult to retrieve precipitation.

The Advanced Microwave Scanning Radiometer 3 (AMSR3) is a microwave radiometer onboard the Global Observing SATellite for Greenhouse gases and Water cycle (GOSAT-GW), which was launched by JAXA on June 29, 2025 (Inaoka et al, 2026). AMSR3 continues the observations of various physical variables related to Earth's water cycle variations, which were carried out by its predecessors: the AMSR onboard the Advanced Earth Observing Satellite II (ADEOS-II) "Midori II," the AMSR-E onboard the Aqua satellite, and the AMSR2 onboard the Global Change Observation Mission - Water (GCOM-W) "Shizuku" (Imaoka et al, 2010).

1.2 The objective

The purpose of this document is to describe the rain retrieval algorithm (V01) for AMSR3. The major improvements implemented in this algorithm, compared to the previous version (AMSR2 V03), are as follows:

1. Update of the precipitation detection method: The precipitation detection method in the retrieval module has been updated to an approach which utilizes surface emissivity (Es), and other parameters as inputs.

2. Correction of scattering-based precipitation intensity retrieval: In the precipitation intensity retrieval section that utilizes scattering signals, the retrieved precipitation values are now corrected using a Support Vector Machine (SVM), incorporating physical variables related to the Convective Precipitation Fraction (CPF) and Frozen Precipitation Depth (FPD).

2. Data and radiative transfer model used

2.1 AMSR3 TB

AMSR-3 is a microwave imager onboard the GOSAT-GW satellite that observes brightness temperatures (TBs) for the following frequencies: 6.925, 7.3, 10.25, 10.65, 18.7, 23.8, 36.42, 89.0, 165.5, 183.3±3, and 183.3±7 GHz. Among these, the 23.8, 165.5, 183.3±3, and 183.3±7 GHz channels observe vertical polarization only, while the other channels observe both horizontal and vertical polarizations. Equipped with a large 2-meter diameter antenna, AMSR-3 achieves improved spatial resolution across all microwave channels (Inaoka et al, 2026).

2.2 Radiative transfer model (RTM)

We used the RTM program of Liu (2004). This program computed the TBc for the plane-parallel atmosphere by four-stream approximation. In this study, all the precipitation particles were assumed to be spherical, and the absorption and scattering coefficients as well as phase functions were computed from the Mie theory.

2.3 GANAL and MGDSST

The algorithm incorporates physical variables of atmosphere and surface conditions except for sea surface temperatures from the Japan Meteorological Agency (JMA) Global Analysis (GANAL). Sea surface temperatures are derived from JMA's Merged satellite and in situ data Global Daily Sea Surface Temperatures in the global ocean (MGDSST) data.

2.4 AutoSNOW

This study utilized AutoSNOW, a daily global snow and ice flag from the National Snow and Ice Data Center (NSIDC) in the United States, as an indicator for snow cover and sea ice.

2.5 Surface emissivity (Es)

The precipitation area detection method developed in this study inputs the Global Precipitation Measurement (GPM) Microwave Imager (GMI) surface emissivity (Es). Therefore, GMI Es was obtained using the following procedure:

1) Synthesize GMI TB from AMSR3 TB.

2) Estimate Es from GMI TB using the method of Turk et al. (2014).

To synthesize GMI TB from AMSR3 TB, we developed a linear regression model for GMI TB using GMI–AMSR3 matchup data from August to December 2025 (with an observation time difference within 600 seconds), where AMSR3 TB, surface temperature Ts, and fraction of water (FOW, Mega and Shige, 2016) were used as inputs.

Next, from the synthesized GMI 18–89 GHz vertically and horizontally polarized TB, the vertically and horizontally polarized TB at 18–89 GHz was estimated using the EPC method of Turk et al. (2014) (hereafter referred to as EsEPC).

3. Algorithm description

3.1 Outline

The algorithm consists of a priori information for the atmosphere, surface conditions, and precipitation clouds, a forward calculation module, and a retrieval module (Figure 2).

In the forward calculation module, look-up tables (LUTs) of MWR TBc are calculated for the surface precipitation rate using a priori information. The retrieval module obtains the surface precipitation rate that gives the TBc value that best matches TBo.

The algorithm is applied to locations where the surface temperature is 0C or higher and that are free of snow cover and sea ice.

3.2 Improvements over the conventional algorithm

The conventional precipitation area detection method (hereafter referred to as conventional method) underestimates precipitation areas over land and coastal regions compared to GPM Dual-frequency Precipitation Radar (DPR) observations. In particular, it frequently misses precipitation events in areas with high frequencies of orographic precipitation, such as the Western Ghats. Conversely, over the ocean, the conventional method overestimates precipitation areas compared to DPR observations.

In this study, we first analyzed the effects of surface conditions and environmental fields on the probability density functions (PDFs) of GMI EsEPC and the ratio of TB to Ts (TB/Ts) in both precipitating and non-precipitating areas. The results revealed that while EsEPC and TB/Ts vary significantly in coastal regions, they exhibit a high correlation with the FOW of each GMI pixel. Furthermore, calculating the difference (dEs) between EsEPC and the estimated non-precipitating

value (Es0) for each FOW showed that the standard deviation (STD) of dEs is larger in precipitating areas than in non-precipitating areas.

The conventional method misses DPR-detected precipitating areas with small scattering signals (referred to as "Miss"), which frequently occur in regions with high frequencies of orographic precipitation. Therefore, we investigated the characteristics of orographic precipitation indices (Shige and Kumerrow, 2016, Yamamoto et al, 2017) when such Miss events occur. The results demonstrated that Miss events have a peak probability of occurrence along the coast, and that the low-level relative humidity (RH) is concentrated at 90% or higher.

Based on these findings, we developed a new precipitation area detection method that regresses the DPR rain flag. This method uses surface conditions, environmental fields, and orographic precipitation indices as inputs, in addition to EsEPC and TB/Ts. The global domain was divided into regions, and separate regression models were constructed for land/coastal areas and oceanic areas within each region. Note that the target areas were limited to regions without snow cover and sea ice using NSIDC AutoSNOW. For the AMSR3 routine processing, a regression model based on a linear algorithm was constructed.

Additionally, in the precipitation intensity retrieval section that utilizes scattering signals within the retrieval module, the retrieved precipitation values were corrected using SVM, incorporating physical variables related to CPF and FPD.

3.3 Algorithm Configuration

3.3.1 A priori information

As Figure 3 schematically illustrates, the RTM calculation requires information on atmospheric variables (temperature, relative humidity, Freezing Level Height (FLH), Cloud Liquid Water Content (CLWC), etc.), surface conditions (surface temperature, sea surface wind speed), and precipitation-related variables (precipitation profiles, precipitating particle size distribution, refractivity of frozen and mixed-phased particles, horizontal inhomogeneity of precipitation, etc.).

In this study, the FPD was estimated by the forward calculation module based on a priori information. The precipitation cloud model was then varied by precipitation type and the FPD. Inhomogeneity of precipitation and CPF were estimated in the retrieval module.

3.3.1.1 Atmospheric and surface variables

We adopted atmospheric temperature, FLH, and surface temperature over land and coast from JMA GANAL. We adopted sea surface temperature from JMA MGDSST. The LUTs were calculated for every 5x5 degree point in the latitude-longitude coordinates. Thus, we incorporated the above

variables on the 5x5 degree points into the RTM calculation. As for relative humidity and CLWC, we assumed the same constant values, 100 % and 0.5 kg m^{-2}.

3.3.1.2 Precipitation type

We constructed statistical precipitation profile models using the Tropical Rainfall Measuring Mission (TRMM) observation. To this end, first, we classified TRMM Precipitation Radar (PR) data into 14 types (8 over land, 6 over ocean) by the ratio between PR precipitation rates and TRMM Lightning Imaging Sensor (LIS) flash rates (Takayabu 2008).

Coastal zones within 200 km of the coastline exhibit precipitation characteristics distinct from those of inland and open-ocean regions (Ogino et al., 2016). Therefore, within the coastal grid boxes, this study defined coastal-ocean and coastal-land precipitation types that correspond to the six oceanic precipitation types.

3.3.1.3 Frozen precipitation depth (FPD)

Similar to previous studies (Shige and Kumerrow, 2016), this study examined the correlation between FPD and GANAL physical variables. The results show that FPD correlates relatively well with physical variables such as atmospheric instability and relative humidity (RH). FPD also correlates with surface precipitation rate, since stronger precipitation tends to be taller. Based on this, this study obtained an index of FPD (FPD_ENV) for given surface precipitation rate from GANAL's mid-lower tropospheric temperature lapse rate and RH.

3.3.1.4 Precipitation profile

Precipitation profiles vary in high correlation with FPD. Convective precipitation has stronger frozen precipitation than stratiform precipitation, which also shows greater variability with FPD.

For each precipitation type, this study obtained the statistical mean and standard deviation of precipitation profiles for convective and stratiform precipitation using DPR data. We also calculated correlation between the DPR precipitation rate at each level and the FPD. However, for the coast, the number of samples was small, so both coastal land and sea data were used to create statistics for the coastal precipitation profiles.

In low temperature regions, the precipitation profiles near the surface became too shallow. To avoid this, FLH-weighted averages of the conventional precipitation profiles and the WAKASA2003 profiles were used in the region where the FLH was below 1500 m.

3.3.1.5 Particle size distribution

For rain drop size distribution, we constructed statistical models for each precipitation type using the globally-available TRMM PR observations (Kozu et al. 2009). To this end, first, we assumed the gamma distribution of rain drop size:

$$N(D) = N_0 D^{\mu} \exp(-\lambda D), \quad (1)$$

where N is the number concentration for particles with diameter D, μ=3, N_0 and λ are parameters to be determined. For convective precipitation, we calibrated N_0 and λ using the attenuation corrected factors derived from the PR data. For stratiform precipitation, we used the standard values of N_0 and λ of PR 2A25 version 6. Then, we averaged the above values for each precipitation type to produce the statistical models of rain drop size distribution.

On the other hand, conventional models were used for frozen and mixed-phase particle size distribution that could not be estimated from the TRMM observation. For frozen particle size distribution, we applied the Harimaya (1977)'s distribution to both convective and stratiform precipitation. Particle size distribution for mixed-phase stratiform precipitation (between FLH minus 1 km and FLH) was parameterized in terms of atmospheric temperature (Nishituji et al. 1983), while we neglected mixed-phase convective precipitation.

3.3.1.6 Density of frozen and mixed-phase precipitation particles

We estimated frozen precipitation particle densities for convective and stratiform precipitation using DPR Ku radar observed reflective factor (Zm) versus the difference between -Ku and Ka radar reflective factors (DFR). The estimated frozen precipitation particle density averaged over 2015-2018 increased with altitude difference from FLH.

Based on this, we searched by trial and error for the optimal value of frozen precipitation density for FPD_ENV, such that the zonal mean of the precipitation bias for the over-land MWR retrievals for July 2014 is close to zero. The results show that the optimum values of frozen precipitation density are (0.65-0.80) for convective and (0.50-0.65) for stratiform at 89 GHz.

Density of mixed-phase stratiform particles was parameterized in terms of atmospheric temperature (Nishituji et al. 1983).

3.3.1.7 Convective precipitation fraction (CPF)

Following previous studies, this study calculated correlations between the DPR CPF and various physical variables. The results showed high correlations with the index of FPD (FPDpix) obtained from GANAL and MWR retrievals, inhomogeneity of precipitation estimated from MWR, polarization difference of TB89, and surface temperature. Based on this, an index of CPF (CPFpix) was estimated from the above physical variables.

3.4 Forward calculation

3.4.1 preprocessing

From GANAL and MGDSST, atmospheric and surface variable data were created for every 5x5 degree point in the latitude-longitude coordinates. Based on a priori information, FPD_ENV for each precipitation rate was calculated from the GANAL data. Then, the precipitation profile and the density of frozen precipitation were varied by precipitation type and FPD_ENV.

3.4.2 RTM calculation

First, we calculated the convective and stratiform LUTs for horizontally homogeneous precipitation by incorporating the above atmospheric, surface, and precipitation-related variables into the RTM program of Liu (2004) for every 5x5 degree point in the latitude-longitude coordinates.
Then, we derived the convective and stratiform LUTs with various horizontal precipitation inhomogeneities by the approximation of Aonashi and Liu (2000). This approximation converted TBc for homogeneous precipitation (TB^h) into those for inhomogeneous precipitation (TB^i), assuming the lognormal distribution of precipitation:

$$TB^i = \int \frac{1}{\sqrt{2\pi}\xi} \exp[-\frac{1}{2\xi^2}(\ln(pr) - \overline{\ln(pr)})^2] TB^h \; d\ln(pr), \tag{2}$$

where ln(*pr*) is the natural logarithm of precipitation, and $\overline{\ln(pr)}$ and ξ is the average and the standard deviation of ln(*pr*), respectively.
The LUTs used in the retrieval module were weighted averages of the above convective and stratiform LUTs. The weights were determined by the statistical frequency distribution of DPR convective and stratiform precipitation for each precipitation type and surface precipitation rate.

3.5 Retrieval

The retrieval module performs detection of precipitation areas, TBc correction using TBo over rain-

free areas, estimation of inhomogeneity of precipitation and CPF, retrievals using scattering signals, and retrievals using emission signals over ocean.

3.5.1 Detection of precipitation areas

In this study, we developed a new precipitation area detection method that regresses the DPR rain flag. This method incorporates surface conditions, environmental fields, and orographic precipitation indices as inputs, in addition to GMI EsEPC and TB/Ts. The specific inputs to the regression model consist of EsEPC (es18v, es18h, es23v, es36v, es36h, es89v, es89h), TB/Ts (tb166v/Ts, pct89/Ts), surface conditions (FOW, surface type), environmental fields (Ts, low-level RH), and orographic precipitation indices (orographic updraft, DFC, low-level moisture convergence, low-level lapse rate).

To account for regional variations in the relationships of EsEPC and TB/Ts versus the DPR rain flag, as well as variations in Miss events and orographic precipitation indices, the global domain was divided into distinct regions. Separate models were then constructed for land/coastal areas and oceanic areas within each region. Furthermore, because distinguishing between precipitating and non-precipitating areas is challenging over snow cover and sea ice, the target areas were restricted to regions outside of snow and sea ice cover using AutoSNOW.

We constructed the model to regress the DPR rain flag using a linear regression algorithm. The training data utilized for each region's land/coastal and oceanic models were GMI–DPR matchup data collected from June 2014 to May 2016. Notably, the training data were categorized into five classes based on the following Ts ranges: (-10~8C), (4~14 C), (10~20 C), (16~26 C), (22~50 C).

The output of this new precipitation area detection method shows an increased (decreased) precipitation area fraction over land and coasts (oceans) compared to the conventional method, bringing the estimates closer to DPR observations. Additionally, the correlation with the DPR rain flag improved relative to the conventional method, particularly along coastal zones. Furthermore, missed precipitation events in regions such as the western coast of Burma and the Western Ghats were reduced (see Fig. 4).

3.5.2 TBc correction using TBo over rain-free areas

The algorithm first classifies each pixel into land, coastal, and ocean classes. For each class, a correction value for the forward-calculated PCT36 and PCT89 of 0 mm/h is obtained from the area average of the PCTs for observed rain-free areas. In the ocean class, the correction values for the forward-calculated TB10v and TB18v of 0 mm/h were obtained in the same way.

3.5.3 Estimation of inhomogeneity of precipitation and CPF

We used high-resolution PCT89 for the estimation of Standard Deviation of Natural Logarithm of Precipitation (SDNLPR). First, we converted the PCT89 scattering signals into precipitation (Rain89) using LUTs for a prescribed value of SDNLPR (=1.0), and calculated the first guess of inhomogeneity (Sigma89) from Rain89 within TB10v FOVs. The LUTs for this inhomogeneity were used in the following retrieval procedures.

The algorithm estimated the FPD of each pixel (FPDpix) using GANAL atmospheric information and Rain89. A index of CPF for each pixel (CPFpix) was then estimated from the FPDpix, sigma89, and the 89 GHz polarization difference.

3.5.4 Retrievals using scattering signals

The algorithm utilizes PCT89 as the scattering signal for precipitation intensity retrieval. In this retrieval, a weighted average of the land/coastal/ocean ratios from the Look-Up Tables (LUTs) for each precipitation type is applied (the same approach is used for emission retrieval).

Over land and coastal regions, the algorithm corrects the retrieved precipitation intensity values via a Support Vector Machine (SVM) using physical variables related to CPF and FPD (namely, precipitation non-uniformity, the 85-GHz polarization difference, Ts, RH, and atmospheric stability). A comparison of the two-dimensional histograms of the retrieved precipitation values against the DPR precipitation intensity before and after the SVM correction reveals that the correction reduces the overall scatter (see Fig. 5).

3.5.5 Retrievals using emission signals over ocean

For the retrieval over ocean, emission signals at lower frequencies were available, in addition to the scattering signals. Following Aonashi et al (2009), the algorithm found the optimal precipitation over ocean by minimizing a cost function (*J*) that was a weighted sum of squares of differences between the observation and the forward calculation for TB10v and TB18v:

$$J = \sum_{f} \sum_{k=1}^{km} \frac{1}{2\sigma^2{}_f} \left\{ TB_f^o(\hat{y}_k) - TB_f^i\left[\hat{y}_k : r(\hat{x}_j)\right] \right\}^2, \tag{3}$$

where $r(\hat{x}_j)$ is the precipitation at point $\hat{x}_j$, $\hat{y}_k$ is the location of a TMI pixel, TB_f^o and TB_f^i represents the AMSR2 TBs and the FOV-averaged TBs calculated from $r(\hat{x}_j)$ at frequency *f*. σ_f

is the standard deviation of the differences between TB_f^o and TB_f^i. Here $\sum_f$ represents summation for f=10 and 18 GHz, and $\sum_{k=1}^{km}$ is summation for AMSR2 pixels over ocean.

We adopted the scattering retrievals as the first guess for this minimization. For shallow precipitation with zero scattering retrievals, we employed precipitation retrieved from TB36v as the first guess.

However, this technique is not applied in low temperature regions (FLH<500m) because the emission signal is weaker.

4 Validation

The AMSR3 precipitation (rainfall) product is validated against the precipitation product derived from DPR. DPR and AMSR3 precipitation estimates acquired within a 10-minute time difference are collocated and averaged onto equivalent 0.5° grids for comparison. The relative error with respect to the DPR precipitation is then calculated to evaluate the AMSR3 precipitation product.

5 Summary

The purpose of this document is to describe the rain retrieval algorithm (V01) for AMSR3. The major improvements implemented in this algorithm, compared to the previous version (AMSR2 V03), are as follows:

1) **Update of the precipitation detection method**: The precipitation detection method in the retrieval module has been updated to an approach which utilizes surface emissivity, and other parameters as inputs.
2) **Correction of scattering-based precipitation intensity retrieval**: In the precipitation intensity retrieval section that utilizes scattering signals, the retrieved precipitation values are now corrected using SVM, incorporating physical variables related to the Convective Precipitation Fraction and Frozen Precipitation Depth.

References:

Aonashi, K. and G. Liu, 2000: Passive Microwave Precipitation Retrievals using TMI during the Baiu period of 1998. Part 1:Algorithm description and Validation. *J. Appli. Meteor.* 39, 2024-2037.

Aonashi, K., Koike, T., Muramoto, K. I., Imaoka, K., Takahashi, N., Liu, G., and Noh, Y. J., 2007: Physical validation of microwave properties of winter precipitation over the Sea of Japan. *IEEE transactions on geoscience and remote sensing*, *45*(7), 2247-2258.

Aonashi, K. J. Awaka, M. Hirose, T. Kozu, T. Kubota, G. Liu S. Shige, S. Kida, S. Seto, N. Takahashi, and Y. N. Takayabu, 2009: GSMaP Passive Microwave Precipitation Retrieval Algorithm: Algorithm Description and Validation. *J. Meteor. Soc. Japan*, 87A, 119-136, 2009.

Aonashi, K., and R. R. Ferraro, 2020: Microwave sensors, imagers and sounders. *Satellite Precipitation Measurement*, V. Levizzani et al., Eds., Advances in Global Change Research, Vol. 1, Springer, 63–81.

Harimaya, T., 1977: The internal structure and embryo of graupel. J. Fae. Sci., Hokkaido Univ., Ser. VII, 5, 29-38.

Imaoka, K., M. Kachi, H. Fujii, H. Murakami, M. Hori, A. Ono, T. Igarashi, K. Nakagawa, T. Oki, Y. Honda, and H. Shimoda, 2010 : Global Change Observation Mission (GCOM) for monitoring carbon, water cycles, and climate change, *Proc. of the IEEE*, Vol. 98, No. 5, 717-734.

K. Inaoka, H. Morita, T. Miura, M. Kachi, R. Shimada, E. Yoshizawa, K. Ohara, K. Nakata, R. Komaru, S. Ikeda, S. Sakamoto, H. Matsuzawa, Y. Taniguchi, K. Murata, and N. Ebuchi, 2026: The Advanced Microwave Scanning Radiometer 3 (AMSR3) aboard GOSAT-GW, submitted to Proceedings of the IEEE.

Kubota, T., S. Shige, H. Hashizume, K. Aonashi, N. Takahashi, S. Seto, M. Hirose, Y. N. Takayabu, K. Nakagawa, K. Iwanami, T. Ushio, M. Kachi, and K. Okamoto, 2007: Global Precipitation Map using Satelliteborne Microwave Radiometers by the GSMaP Project : Production and Validation, *Trans. Geosci. Remote Sens.*, 45, 7, 2259-2275.

Kozu, T., T. Iguchi, T. Kubota, N. Yoshida, S. Seto, J. Kwiatkowski, and Y. N. Takayabu, 2009: Feasibility of Raindrop Size Distribution Parameter Estimation with TRMM Precipitation Radar. *J. Meteor. Soc. Japan*, 87A, 53-66, 2009.

Liu, G., 2004: Approximation of Single Scattering Properties of Ice and Snow Particles for High Microwave Frequencies. *J. Atmos. Sci.*, **61**, 2441–2456.

Mega, T., and S. Shige, 2016: Improvements of Rain/No-Rain Classification Methods for Microwave Radiometer over Coasts by Dynamic Surface-Type Classification. *J. Atmos. Oceanic Technol.*, **33**, 1257–1270, https://doi.org/10.1175/JTECH-D-15-0127.1.

Nishitsuji, A., M. Hoshiyama, J. Awaka, and Y. Furuhama,1983: An analysis of propagative character at 34.5 GHz and 11.5 GHz between ETS-II satellite and Kasima station – On the precipitation model from stratus. *IEICE Trans.* (in Japanese) , Vol. J66-B, 1163-1170.

Ogino, S.-Y., M. D. Yamanaka, S. Mori, and J. Matsumoto, 2016: How much is the precipitation amount over the tropical coastal region? *J. Climate*, 29, 1231–1236, https://doi.org/10.1175/JCLI-D-15-0484.1.

Shige, S., and C. Kummerow, 2016: Precipitation top heights of heavy orographic rainfall in the Asian monsoon region. *J. Atmos. Sci.*, **(2016)**.

Takayabu, Y. N., 2008: Observing rainfall regimes using TRMM PR and LIS data. GEWEX News, Vol 18, 9-11, May, 2008.

Turk, F. J., Z. S. Haddad, and Y. You, 2014: Principal Components of Multifrequency Microwave Land Surface Emissivities. Part I: Estimation under Clear and Precipitating Conditions. J. Hydrometeor., **15**, 3–19, https://doi.org/10.1175/JHM-D-13-08.1.

Yamamoto, M. K., S. Shige, C. Yu, and L. Cheng, 2017: Further Improvement of the Heavy Orographic Rainfall Retrievals in the GSMaP Algorithm for Microwave Radiometers. *J. Appl. Meteor. Climatol.*, **56**, 2607–2619, https://doi.org/10.1175/JAMC-D-16-0332.1.

Chapter 4.

Description of GOSAT-GW AMSR3 Snowfall Retrieval Algorithm

Guosheng Liu

Florida State University

Table of Contents

1. Introduction....4-3

2. Theoretical Basis for Algorithm Design....4-4

3. Snowfall Algorithm Description....4-7

3.1 Separation of Rain or Snow Suitable Conditions....4-7

3.2 Creation of *a-priori* Database....4-9

3.3 Brightness Temperature to Snowfall Rate Conversion....4-11

4. Validation....4-14

References....4-14

1. Introduction

The Advanced Microwave Scanning Radiometer 3 (AMSR3) on board the GOSAT-GW satellite observes radiances from the Earth at 21 channels covering 8 frequencies from 7 to 183 GHz, of which the high-frequency channels (>100 GHz) are particularly designed to measure solid precipitation (snowfall) because of their high sensitivity to the scattering by ice particles. Although rain and snow are just two different forms of precipitation, their climatological impacts are very different. Over land, accumulated snow may stay on the ground for months, resulting in different hydrological and radiative consequences from those by rain. Over ocean, falling snow has a complex interaction with ocean surface, because it both freshens and cools (through snow melting) the ocean surface water. A substantial portion of precipitation in the high latitudes is in the form of snowfall. Based on analysis of CloudSat (Stephens et al., 2002) data, it is suggested that the annually averaged zonal mean of snowfall near 60ºS can be more than 1.5 mm day^{-1}, which is about 1/4 of the zonally averaged rainfall value found in the inter-tropical convergence zone, signifying the importance of snowfall in the hydrological cycle (Liu, 2008a).

Snowfall observations had in the past been largely dependent on scarcely located ground stations. DPR (Dual-frequency Precipitation Radar) on the GPM (Global Precipitation Measurement) core satellite has some capability of measuring snowfall. However, due to its low sensitivity of detection (13 dBZ), it misses a substantial portion of snowfall cases with low to moderate snowfall intensity (Casella et al., 2017). While Cloud Profiling Radars (CPR) on CloudSat and EarthCARE can also be used to estimate snowfall, because the radars do not scan (therefore, it only observes a 1.5 km strip on the Earth for each satellite pass), its spatial coverage is very limited. Therefore, for global observation of snowfall we still must largely rely on measurements from passive microwave sensors with channels at high frequencies, such as the AMSR3.

The principle of passive microwave snowfall retrieval is to measure the scattering signature of falling snowflakes by high-frequency microwave radiometers. Using satellite data, snowfall detection and retrieval have been experimented by several investigators (e.g., Liu and Seo, 2013; Meng et al., 2017; Rysman et al., 2018; Gonzalez and Kummerow, 2025). In a previous study, Liu and Seo (2013) developed a snowfall detection algorithm that uses coincident CloudSat radar observations as guide to train high-frequency microwave radiometer data, and subsequently retrieves snowfall probability based on a look-up table in brightness temperatures' EOF (empirical orthogonal function) space. This AMSR3 snowfall algorithm will further advance this approach using a machine learning technique and develop the *a-priori* training database with collocated space radar and radiometer data from multiple platforms.

Several obstacles exist for accurate snowfall retrievals. First, snowfall signature in passive microwave observations is generally weak compared to that for rainfall. While heavy rainfall may cause brightness temperature to change by hundreds of Kelvins, snowfall barely moves the brightness temperature by 20~30 K even under heavy snowfall events. This fact of weak snowfall signature posts challenges both for snowfall identification and for brightness temperature to snowfall rate conversion. Second, over snow-covered surfaces, separation of signature of snow in the air and that on the ground is challenging. Third, it remains largely uncertain in evaluating the scattering properties for ice particles. The primary signature of snowfall in microwave radiation is the reduction of upwelling brightness temperature due to the scattering by snowflakes. The scattering signature strengthens with the increase of the amount and size of snow particles as snowfall intensifies. However, unlike raindrops that are (nearly) spheres with a known density of 1 g cm^{-3}, snowflakes are highly nonspherical and their bulk density varies with particles' size and shape. There are still many unknowns about the microphysics of snowflakes with realistic shapes/densities and their scattering properties, which are needed for quantitative estimation of snowfall rate from satellite-observed radiances. Additionally,

thermal emission from water vapor and cloud liquid water has a masking effect on snowflake scattering and reduces the snowfall signature. Under cold environment, the strongest signature of a snowstorm at some microwave channels may not necessarily be brightness temperature reduction due to scattering by snowflakes; a brightness temperature increase due to liquid water emission can also occur. In some cases, the liquid water influence becomes so strong that the snowstorm causes a warming (like rainfall over ocean) in microwave brightness temperatures.

The AMSR3 snowfall algorithm is developed based on the same strategy of Liu and Seo (2013). First, CloudSat/EarthCARE/GPM-DPR snowfall estimates and GPM GMI brightness temperature matchups are used to build an *a-priori* database. Snowfall retrieval is then performed using an inversion procedure trained on the a-priori database. In lieu of the look-up-table (or Bayesian) approach used in earlier versions, an XGBoost regression has been used for brightness temperature to snowfall rate conversion in the current version of the algorithm. The advantages of using this inversion procedure are discussed in later sections.

2. Theoretical Basis for Algorithm Design

AMSR3 measures upwelling microwave radiation at frequencies from 6.9 to 183 GHz, among which brightness temperatures at high-frequency (>100 GHz) channels are needed for snowfall retrievals. To illustrate the brightness temperature response to snowfall intensity, radiative transfer model simulated brightness temperature changes relative to clear-sky values at 89 GHz and 166 GHz are shown in Fig.1. The radiative transfer model developed by Liu (1998) has been used in this simulation, which uses a four-stream discrete ordinates method to solve the radiative transfer equation. For snow particles, the single-scattering properties calculated by discrete dipole approximation for sector type snowflakes (Liu, 2008b) are used. Based on studies of Geer and Baordo (2014), the single-scattering properties for the sector type snowflakes work reasonably well in radiative transfer simulations for middle latitude snowstorms.

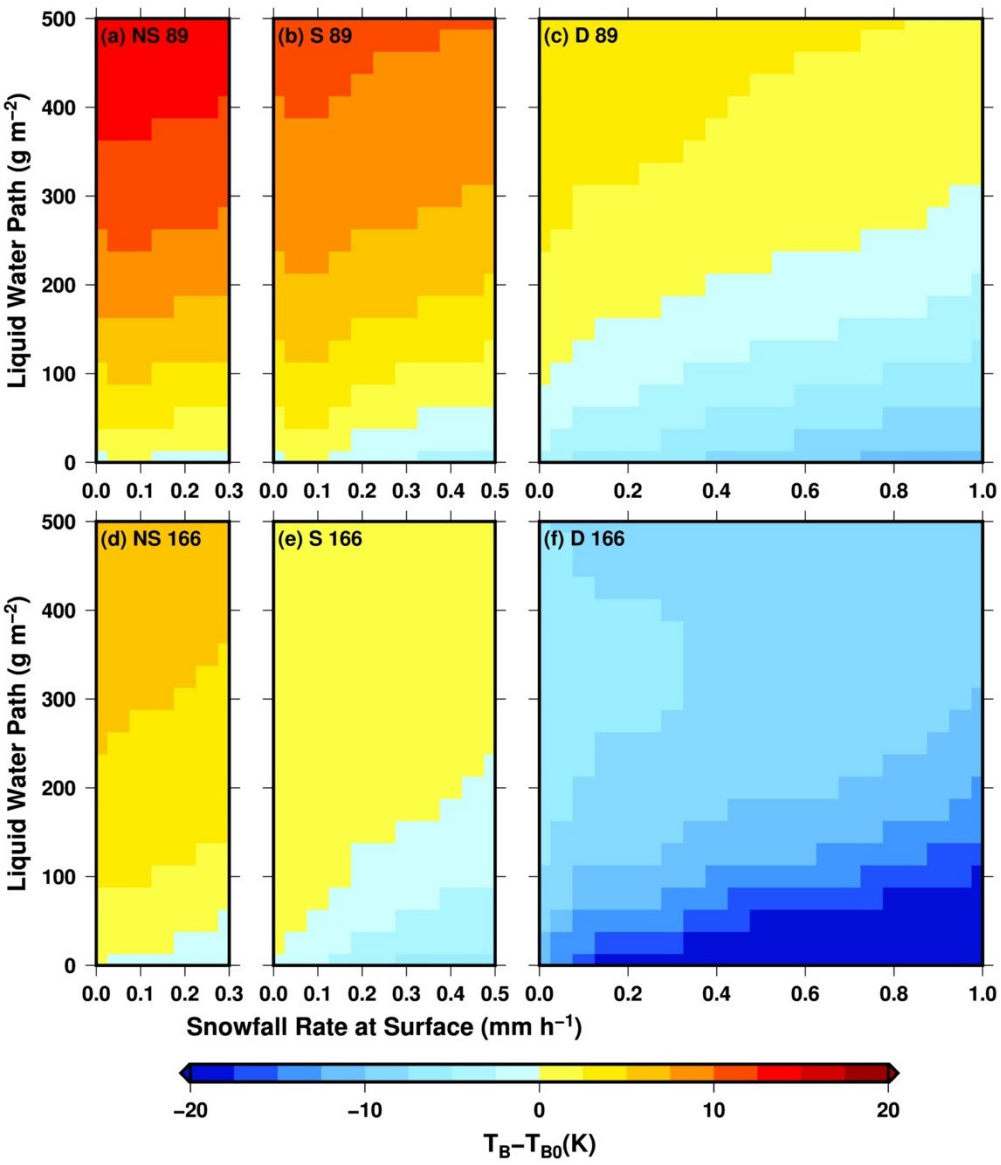

Fig.1 Simulated brightness temperature change (relative to clear-sky values) as surface snowfall rate and cloud liquid water increase for channels at 89 GHz (top) and 166 GHz (bottom) for 3 types of snow clouds – NS: near-surface (cloud top lower than 1.5 km, left panels), S: shallow (cloud top between 1.4 and 4 km, mid panels), and D: deep (cloud top higher than 4 km, right panels). The ranges of liquid water path and snowfall rate used in the simulations are based on values observed by a ground-based radar and radiometer. Adapted from Jeoung et al. (2020).

Three types of snow clouds are considered based on analysis of ground-based radar – radiometer observations by Jeoung et al. (2020). They are near-surface (NS) clouds with top lower than 1.5 km, shallow (S) clouds with top between 1.5 and 4 km, and deep (D) clouds with top exceeding 4 km. Ground-based observations also indicated that cloud liquid water path frequently varies from 0 to 500 g m^{-2} for any of the 3 types of snow clouds while snowfall rate at surface commonly reaches to 0.3, 0.5, and 1.0 mm h^{-1}, respectively,

for near-surface, shallow, and deep clouds. Using clear-sky brightness temperature T_{B0} as the base, Figure 1 shows how brightness temperatures vary as liquid water path and surface snowfall rate increase.

For near-surface snowing clouds, the decrease of brightness temperature due to ice scattering is very limited for either 89 or 166 GHz, only about 1.5 K for 89 GHz and 2.5 K for 166 GHz occurring when liquid water path is very low. Therefore, most likely this type of clouds displays a warming signature in the passive microwave observations due to the existence of liquid water clouds. For shallow snowing clouds, the modeling results show there is still mostly warming at 89 GHz and an equal mix of warming and cooling at 166 GHz. The masking effect remains quite significant at 89 GHz even for deep snowing clouds; it can cause an increase in brightness temperature by more than 5 K from clear-sky value. The dominant scattering signature shows at 166 GHz for deep clouds. At surface snowfall rate of 1 mm h^{-1}, brightness temperature can decrease from clear-sky value by more than 30 K (color bar only shows up to -15 K) when liquid water path is lower than 100 g m^{-2}.

Based on the above modeling results, if only relying on scattering signature, i.e., brightness temperature depression, an algorithm will totally fail in retrieving snowfall rate for near-surface clouds and partially fail for shallow clouds. Even for deep snowing clouds, cloud liquid water will impact snowfall retrieval with a result of an overestimation for low and an underestimation for high values of liquid water path. Therefore, a more plausible approach to the retrieval problem is to use a statistical method in which the algorithm utilizes any regularities naturally existing between cloud liquid and snow profiles to search for the most likely snowfall rate. This approach requires that the *a-priori* database used in the retrieval has the same characteristics in both microphysical properties and occurring frequency as those in natural clouds.

In addition to the above brightness temperature to snowfall rate sensitivity considerations, surface types and atmospheric conditions also influence satellite received microwave brightness temperatures. Therefore, their effects need to be considered when designing the retrieval algorithm. For this reason, we divide all conditions into 10 regimes as shown in Table 1 based on surface type (open water, land without snow cover, snow-covered land, sea ice, Greenland region and coast) and total precipitable water (TPW). Note that the TPW threshold used for determining the "wetness" of the atmosphere is somewhat arbitrary; they are primarily determined by the availability of data points of the CloudSat-GMI matchups, so that every regime contain sufficient data points for algorithm training. Each regime has its own training database and brightness temperature to snowfall conversion model. At the retrieval step of the algorithm, a pixel's regime is first determined by its surface type and TPW, then the solution is determined by the conversion model that corresponds to the pixel's regime. A separate "Greenland" regime is designated because it is found that its frozen surface has very different microwave brightness temperature characteristics from those of other snow-covered surfaces. It is reasonable to suspect that Antarctic could also be of similar characteristics. However, because GMI observations do not reach the inland of Antarctic, whether Antarctic belongs to the same regime as Greenland is still unclear, which will be investigated later using AMSR3 and EarthCARE observations.

Table 1 Surface and Atmosphere Regimes

Regime No.	Description
1	open water, dry (TPW <5.0 kg m^{-2})
2	open water, moderate wet (TPW 5.0-7.0 kg m^{-2})
3	open water, wet (TPW >7.0 kg m^{-2})
4	land (no snow cover)

5	snow cover land, dry (TPW <2.5 kg m^{-2})
6	snow cover land, moderate wet (TPW 2.5-5.0 kg m^{-2})
7	snow cover land, wet (TPW >5.0 kg m^{-2})
8	sea ice
9	over Greenland
10	Coast

3. Snowfall Algorithm Description

The AMSR3 snowfall retrieval algorithm consists of 3 components: (1) separation of snow-rain conditions, (2) creation of *a-priori* database, and (3) brightness temperature to snowfall rate conversion. A flowchart of the AMSR3 snowfall retrieval algorithm is shown in Fig.2.

3.1 Separation of Rain or Snow Suitable Conditions

Before performing precipitation retrievals, it is necessary to know whether the precipitation is rain or snow when it reaches ground. If it is rain, a rain retrieval algorithm will be employed and snowfall rate will be assigned to 0. Otherwise, if it is snow, the snowfall algorithm as described in this section will be used. Most raindrops (particularly in the high latitudes) are originated from ice particles aloft; precipitation becomes rainfall when ice particles melt in warm ambient temperature. Therefore, air temperature is obviously the most reliable indicator to determine snowfall-favorable conditions. Based on an analysis of decades worth of land surface station and shipboard current weather reports, Liu (2008a) found that the transition from surface rain to snow mostly occurs at 2-m air temperature between 4°C to -1°C with a median value of about 2°C. This is a physically reasonable value because while ice melting starts at 0ºC, the process of melting a snowflake takes time and the snowflake keeps falling toward ground as the melting proceeds.

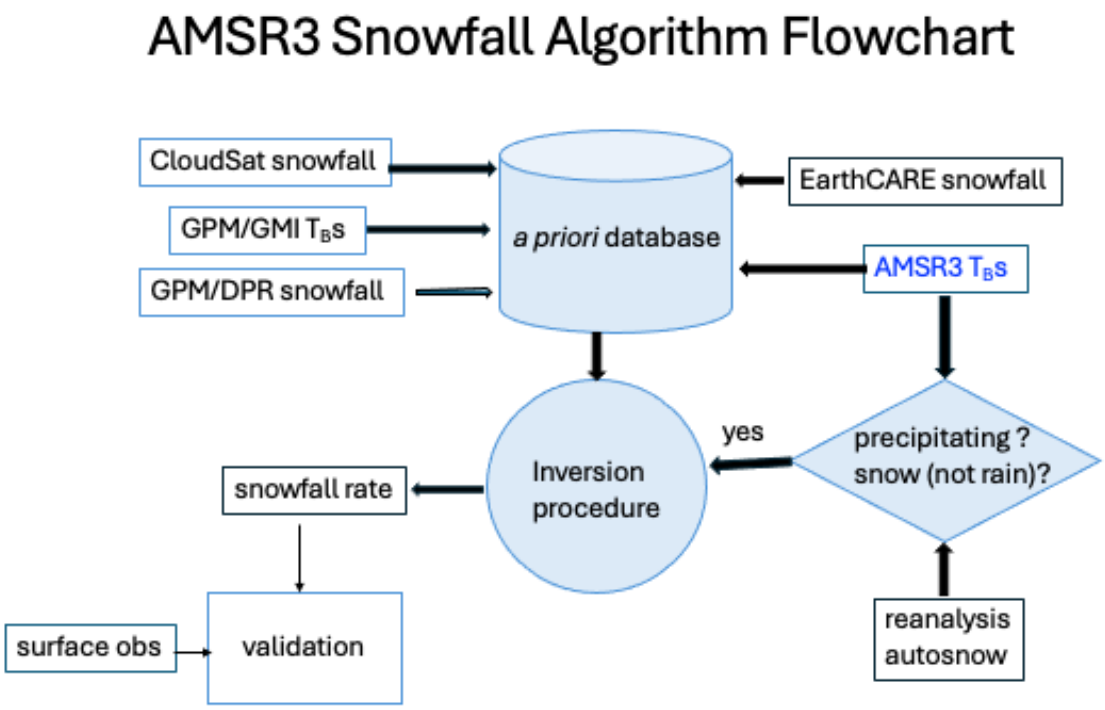

Fig.2 AMSR3 snowfall retrieval algorithm flowchart. The creation of the a-priori database and algorithm training are carried out offline, while rain-snow separation and brightness temperature to snowfall conversion are carried out during retrieval executions.

However, the rain-snow transition is a complicated physical process involving many impacting factors. In a common situation where lapse rate is positive (i.e., temperature decreases with height), ice particles aloft start melting after falling across 0°C level. Depending on freezing level height, particles' melting rate and falling speed, precipitation at ground can be either liquid, solid or mixed phase. The melting particles' surface temperature is between wet-bulb and ice-bulb temperature (because they are partial liquid and partial solid). If ambient relative humidity is low so that particle's surface temperature does not reach 0°C (even if ambient temperature is higher than 0°C), the particle will not start melting. In case of a negative lapse rate (temperature inversion), melting may have already started aloft even when surface air temperature is below 0°C. Whether solid or liquid phase precipitation is observed at ground depends on how fast the particle is re-freezing and how fast it is falling.

Using global ground-based observations over multiple decades, Sims and Liu (2015) have studied the influence on particle phase by several geophysical parameters on precipitation phase. In their published work, the following parameters are examined: near-surface air temperature, atmospheric moisture, low-level (0-500 m) vertical temperature lapse rate, surface skin temperature, surface pressure, and land cover type. Considering that snow melting occurs at (or close to) wet-bulb temperature instead of actual air temperature, the snow-rain transition was examined using wet-bulb temperature, instead of air temperature itself. Results show that in addition to wet-bulb temperature, vertical temperature lapse rate (0-500m) affects the precipitation phase significantly. For example, at a near-surface wet-bulb temperature of 0°C, a lapse rate of 6°C km^{-1}

results in an 86% probability of solid precipitation, while a lapse rate of -2°C km^{-1} (inversion) results in a 45% probability. For 2-m wet-bulb temperatures less than 0°C, ground skin temperature also affects precipitation phase, although the effect appears to be minor. Based on these findings, we have developed a parameterization that accepts available meteorological data as input and returns the probability of solid precipitation. The geophysical parameters included in the parameterization are near-surface (2-m) temperature, relative humidity, low-level vertical lapse rate, ground skin temperature and surface type.

In the current snowfall algorithm, the Sims and Liu algorithm is used; a pixel is determined to be snow-favorable when the above probability of snowfall is greater than 50%. Otherwise, it is determined to be rainfall. The input environmental parameters to the separation algorithm are from JMA GANAL reanalysis. Future improvement based on a recent study of Shi and Liu (2024) is under consideration.

3.2 Creation of *a-priori* Database

The *a-priori* database is used to train the inversion part of the algorithm (to be described later in next section), and is regarded as "the truth" in relating observables (brightness temperature) to retrievals (snowfall rate). Therefore, this part of the algorithm is the most important component for the accuracy of the retrievals. A high-quality *a-priori* database requires: (1) the statistical characteristics of snowfall events such as occurrence frequency, associated temperature and water vapor fields, vertical structures, etc., resemble what occur in nature, and (2) the brightness temperatures associated with an observed scene (pixel) are accurate. If we generate the training database using numerical model simulations, the first requirement implies that the numerical weather prediction or cloud-resolving models need to be able to simulate snow clouds with the same cloud physical properties as reality, and the second requirement then asks that radiative transfer model can correctly compute brightness temperatures given a snow cloud microphysical field. Since both requirements are difficult to be met as of today, instead of relying on numerical models, we decided to build the training database based on observations. For the database to have a global coverage, collocated satellite observations from CloudSat and EarthCARE CPRs, GPM DPR and GPM GMI are used. It is planned that collocated EarthCARE CPR radar and AMSR3 radiometer observations are added later for database enhancement.

GPM GMI brightness temperatures are used as the proxy of AMSR3 brightness temperatures in constructing the *a-priori* database. At frequencies above 10 GHz, AMSR3 channel specifications are similar to those of GMI's except for no 166H channel in AMSR3. Therefore, we use GMI brightness temperatures in place of AMSR3's in creating the *a-priori* database. For snowfall rates, we use retrievals from cloud radar observations of the CloudSat CPR, EarthCARE CPR and GPM DPR.

CloudSat satellite was launched in 2006 and its CPR observations cover the latitudes between 82°S and 82°N at W-band. Analysis of in-orbit data has shown that the CPR's minimum detectable radar reflectivity factor is about -27 dBZ, sensitive enough to detect snowfall. However, the CPR has difficulties of measuring heavy snowfall due to hydrometeor's attenuation and non-Rayleigh scattering effects, which limits the upper bound of the CPR reflectivity to about 20 dBZ. CloudSat CPR ceased operation in 2023 although we only used its data up to August 2020 for database creation. Since the GPM core satellite was launched in 2014 and observations cover latitudes between 65°S and 65°N, the collocated CloudSat CPR and GPM GMI data cover the period of 2014 to 2020 and latitudes equatorward of 65°. The collocated dataset is described in Turk et al. (2021). The matchups require the time difference within 15 minutes and the maximum pixel-center distance less than 3 km between GMI and CPR observations. Snowfall rate is derived from snowfall rate retrievals of the lowest uncontaminated level in 2C-SNOW_PROFILE product (Wood et al. 2014).

EarthCARE satellite was launched in 2024 and is currently in operation. Similar to CloudSat, its CPR operates at W-band with a sensitivity of about -36 dBZ, and covers the latitudes between 82°S and 82°N. A collocated EarthCARE – GPM dataset was put together by Aoki et al. (2026). Because EarthCARE CPR does not have a standard product of snowfall rate, we use a radar reflectivity (Z) - snowfall rate (S) relation derived by Heymsfield et al. (2018):

$$S = 0.083e^{0.211dBZ}.$$

In deriving the above relation, data of CloudSat CPR radar reflectivity and 2C-SNOW-PROFILE snowfall rate from December 2007 through December 2008 are used. Currently, EarthCARE CPR – GPM GMI matchups from 2024 and 2025 are used in the *a-priori* database, although its volume will be increased as more observations accumulate.

The GPM DPR operates at Ku- and Ka-band with a minimum detectability of about 13 dBZ. The DPR derived snowfall can be used to compensate the weakness of CloudSat/EarthCARE CPR snowfall retrieval for heavy snowfall events. Using GPM DPR alone to estimate snowfall has its own weakness. Due to its low detectability, many light snowfall cases cannot be detected by the DPR radar (Liu, 2020). For this reason, we only use the DPR-GMI matchup data as "a supplement" to compensate for the deficiency of CPR's inability for measuring heavy snowfall events. For DPR snowfall rate, we use official surface precipitation rate product when our algorithm determines a pixel is under snow-favorable condition. Since DPR and GMI are onboard the same GPM Core satellite, the number of collocated pixels is overwhelmingly larger than that of CPR-GMI matchups. Only one year (2018) of nadir DPR data are used for the *a-priori* database creation.

In the left panel of Fig.3, we show the number distribution of matched data points as a function snowfall rates for the 3 sets of matchups. Note that points with 0 snowfall rate are not included in the plot which are about 75%, 60% and 93% of their corresponding total points, respectively, for CloudSat-GMI, EarthCARE-GMI and DPR-GMI matchups. Also noted that the data points from DPR-GMI matchups are several orders bigger than the other two sources, which is undesirable because it would result in the trained algorithm being disproportionally skewed to the DPR-GMI matchup dataset if the three datasets are treated equally when training algorithms. This problem is handled by using a "sample weight" parameter in the XGBoost retrieval to adjust the weight of each sample point, which is described in the next section. After adjusting, the "effective" number of samples (i.e., number times weight) are the solid curves as indicated in the right panel of Fig.3. As expected, CPR detects more light snow cases while DPR detects more heavier ones.

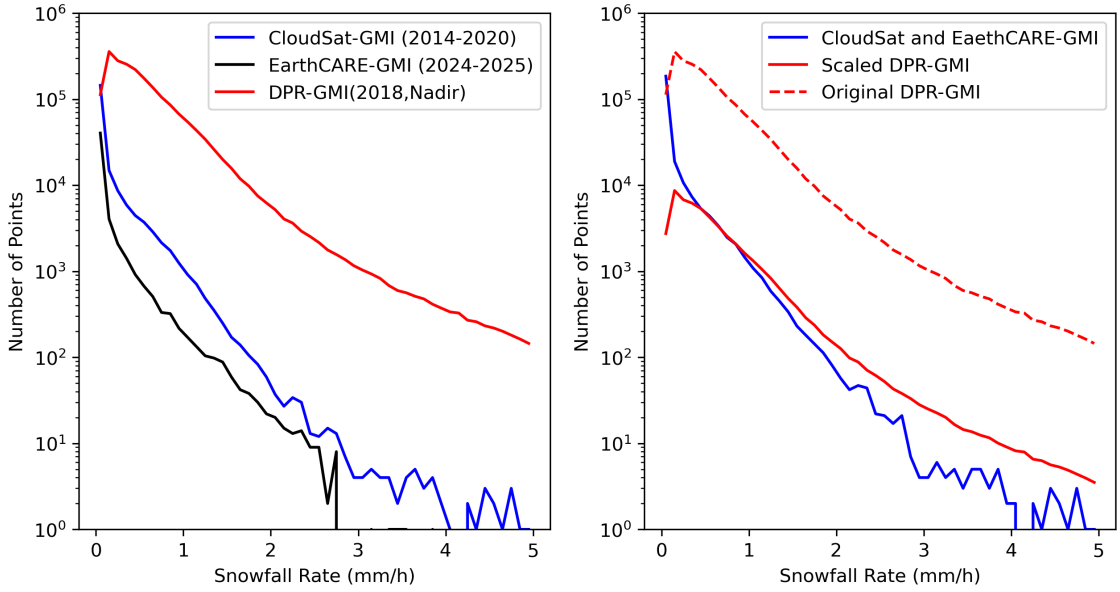

Fig.3 (left) The number distribution of data points with snowfall rate in the training database from 3 matchup sources. (right) Same as left, but CloudSat and EarthCARE CPR with GMI matchups are combined, and DPR-GMI matchups are scaled. Note that values for 0 snowfall rate are not plotted.

3.3 Brightness Temperature to Snowfall Rate Conversion

An earlier version of the snowfall algorithm uses a Bayesian method to convert AMSR3 brightness temperatures to snowfall rates. There are several limitations to the Bayesian method: (1) it is difficult to combine CPR-GMI and DPR-GMI matchups because DPR and CPR are sensitive to different ranges of snowfall rates, (2) lower snowfall rates are often overweighted in the retrieval because they occur more frequently while higher rates are underestimated due to low frequency of occurrence, and (3) retrieval computation is very time-consuming because the *a-priori* dataset contains a large number of data points and each point is examined for every satellite pixel when executing brightness temperature to snowfall rate conversion. In recent years, machine learning techniques have been increasingly used in many research areas including satellite remote sensing. To take advantage of the rapid development of machine learning techniques, we apply the XGBoost (Extreme Gradient Boosting) method (Chen and Guestrin, 2016) to perform brightness temperature to snowfall rate conversion.

XGBoost is an ensemble machine learning method that builds many decision trees sequentially, where each tree learns to correct the errors made by the previous ones. During prediction (retrieval), the input variables (brightness temperatures) are passed through all the trees in the trained model. Each tree contributes a small score, and the scores are combined to produce the final prediction (snowfall rate). There are several hyperparameters in the XGBoost model that are tunable in the training phase for the best performance of retrieval. Because the training (building the retrieval model) phase and the prediction (performing retrieval) phase are separated, the computation time for retrievals is very short regardless the size of training dataset. There is an assignable “sample weight” parameter in the method which allows us to give a “weight” to each data point in the training dataset, effectively to control which data points are more important than the others when training the retrieval model.

In Fig.3 (right panel), we show how the DPR-GMI matchups' weights are scaled down to match the contributions of CPR-GMI matchups. We postulate that when a snowfall rate is around 0.5 mm h^{-1}, both CPR and DPR radars are likely to be able to detect it, thus the frequencies of observation by both radars should be the same (if sample volumes of both are large enough). So, we assign a smaller "sample weight" to all DPR-GMI samples, effectively bringing the frequency of measurements of DPR-GMI matchups at 0.5 mm h^{-1} snowfall rate to that of CPR-GMI matchups, as indicated by the solid line in the right panel of Fig.3. This adjustment using "sample weight" can be done each time we change the number of data points in the training datasets due to the continuous increase of EarthCARE CPR-GMI matchups as both EarthCARE and GPM satellites are in operation.

Another adjustment using the "sample weight" parameter can be done to boost the weights of heavier snowfall, as shown in Fig.4. The earlier Bayesian version of the algorithm has a shortcoming of underestimation of heavy snowfall events (because they are rarely observed, therefore very few cases exist in the training datasets). Using the "sample weight" parameter, we can effectively boost the influence of heavy snowfall events. Note that at this point the snowfall rate dependent "sample weights" are given by the reciprocal of the number faction in a snowfall rate bin, so that the snowfall rate bins with smaller data numbers receive bigger weights following the formula:

$$SW = SW_{min} + (SW_{max} - SW_{min})\frac{N_{lastbin}}{N_{bin}}$$

where SW is the weight at the center of nth snowfall rate bin. SW_{min}=0.05 is the minimum, and SW_{max}=1.0 is the maximum weight. $N_{lastbin}$ is the number of data points in the highest snowfall rate bin (~ 5 mm h^{-1}) and N_{bin} is the number of data points in the nth bin. The distribution of SW for the snow cover regimes (regime 5, 6, and 7 combined) is shown in Fig.4. Note that the sample weights for DPR-GMI matchup data points have also been scaled down as described in the previous section. Whether this formulation is the best to determine sample weights reserves to be further studied in the future.

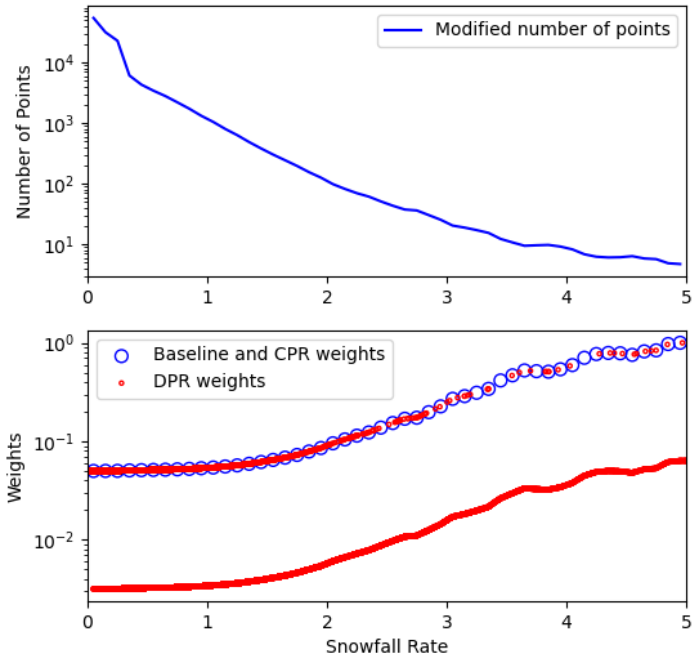

Fig.4. (top) Modified number of points (sum of the 2 solid curves in the right panel of Fig.3) in the training dataset. (bottom) "Sample weights" to be assigned to data points in the training dataset according to their snowfall rates.

For each regime listed in Table 1, we have developed two XGBoost models trained by the *a-priori* database: one for classification which separates precipitation and non-precipitation pixels, and the other for regression which calculates snowfall rate. The classification model requires AMSR3 brightness temperatures (18V, 18H, 23V, 36V, 36H, 89V, 89H, 165V, 183±3, 183±7), 2-m temperature, 2-m relative humidity and total precipitable water as input, and determines whether a pixel is precipitating (1) or not (0). The regression model requires the 10 brightness temperatures as listed above as input, and outputs snowfall rate. AMSR3 data with lower frequencies than 18 GHz are not used in the snowfall retrieval.

Finally, there are several hyperparameters that can be adjusted in developing XGBoost models, which are tunable for the best performance of the algorithms. Our test indicated that a large value of "number of estimators" with a small value of "learning rate" gives the best algorithm performance. Currently, we chose learning rate of 0.1 and 0.05 with "numbers of estimators" of 400 and 800 for classification and regression, respectively. All other hyperparameters are tuned accordingly for the best *AUC* (area under the curve) for classification and *RMSE* (root mean squared error) for regression. In future, these hyperparameters will be further tested for better algorithm performance and then implemented in later algorithm upgrades.

4. Validation

Two approaches will be considered for validating the snowfall retrieval algorithm. One is to collect quality-controlled historical surface snowfall data (gauge and/or radar data) at multiple locations, and to compare whether the retrievals are in-line with the "snowfall climatology" at those locations. This approach does not require additional field observations and can verify the retrieval algorithm in an averaged sense. We plan to use the following datasets for this type of validation:

o GHCND: Global Historical Climatology Network – Daily product (Menne et al., 2012). This dataset contains daily snowfall data at over 100,000 stations around the globe, although the length of data records varies dependent on station (from 1 year to 180 years). We have some experience with this dataset; its quality at least over N. America seems to be quite good.

o SNOTEL: Snowpack Telemetry (SNOTEL) daily product. SNOTEL is operated by the U.S. Department of Agriculture. SNOTEL sites, mostly located over mountain areas in the western U.S., are remote weather stations that measure snow accumulated on the device and transmit the data wirelessly; the data we used here are snow water equivalent.

o MRMS: Multi-Radar Multi-Sensor precipitation product (Zhang et al., 2016). This is a gauge corrected ground-radar network precipitation product over N. America although no gauge correction is applied for snowfall (it is simply converted from NexRad reflectivity using $Z=75S^2$, where Z is radar reflectivity and S is snowfall rate). There are known problems with this product such as substantial underestimation when the location is far from the radar site (>50 km) or the radar beam is high from the surface. We will keep these weaknesses in mind when using this dataset for validation. The broad area coverage is its strength.

o AMeDAS: Gauge corrected ground-radar network precipitation product over Japan. This product is similar to MRMS; it has similar strength and weakness to MRMS.

The second approach for validation is to compare retrievals for individual cases. This approach will be able to find whether the algorithm can resolve the pattern of snowfall system correctly, and thus help us understand whether the algorithm has weakness with certain types of cloud systems (for example, shallow convective clouds). MRMS and AMeDAS snowfall distributions will be the suitable datasets for this type of validation. Based on the outcome of validations, the snowfall retrieval algorithm will be modified to improve its performance.

References

Aoki, S., Kubota, T., and Turk, F. J. (2026): Exploring vertical motions in convective and stratiform precipitation using spaceborne radar observations: Insights from EarthCARE and GPM coincidence dataset, Atmos. Meas. Tech., 19, 79-100.

Casella, D. et al., 2017: Evaluation of the GPM-DPR snowfall detection capability: Comparison with CloudSat-CPR. Atmos. Res., 197, 64-75.

Chen, T., & Guestrin, C. (2016). XGBoost: A Scalable Tree Boosting System. In Proceedings of the 22nd ACM SIGKDD International Conference on Knowledge Discovery and Data Mining (pp. 785–794). https://doi.org/10.1145/2939672.2939785.

Geer, A. J. and Baordo, F. (2014). Improved scattering radiative transfer for frozen hydrometeors at microwave frequencies, Atmos. Meas. Tech., 7, 1839–1860, https://doi.org/10.5194/amt-7-1839-2014.

Gonzalez, R., & Kummerow, C. D. (2025). An Evaluation of GPROF-Based Snowfall Retrievals and Their Training Data. Journal of Hydrometeorology, 26(5), 627–638. https://doi.org/10.1175/JHM-D-24-0106.1.

Jeoung, H., Liu, G., Kim, K., Lee, G., and Seo, E.-K. (2020): Microphysical properties of three types of snow clouds implication for satellite snowfall retrievals, Atmos. Chem. Phys., 20, 14491–14507, https://doi.org/10.5194/acp-20-14491-2020.

Liu, G., 1998: A fast and accurate model for microwave radiance calculations. J. Meteor. Soc. Japan, 76, 335-343.

Liu, G., 2008a: Deriving snow cloud characteristics from CloudSat observations, J. Geophys. Res., 113, D00A09, doi:10.1029/2007JD009766.

Liu, G., 2008b: A database of microwave single-scattering properties for nonspherical ice particles. Bull. Am. Met. Soc., 89, 1563-1570.

Liu, G., 2020: Radar Snowfall Measurement. In: Levizzani V., Kidd C., Kirschbaum D., Kummerow C., Nakamura K., Turk F. (eds) Satellite Precipitation Measurement. Advances in Global Change Research, vol 67. Springer, Cham.

Liu, G. and E.-K. Seo, 2013: Detecting snowfall over land by satellite high-frequency microwave observations: The lack of scattering signature and a statistical approach. J. Geophys. Res. Atmos., 118, 1376–1387.

Menne, M.J., I. Durre, R.S. Vose, B.E. Gleason, and T.G. Houston, 2012: An overview of the Global Historical Climatology Network-Daily Database. J. Atmos. Ocean. Tech. 29, 897-910.

Meng, H., et al., 2017: A 1DVAR-based snowfall rate retrieval algorithm for passive microwave radiometers. J. Geophys. Res. 122, 6520–6540.

Rysman, J.-F., G. Panegrossi, P. Sanò, A. Marra, S. Dietrich, L. Milani, and M. Kulie, 2018: SLALOM: An all-surface snow water path retrieval algorithm for the GPM Microwave Imager. Remote Sens., 10, 1278.

Shi, S., and G. Liu, 2024: Improvements on phase classification using atmospheric melting and refreezing energy based on soundings. Journal of Geophysical Research: Atmospheres, 129, e2023JD040030. https://doi.org/10.1029/ 2023JD040030.

Sims, E. and G. Liu, 2015: A parameterization of the probability of snow-rain transition. J. Hydrometeor. 16, 1466-1477.

Stephens, G. L., et al., 2002: The CloudSat Mission and the A-Train. Bull. Amer. Meteor. Soc., 83, 1771-1790.

Turk, F. J., Ringerud, S. E., Camplani, A., Casella, D., Chase, R. J., Ebtehaj, A., Gong, J., Kulie, M., Liu, G., Milani, L., Panegrossi, G., Padullés, R., Rysman, J.-F., Sanò, P., Vahedizade, S., & Wood, N. B. (2021). Applications of a CloudSat-TRMM and CloudSat-GPM Satellite Coincidence Dataset. *Remote Sensing*, *13*(12), 2264. https://doi.org/10.3390/rs13122264

Wood, N. B., T. S. L'Ecuyer, A. J. Heymsfield, G. L. Stephens, D. R. Hudak, and P. Rodriguez (2014), Estimating snow microphysical properties

using collocated multisensor observations, J. Geo-phys. Res. Atmos., 119, 8941–8961, doi:10.1002/2013JD021303.

Zhang, J., et al., 2016: Multi-Radar Multi-Sensor (MRMS) quantitative precipitation estimation: Initial operating capabilities. Bull. Amer. Meteor. Soc., 97, 621-638.

Chapter 5.

Description of GOSAT-GW AMSR3 Sea Surface Temperature Algorithm

Akira Shibata

Remote Sensing Technology Center of Japan

Table of Contents

1. Introduction 5-3
2. Algorithm Overview 5-3
3. Theoretical Description 5-4
4. Algorithm Implementation 5-11
   4.1 Implementation 5-11
   4.2 Input/output parameters 5-11
   4.3 Ancillary data 5-11
   4.4 Processing flow 5-11
   4.5 Example output 5-11
   4.6 Limitations 5-12
5. Validation Concept 5-12

References

1. Introduction

Passive microwave radiometers are capable of measuring sea surface temperature (SST) under cloud cover. Usable frequencies for measuring SST range from 4 to 10 GHz. It has been noticed that the sensitivity to low SST becomes less as the frequency is increased (Hollinger and Lo, 1984). The first spaceborne microwave radiometer capable of measuring SST was the Scanning Multichannel Microwave Radiometer (SMMR) carried on Seasat 1 and Nimbus 7, both of which were launched in 1978. Although SST retrievals from the SMMR on Nimbus-7 had an error as high as 1.12°C, most of the SST error was due to calibration problems unique to the SMMR design (Milman and Wilheit, 1985). The second radiometer capable of measuring SST was the TRMM Microwave Imager (TMI) on the Tropical Rainfall Measuring Mission (TRMM) launched in 1997. The SST accuracy retrieved from TMI at 10 GHz is much better than that of the SMMR (Shibata et al., 1999), and the cited results seem to promise accurate SST retrievals at 6 GHz with future radiometers. The third sensors were two AMSRs; one is the AMSR-E onboard the NASA Aqua launched in May 2002, and the other is the AMSR onboard the ADEOS-II launched in December 2002. The AMSRs were the first sensors to provide an accurate microwave SST for the global ocean, and the averaged rms of the difference between AMSR and buoy SSTs was 0.47°C for AMSR2 over 10 years, 0.59°C for AMSR-E over an 18 month period, and 0.74°C for AMSR over seven months (Shibata, 2004). This paper will describe the SST algorithm for AMSR3, onboard the GOSAT-GW.

2. Algorithm Overview

We retrieve the SST using the brightness temperatures at 6 GHz with vertical polarization (V-pol), referred to henceforward as 6V. In addition to the SST, 6V contains various signals related to other parameters. These are (a) atmospheric effect, (b) wind effect, (c) salinity effect, (d) land contamination, (e) sea ice contamination, and (f) sun glitter contamination. Among the first three effects, (c) is very small. We can correct (c) by using the monthly climate salinity. Effects (a) and (b) are large, and we will explain in detail methods for correcting them. Contaminations due to (d) to (f) are also significant, so we eliminate contaminated areas as much as possible. In our algorithm, areas missing owing to (d) are within about 100 km of the shorelines, and areas missing owing to (f) occur where there is an angle of 25° or less between the AMSR viewing direction and the sun glitter direction. In (e), the sea ice case, we eliminate those pixels where sea ice is detected by AMSR. Effects (a) to (c) and contaminations (d) to (f) are common to microwave radiometers in general. In addition to these, we need to correct other errors specific to AMSR. These are (g) incidence angle variation, (h) scan bias error, and (i) radio frequency interference (RFI). In the case of AMSR, the

main cause of (h) is a cold sky mirror blocking a main reflector viewing at the rightmost scanning position. A temperature drop of −1.5 K may be registered over the ocean by 6V when scanning at the rightmost position (for a 243 pixels swath). At frequencies other than 6 GHz, no scan bias is discernible. RFI at 6.9 GHz is very severe over continents and sometimes around islands in the ocean.

In our algorithm to retrieve the SST, we require an initial SST value as one of the inputs. We specify this initial value from the Reynolds SST for AMSR and AMSR-E, and from the Merged satellite and in-situ data Global Daily SST (MGDSST) of the Japan Meteorological Agency (JMA) for AMSR2.

3. Theoretical Description

Atmospheric Corrections

The atmospheric effects at 6 GHz are mainly attributed to molecules (water vapor and oxygen) and cloud liquid water. These effects can be estimated by using 23V and 36V (V-pol of brightness temperature at 23 GHz and 36 GHz, respectively). The 23 GHz channel is sensitive to water vapor (there is an absorption line of water vapor at 22.235 GHz), while the 36 GHz channel is sensitive to cloud liquid water. Only V-pol is used because it is less sensitive to ocean wind than the horizontal polarization (H-pol) (Shibata, 2003). Fig. 1 shows an example of atmospheric correction for 6V (units: K) at an SST of 20°C, where the horizontal axis is 36V and the vertical axis is 23V. To make the atmospheric corrections, we subtract these values from the AMSR 6V.

Fig. 1 Atmospheric correction value for 6V.

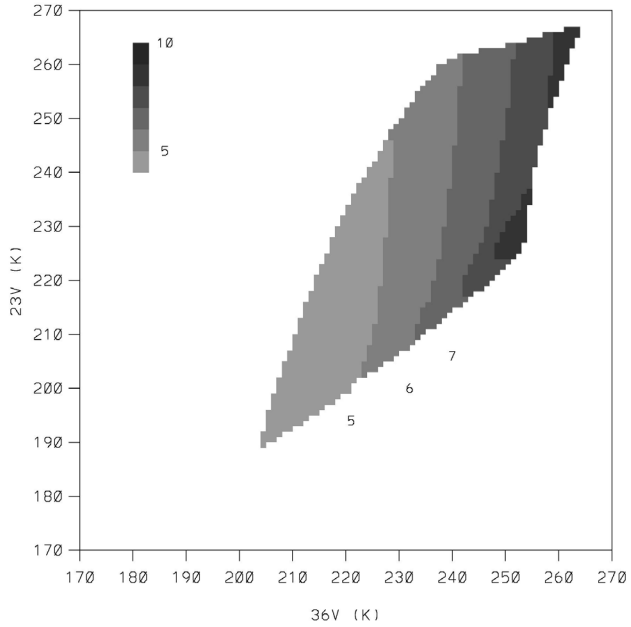

We obtained Fig. 1 by using a microwave transfer model typically applied to one-year Japanese aerological observations (Shibata, 1994). The microwave model consists of 60 levels ranging from the surface to 12 km, each 200 m in depth, followed by 18 levels for each 1 km of depth from 12 to 30 km. Within each level, the microwave signal decays owing to absorption by molecules and cloud liquid water. Molecules and cloud liquid water emit microwaves corresponding to the ambient temperature. In the first step of the sequential calculations, an external microwave of 2.7 K arrives from the cosmos, and the down-welling microwave is calculated for each level in the manner described above. At the ocean surface, the microwave is reflected, with a reflection intensity given by Fresnel's formula (r). The ocean surface emits microwave radiation equal to SST × (1 - r). For 6V, the value of r depends on SST and is roughly 0.6. The microwave signal in an upward direction from the ocean surface is calculated in the same manner as for the downward direction. Finally, the microwave radiation at 30 km is obtained. The values shown in Fig. 1 were obtained by subtracting the ocean surface radiation (i.e., SST × (1 - r)) from the values calculated at a height of 30 km; this is expressed by Eq. (1).

$$\text{atmos\_effect\_6V(H)} = \text{simu\_6V(H)} - \text{calm\_ocean\_6V(H)}, \quad (1)$$

where calm_ocean_6V(H) is given by the Fresnel formula.

Japanese aerological stations are located between the sub-tropical and sub-arctic regions, and the accumulated water vapor content calculated from this dataset ranges from 3 to 60 kg/m^2 (or mm). Values for 23V vary from 190 K to 260 K owing to these variations in water vapor. The cloud liquid water is inserted into the microwave transfer model at heights between 1 and 5 km, where its values range between 0 and 2 kg/m^2. Values for 36V vary from 205 K to 260 K, mainly because of variations in cloud liquid water.

Atmospheric effects on 6V are calculated from 0°C to 35°C SST at intervals of 5°C, and are interpolated for the intermediate SSTs. Fig. 1 applies to 6V, and we have a similar figure for 6H. In rainy conditions, the microwaves at 36 and 23 GHz are scattered by raindrops, and we are unable to use those data quantitatively without considering these scattering effects. In our algorithm, the SST is set as missing under rainy conditions, defined as occurring when the atmospheric effects on 6V are larger than 6.6 K (we determined the value of 6.6 K from the actual AMSR data).

Wind Effect Corrections

Wind effects have two components: wind speed and wind direction. To observe these effects at 6 GHz, we created Fig. 2 by combining data from AMSR and SeaWinds on ADEOS-II. Fig. 2 (a) shows the relation of 6V to relative wind direction (RWD); (b) shows the relation of 6H to RWD, and (c) shows the relation between 6V and 6H. The units of the vertical axis in Figs.2 (a) and (b),

and of both axes in Fig. 2 (c), are Kelvin, annotated as 6V (K). To create Fig. 2, we used two days of AMSR and SeaWinds data for the global ocean, for May 15 and 19, 2003. The RWD is defined as the relative angle between AMSR viewing direction and the SeaWinds wind direction. An RWD of 180° corresponds to an upwind direction; 90° and 270° correspond to a crosswind direction; and 0° (and 360°) correspond to a downwind direction. SeaWinds wind speeds from 1 to 17 m/s at 4 m/s intervals are shown in Fig. 2.

6V and 6H in Fig. 2 were already corrected for the atmospheric effect and SST effect, as expressed in Eq. (2).

$$6V(H) = AMSR\_6V(H) - atmos\_effect\_6V(H) - calm\_ocean\_6V(H), \quad (2)$$

Fig. 2 Characteristics of (a) 6V and (b) 6H as a function of wind speed and relative direction. (c) Relationship between 6V and 6H. (1/2)

(a) 6V versus RWD

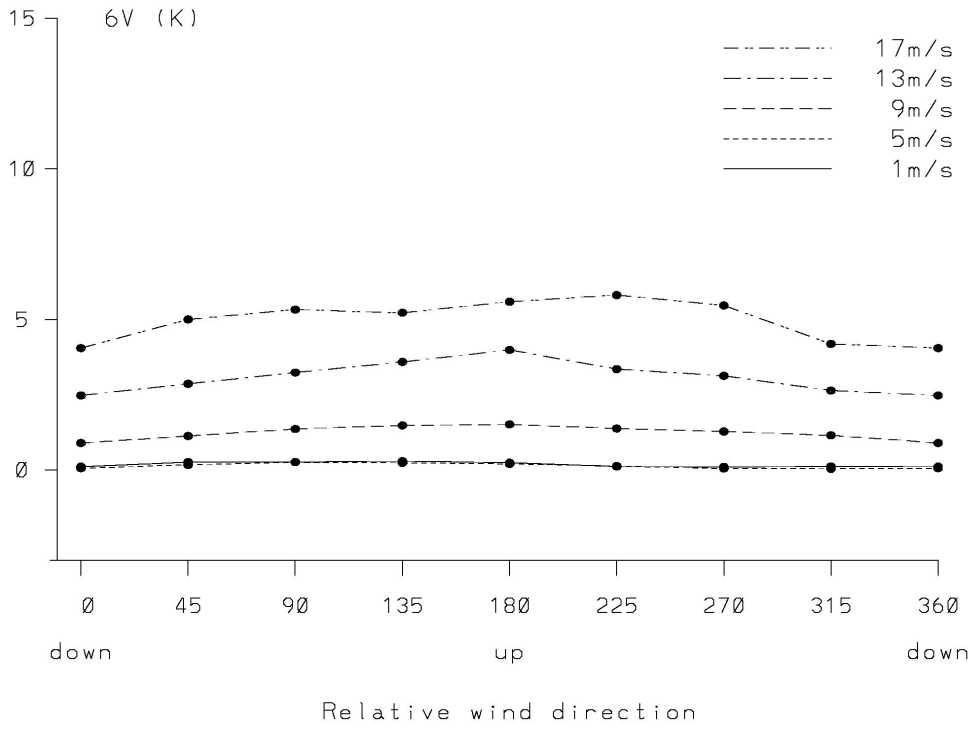

Fig. 2 Characteristics of (a) 6V and (b) 6H as a function of wind speed and relative direction
(c) Relationship between 6V and 6H. (2/2)

(b) 6H versus RWD

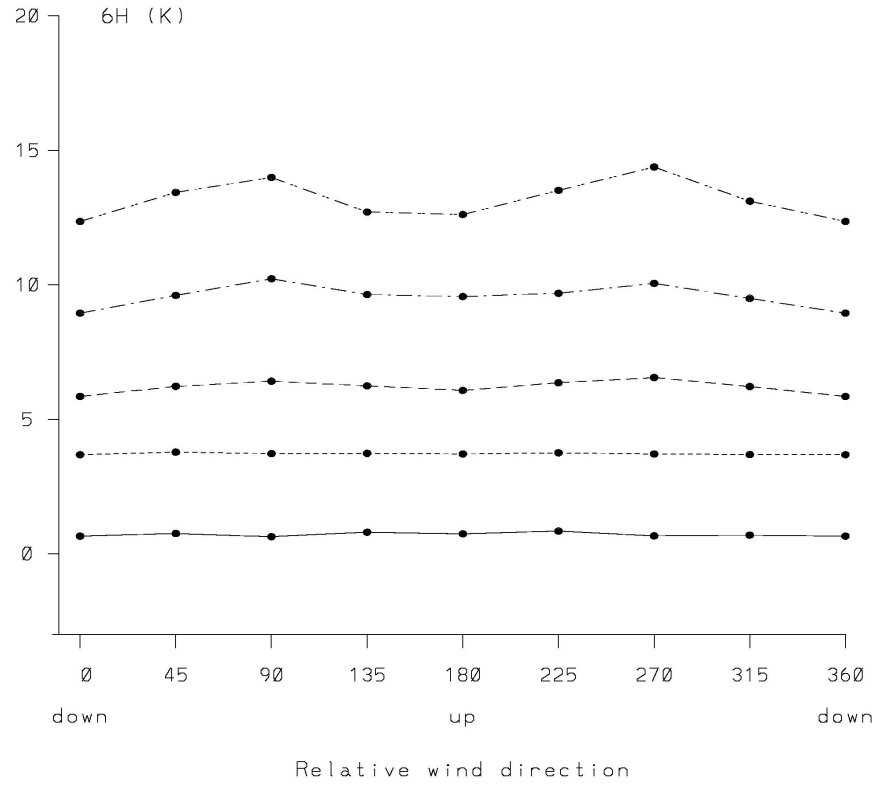

(c) 6V versus 6H

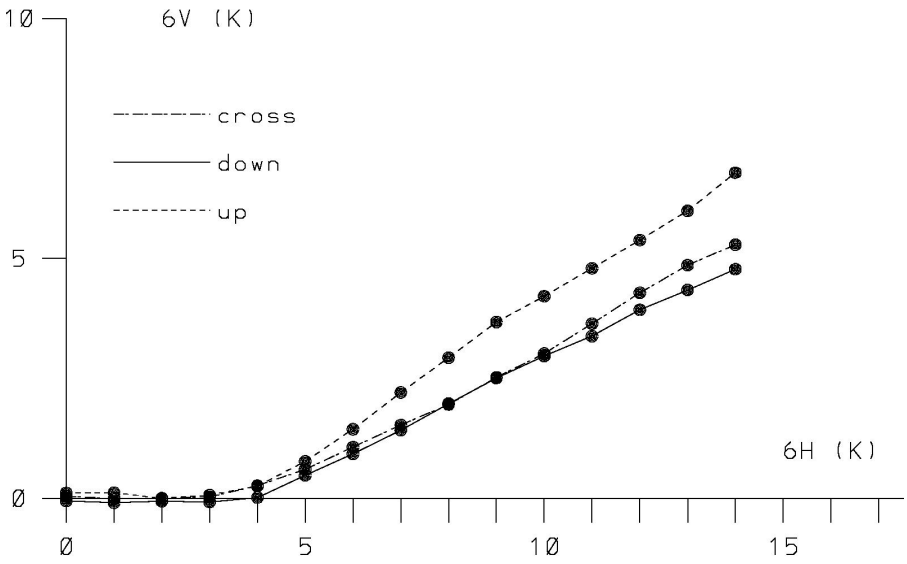

In Fig. 2 (a), it can be seen that 6V does not change with RWD for wind speeds of 1 and 5 m/s, but that it increases at higher wind speeds. 6V varies with RWD at wind speeds exceeding 9 m/s, reaching a maximum in the upwind direction and a minimum in the downwind direction. The difference between the maximum and minimum values is 1.5K at a wind speed of 13 m/s. In Fig. 2 (b), it can be seen that 6H increases even at small wind speeds, such as 1 m/s. 6H varies with the relative wind direction at wind speeds higher than 9 m/s, reaching a maximum in the crosswind direction and a minimum in the upwind and downwind directions.

In Fig. 2 (c), it can be seen that 6V does not change over a range where 6H is less than 3.8K = z0, and that both 6V and 6H increase above z0. The slope of 6V/6H (designated as sp) ranges from 0.5 to 0.7 (0.5 corresponds to the downwind direction; 0.7 corresponds to the upwind direction; values for the crosswind direction are intermediate). From Fig. 2 (c), we can calculate the extent of the wind effect on 6V (designated as inc_6V) as shown in Eq. (3).

$$\begin{aligned} \text{inc\_6V} &= 0 && \text{for 6H less than z0} \\ &= (6H - z0) \times sp && \text{for 6H greater than z0} \end{aligned} \qquad (3)$$

To avoid SST errors under very high wind speeds, we regard the SST as missing when 6H exceeds (z0 + 9).

Fig. 2 (c) is obtained from data for the global ocean. The relation between 6V and 6H depends on the air-sea temperature difference (ASD), in addition to the RWD. To observe the dependency on the ASD, we use air temperature data from the Global Analysis (GANAL) weather forecast model operated by the Japan Meteorological Agency. Fig. 3 shows the 6V-6H relation in the downwind direction and for three ASD cases (Shibata, 2007). The solid line corresponds to the global ocean case, the dotted line labeled by sp1 corresponds to the unstable case (i.e., ASD is –3°C), and the dotted line labeled by sp2 corresponds to the stable case (i.e., ASD is 2°C). The 6V-6H relation with the ASD in the crosswind direction is similar to the one in the downwind direction; however, the 6V-6H relation with the ASD in the upwind direction is different. The slope is almost the same for the three cases.

Fig. 3 Different slopes for different cases of ASD.

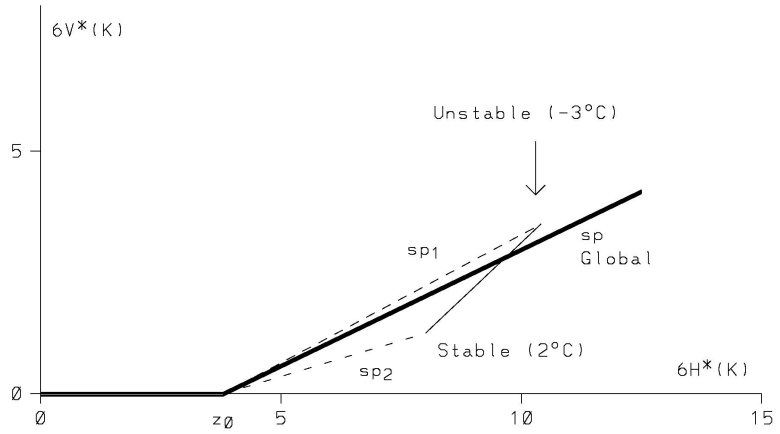

To determine sp, we must know the RWD. We can determine the RWD from the AMSR data. Fig. 4 shows the relation between 6H and S36. The parameter S36 represents the wind effect on the 36 GHz channel, and is described in detail in the SSW algorithm document.

Fig. 4 Method for Determination of RWD.

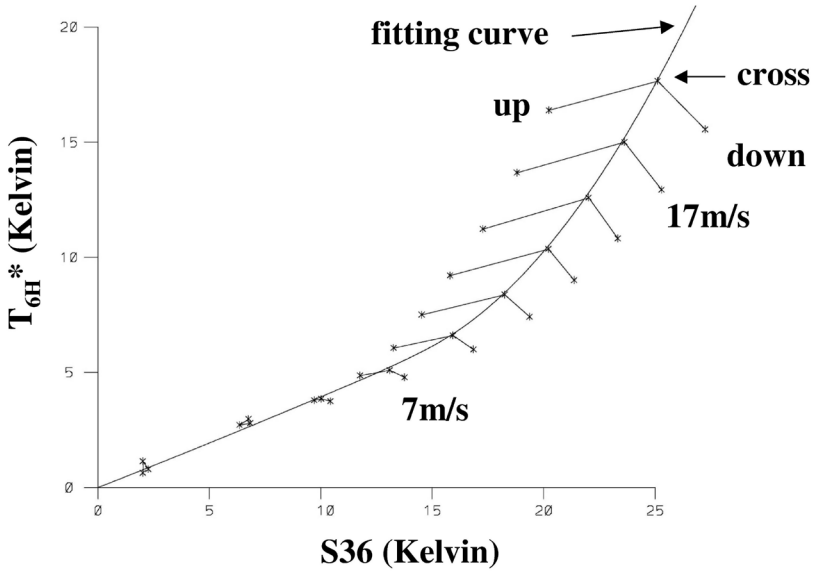

In Fig. 4, it is seen that the data points for upwind, downwind, and crosswind RWD become separated from one another for 6H above around 4 K. Below 4 K, the data points for the three directions overlap one another.

The results from Fig. 4 indicate that we can determine the RWD by combining 6H and S36, i.e., we measure the distance from a point of (6H, S36) to the fitting curve corresponding to the

crosswind direction, and normalize it to a value between −1 and 1 (designated as dd). A value of −1 corresponds to upwind, 0 to crosswind, and 1 to downwind. The coefficient sp ranges between 0.5 and 0.7. Thus, it can be expressed as shown in Eq. (4),

$$\begin{aligned} sp &= 0.57 - 0.13 \times dd \qquad -1 < dd \leqq 0 \quad \text{for upwind} \\ &= 0.57 - 0.07 \times dd \qquad 0 \leqq dd < 1.0 \text{ for downwind} \end{aligned} \tag{4}$$

Conversion to SST

At this point, we have already corrected 6V for atmospheric and wind effects. We now retrieve the SST from the corrected 6V by using the relation between 6V and SST. Fig. 5 shows this relation. The curves shown in Fig. 5 were obtained using the Fresnel formula, with an incidence angle of 55.0° and a salinity of 3.5%. The complex dielectric constant of the ocean water was obtained from Klein and Swift (1977). Since the complex dielectric constant seems not to be quite perfect, we made some small adjustments to the theoretical values for 6V. These adjustments became larger in cases with lower SST values (e.g., −0.5 K at SST = 0°C; 0.0 K at SST = 30°C).

In most cases, the AMSR SST is obtained from 6V. In rare cases, such as in areas where RFI is experienced at 6 GHz, the AMSR SST was obtained from the vertical polarization of the brightness temperature for the 10 GHz channel (10V). The 10V SST was retrieved only at 10°C and higher, because the sensitivity of 10V to SST is very weak below 10°C, as seen in Fig. 5. The atmospheric and wind-effect corrections for 10V are similar to those for 6V.

Fig. 5 Conversion to SST from 6V or 10V.

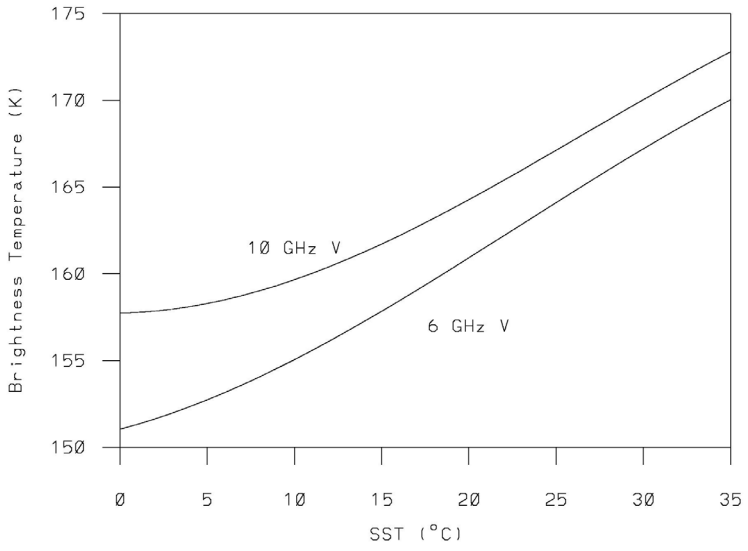

4. Algorithm Implementation

The AMSR3 SST algorithm is written with Fortran 77.

4.1. Implementation

compile the source code by f77, and run “a.out”

4.2. Input/output parameters

Input: L1B

MGDSST / JMA for the initial SST

GANAL / JMA for air temperature

Output: SST

Quality flags for missing SSTs:

128 — land; land and coastal areas are removed

129 — sea ice; sea ice areas are removed for the input SST less than 5°C

130 — sun glitter; sun glitter areas of relative angle 25° or less with the sun are removed

131 — rain; rainy areas defined by “atmos_effect_6V” greater than 6.6 K are removed

132 — strong wind; areas of wind speeds greater than around 15 m/s are removed

133 — abnormal SST; SST less than –2°C

160 — incidence angle; areas where the incidence angle deviates from 55° by 1° or more are removed

161 — RFI; RFI areas from global stars and ground based radars are removed

4.3. Ancillary data

land flag (own data)

climate salinity (own data)

scan bias for 6V and 6H (own data)

atmospheric correction table (own data)

monthly and SST dependency sp specification table (own data)

brightness temperature correction table during orbit, among months, among years, if necessary (own data)

average ASD table (own data)

4.4. Processing flow

run several subroutines sequentially

4.5. Example output

see the AMSR3 SST

4.6. Limitations

range –2 to 40°C

no data for strong wind speed

no data for strong rain rate

no data in areas of the shoreline

no data in areas of sea ice

no data inside sun glitter areas

no data within RFI areas

ground based radar

global stars

5. Validation Concept

We will compare the AMSR3 SST retrievals with buoy SST measurements observed for the global ocean. Buoy data are collected through the Global Telecommunications System (GTS) and include data from both moored and drifting buoys. The number of matched observations is roughly 800 per day.

In order to compare the SSTs from AMSR3 and buoys, we will average the AMSR3 SST within each 3 × 3 pixel area. We omit cases in which the difference between the maximum and minimum AMSR3 SST is larger than 3°C within the 3 × 3 pixel area. We also omit cases where the absolute difference between the AMSR3 and buoy SST is larger than 3°C.

We will check for cross-talk of the SST retrievals with four parameters: accumulated water vapor content (WV), accumulated cloud liquid water content (CLW), sea surface wind speed, and RWD.

References

Hollinger J. P. and Lo R. C., 1984: Determination of sea surface temperature with N-ROSS. Naval Research Laboratory Memorandum Report 5375.

Milman A. S. and Wilheit T. T., 1985: Sea surface temperature from the Scanning Multichannel Microwave Radiometer on Nimbus 7. J.G.R., 90 (C6): 11631-11641.

Klein L. A. and Swift C. T., 1977: An improved model for the dielectric constant of sea water at microwave frequencies. IEEE Trans. Antennas and Propagation, 25: 104-111.

Shibata A., 1994: Determination of water vapor and liquid water content by an iterative method. Meteorol. Atmos. Phys., 54: 173-181.

Shibata A., Imaoka K., Kachi M., and Murakami H., 1999: SST observation by TRMM Microwave Imager aboard Tropical Rainfall Measuring Mission. Umi no Kenkyu, 8: 135-139 (in Japanese).

Shibata A., 2003: A change of microwave radiation from the ocean surface induced by air-sea temperature difference, Radio Science, 38 (4): 8063-8072.

Shibata A., 2004: AMSR/AMSR-E SST algorithm developments: removal of ocean wind effect, Italian J. Remote Sensing, 30/31: 131-142.

Shibata, A., 2006: Features of ocean microwave emission changed by wind at 6 GHz, J. Oceanogr., 62(3), 321-330.

Shibata, A., 2007: Effect of air-sea temperature difference on ocean microwave brightness temperature estimated from AMSR, SeaWinds, and buoys, J. Oceanogr., 63(5), 863-872.

Chapter 6.

Description of GOSAT-GW AMSR3 Sea Surface Wind Speed Algorithm

Akira Shibata

Remote Sensing Technology Center of Japan

Table of Contents

1. Introduction 6-3
2. Algorithm Overview 6-3
3. Theoretical Description 6-4
4. Algorithm Implementation 6-8
   4.1 Implementation 6-8
   4.2 Input/output parameters 6-8
   4.3 Ancillary data 6-9
   4.4 Processing flow 6-9
   4.5 Example output 6-9
   4.6 Limitations 6-9
5. Validation Concept 6-9

References

1. Introduction

There are two types of algorithm used for retrieving sea surface wind speed (SSW) from passive microwave radiometers. One uses a higher frequency, such as 36 GHz, and the other uses lower frequencies, such as 6 and 10 GHz. Although the first method has a better retrieval accuracy than the second method, it suffers significant contamination from raindrops. Consequently, the SSW retrieved by the first method is absent for rainy areas. An algorithm for the first method for the Advanced Microwave Scanning Radiometer (AMSR) is described in Shibata (2012), and for the second method in Shibata (2006). In developing the first type of algorithm, we used a combination of data from AMSR and SeaWinds, both onboard the ADEOS-II. Here we present an AMSR3 onboard the GOSAT-GW algorithm using the same method of higher frequencies of AMSR2 onboard the GCOM-W satellite.

2. Algorithm Overview

To develop the SSW algorithm, we need to know how the characteristics of brightness temperature (Tb) vary with sea surface wind speed. Although it is more desirable to know this for a frequency of 36 GHz, it is difficult to determine the variation for such a high frequency, owing to the increased contamination by atmospheric effects. Therefore, we determine it at 6 GHz. As shown in Fig. 2 in the sea surface temperature (SST) algorithm description, the increment in Tb with vertical polarization is at 6 GHz (6V) because the wind speed is zero under weak wind conditions ($\leq$ 6 m/s) and increases gradually above this speed. The Tb with horizontal polarization at 6 GHz (6H) increases even under weak wind conditions, and its increment is larger than that of 6V for all wind speeds. An anisotropic feature depending on the relative wind direction (RWD), the angle made by the direction of AMSR viewing and the wind direction, is found for both polarizations. 6V reaches a maximum in the upwind direction and a minimum in the downwind direction; 6H reaches a maximum in the crosswind direction and a minimum in both the up and downwind directions. We assume that Tb maintains similar characteristics at 36 GHz. Firstly, we will calculate a parameter, S36, from the 36 GHz data. Then, we will correct the anisotropic feature of S36, and finally, we will convert S36 to SSW.

3. Theoretical Description

Calculation of S36

Tb at 36 GHz was computed at the satellite height using a microwave transfer model that has been described in detail (Shibata, 1994; Shibata, 2004). The atmospheric part of this model deals only with absorption processes by water vapor, oxygen, and cloud liquid water, and does not deal with scattering by raindrops. The reflection from a calm ocean surface is described by the Fresnel formula, for which the complex dielectric constant of ocean water is obtained from Klein and Swift (1977). The model uses the daily aerological data of about sixteen Japanese observation sites in one year for intervening atmospheric parameters. Figure 1 reports the calculated Tb with vertical polarization at 36 GHz (36V; ordinate) versus Tb with horizontal polarization at 36 GHz (36H; abscissa), both in units of Kelvin. The dots represent averaged values of 36H corresponding to 36V, with a 1 K interval. In these calculations, the total amount of water vapor varies from 5 to 60 kg/m^2, and the liquid water content takes two values of 0 and 0.4 kg/m^2. The line OA is a regression line of these data. The line OA represents the calm ocean surface condition, while the line WA represents the ocean surface roughened by wind, for which the emissivity of the vertical polarization increases by 0.01 and that of the horizontal polarization increases by 0.1. The two lines OA and WA intersect at the point A. For other changes in surface emissivity, the regression lines also intersect at the point A. Tb at the point A is about 300 K for both polarizations, which may represent the intervening atmospheric temperature in a lower level. Under an infinite nonopaque condition, Tb may approach the atmospheric temperature in the lower level, regardless of the ocean surface condition.

Fig. 1 Definition of S36.

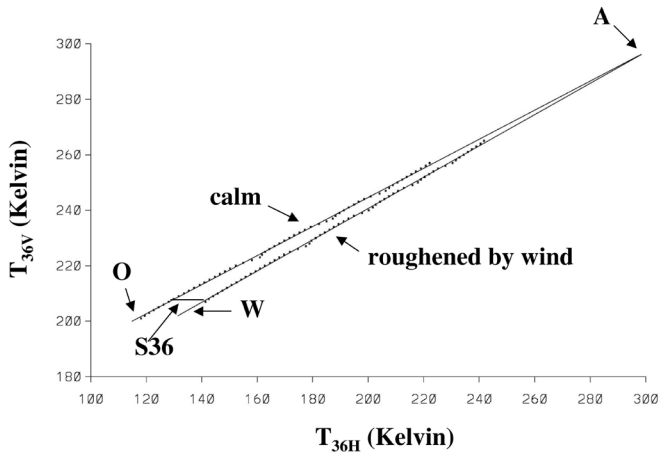

A parameter representing ocean wind is defined by a horizontal length between OA and WA, as shown by S36 in Figure 1, and written as in eq. (1).

$$S36 = (36H - a \times (36V - b) - c) / f + t \quad (1)$$

$$b = 208$$

$$f = 1 - 0.01 \times (36V - 200) \quad (2)$$

The coefficient b is a constant, whereas a and c depend on SST. In eq. (1), f is an atmospheric correction and represents the convergence of the two lines OA and WA. The difference in Tb for 36V between O and A is about 100 K, and f diminishes when 36V approaches 300 K in eq. (2). In eq. (1), t is an offset that will be explained later. The position of point O shifts in accordance with changing SST, and the values of a and c depend on SST. The values of a and c can be determined by comparing S36 with the SeaWinds wind speed. Ideally, these values should be determined against a SeaWinds wind speed of 0 m/s, in which case t = 0. However, such a case is very rare, and there are insufficient collocated data points for comparison. Therefore, collocated data are obtained at a SeaWinds wind speed of 5 m/s (i.e., in a range from 4.5 to 5.5 m/s), and t is set empirically as 4.5. Table 1 lists values of a and c for seven SSTs from 0 to 30ºC with 5ºC intervals. The technique employed in eq. (1) can be applied also to the other frequencies of 18, 23, and 89 GHz, although their SST dependencies are not listed. Hereafter, the corresponding parameters for these frequencies are called S18, S23, and S89, respectively.

Table 1 Values of a and c against seven SSTs.

SST [ºC]	a	c
0	2.23	132.0
5	2.20	132.2
10	2.14	131.5
15	2.07	130.7
20	2.06	128.8
25	2.03	127.4
30	2.06	124.2

Correction of the anisotropic feature of S36

S36 and the corresponding parameters for the other frequencies also have anisotropic features depending on RWD, whose dependencies can be determined by comparing the parameters with the SeaWinds wind speed and direction. In Figure 2, S89, S36, S23, and S18 are shown against RWD and for ten cases of SeaWinds wind speed from 1 to 19 m/s with 2 m/s intervals. It is clear that the sensitivity to wind speed becomes greater with increasing frequency, i.e., highest for S89, medium

for S36, and lowest for S23 and S18. However, the behavior of S89 seems to be noisier than for the other frequencies, which may be attributable to atmospheric contamination at higher frequencies. Therefore, S36 is the best parameter for retrieving wind speed. S36 is almost constant with RWD for weak wind speeds of less than 5–7 m/s. For wind speeds over this value, S36 has an anisotropic feature, reaching a minimum in the upwind direction and a maximum in the downwind direction. As mentioned above, 6V reaches a maximum in the upwind direction and a minimum in the downwind direction. Assuming that this feature of 6V holds similarly for 36V, S36 reaches a minimum in the upwind direction, because a × 36V is dominant in eq.(1) (a is almost equal to 2). As for the maximum value, S36 reaches a maximum in the downwind direction, and S18 reaches its maximum for directions between cross and downwind directions (S23 has characteristics between those of S36 and S18).

Fig. 2 S89, S36, S23, and S18 against RWD and for ten cases of SeaWinds wind speed.

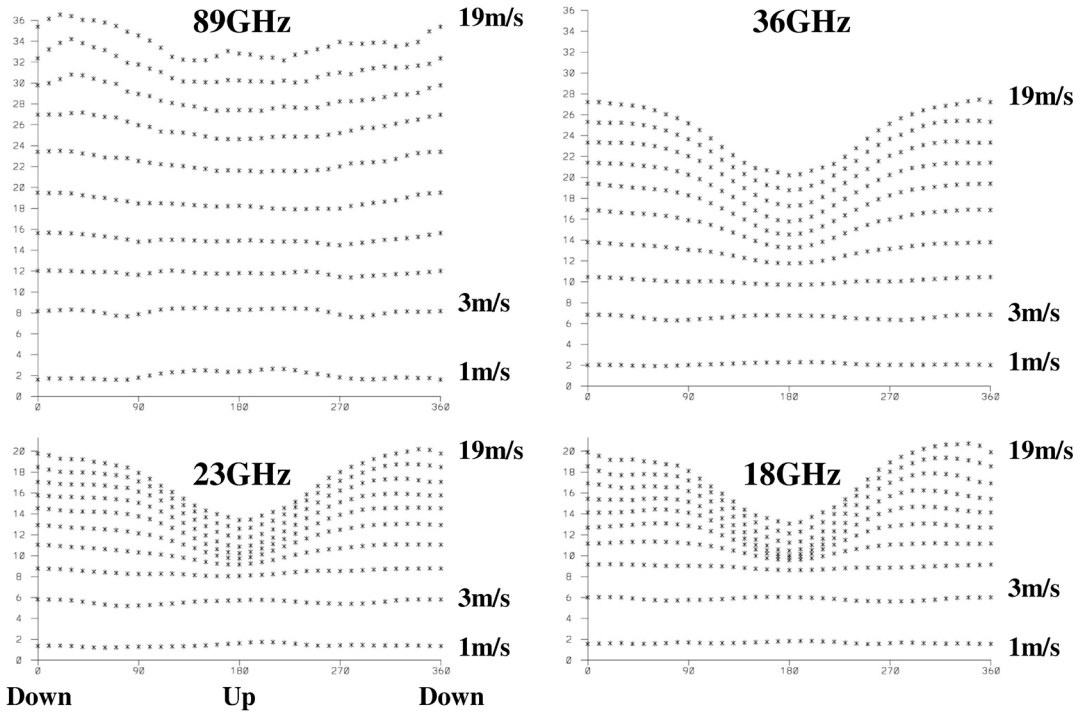

The anisotropic feature of S36 should be corrected before converting S36 to wind speed, because otherwise the converted wind speed will inherit the anisotropic feature. Figure 3 depicts the relation between S36 and 6H for three cases of RWDs (up, cross, and downwind) and ten cases of wind speeds (from 1 to 19 m/s with 2 m/s intervals). 6H is defined by eq. (2) in the SST algorithm description. As mentioned previously, S36 reaches a maximum in the downwind direction and a

minimum in the upwind direction. Also, 6H reaches a maximum in the crosswind direction and a minimum in the up and downwind directions. The anisotropic correction means that S36 for both the up and downwind directions is adjusted to S36 for the crosswind direction, following the slopes in Figure 3. A fitting curve corresponding to crosswind is shown in Figure 3. Different slopes are used for the adjustments from up to crosswind and from down to crosswind directions, respectively. Figure 4 depicts S36 before and after the anisotropic correction. For almost the entire range of SeaWinds wind speed, S36 remains constant with RWD. However, at larger wind speeds, such as 19 m/s, S36 varies slightly with RWD, with variations on the order of 1 K.

Fig. 3 Method of correcting the anisotropic feature of S36.

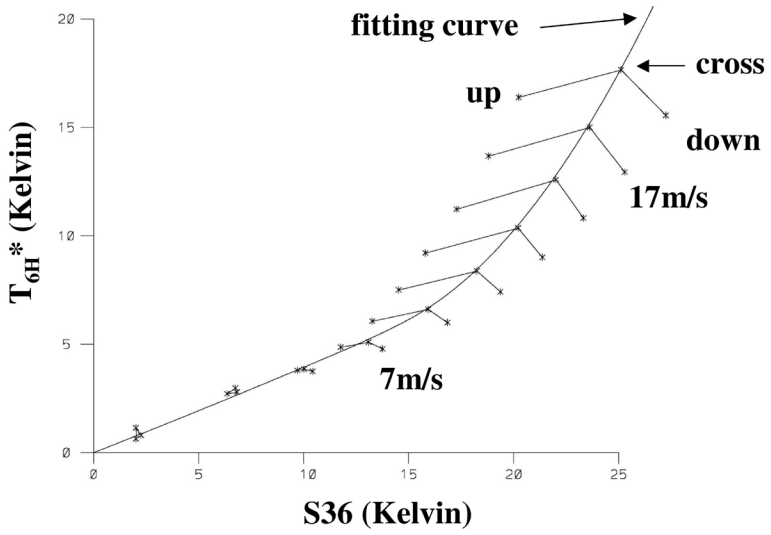

Fig. 4 Comparison of S36 before and after anisotropic correction.

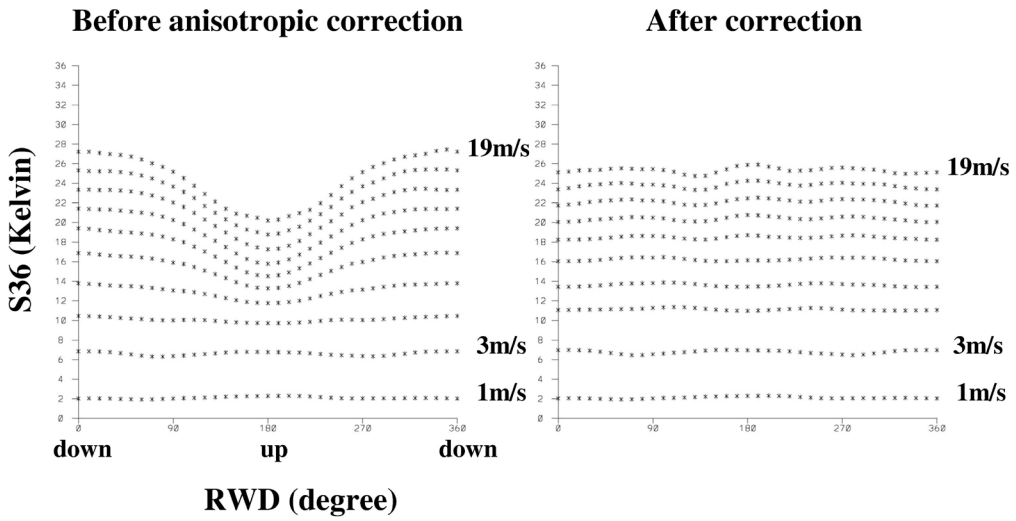

Conversion of S36 to wind speed

Finally, S36 is converted to wind speed, using the curve shown in Figure 5, which was obtained by comparing S36 with the SeaWinds wind speed for about 3 × 108 collocated data points over a period of seven months. Conversion of negative S36 values is considered, as S36 sometimes becomes negative. Reasons for S36 to become negative are (a) Tb noise (fluctuation) of the AMSR and (b) incorrect SST derived from the weekly SST. The remaining error in the corrected S36 (Fig. 4) gives rise to a wind speed error. From the conversion curve, an error of 1 K in S36 is estimated as an error of 1 m/s in wind speed in the 15–20 m/s range.

Fig. 5 Conversion curve from S36 to wind speed.

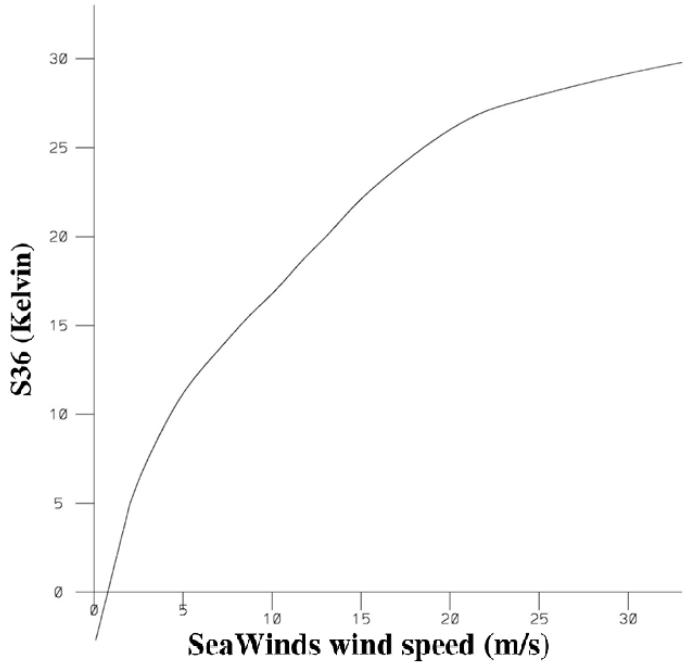

4. Algorithm Implementation

The AMSR3 SSW algorithm is written in Fortran 77.

4.1. Implementation

compile the source code with f77, and run “a.out”

4.2. Input/output parameters

Input: L1B

MGDSST / JMA for the initial SST

GANAL / JMA for air temperature

Output: SSW

Quality flags for missing SSW:

128 — land; land and coastal areas are removed

129 — sea ice; sea ice areas are removed for input SST less than 5℃

130 — sun glitter; sun glitter areas of relative angle 25° or less with the sun are removed

131 — rain; rainy areas defined by “atmos_effect_6V” greater than 6.6 K are removed

132 — abnormal wind; out of range from 0 to 30 m/s

133 — abnormal wind; impossible to determine the relative wind direction

134 — No MGDSST

160 — incidence angle; areas where the incidence angle deviates by 1° or more from 55° are removed

161 — RFI; RFI areas from global stars and ground based radars are removed

4.3. Ancillary data

land flag (own data)

S36 specification table (own data)

conversion table (own data)

Tb correction table during orbit, among months, among years, if necessary (own data)

4.4. Processing flow

run several subroutines sequentially

4.5. Example output

see the AMSR3 SSW

4.6. Limitations

range of 0 to 30 m/s

no data for rain

no data for shorelines

no data for sea ice areas

no data inside sun glitter areas

5. Validation Concept

We will validate the AMSR3 SSW by comparison with SSW values from ocean buoys. Ocean buoy data are collected from moored buoys of the National Data Buoy Center (NDBC), the Tropical Atmosphere Ocean (TAO) Project, and the Prediction and Research Moored Array in the Atlantic (PIRATA) in open ocean 100 km off shorelines. The height at which the wind speed is measured differs among buoys, so it is adjusted to 10 m for all buoys by assuming a neutral atmospheric condition. In combining the AMSR3 and buoy data, the time difference between the AMSR2 and buoy measurements is limited to within one hour. Nine pixels of AMSR3 data are averaged around the buoy location.

References

Klein L. A. and Swift C. T., 1977: An improved model for the dielectric constant of sea water at microwave frequencies. IEEE Trans. Antennas and Propagation, 25: 104-111.

Shibata A., 1994: Determination of water vapor and liquid water content by an iterative method. Meteorol. Atmos. Phys., 54: 173-181.

Shibata A., 2004: AMSR/AMSR-E SST algorithm developments: removal of ocean wind effect. Italian J. Remote Sensing, 30/31: 131-142.

Shibata, A., 2006: A wind speed retrieval algorithm by combining 6 and 10 GHz data from Advanced Microwave Scanning Radiometer: wind speed inside hurricanes. J. Oceanogr., 52(3), pp.351-359.

Shibata, A., 2012: Ocean wind speed retrieval algorithm using the frequency 36 GHz vertical/horizontal and 6 GHz horizontal data of the Advanced Microwave Scanning Radiometer (AMSR). Italian J. Remote Sensing, 45: 133-140.

Chapter 7.

Description of GOSAT-GW AMSR3 All-weather Sea Surface Wind Speed Algorithm

Akira Shibata, Mieko Seki

Remote Sensing Technology Center of Japan

Table of Contents

1. Introduction 7-3
2. Algorithm Overview 7-3
3. Theoretical Description 7-4
4. Algorithm Implementation 7-8
   4.1 Implementation 7-8
   4.2 Input/output parameters 7-8
   4.3 Ancillary data 7-9
   4.4 Processing flow 7-9
   4.5 Example output 7-9
   4.6 Limitations 7-9
5. Validation Concept 7-9

References

1. Introduction

In constructing algorithms to retrieve ocean wind speed from satellite-borne passive microwave radiometers, it is common to use higher frequencies such as 36 GHz rather than lower frequencies for retrieval of low to moderate winds up to 25 m/s in no-rain areas, since the sensitivity to ocean wind at higher frequencies is better than that at lower frequencies (Wentz, 1983). However, the atmospheric opacity at higher frequencies exceeds that at lower frequencies. The brightness temperature (Tb) at 36 GHz becomes saturated inside rainstorms such as hurricanes and typhoons, and sometimes decays. In other words, Tb at 36 GHz does not contain information about the ocean surface inside rainstorms. Therefore, it is necessary to develop algorithms that use lower frequencies, even if they do have lower sensitivity to ocean wind. An algorithm for using the higher frequencies method for the Advanced Microwave Scanning Radiometer (AMSR) is described in Shibata (2012), and for the lower frequencies method in Shibata (2006). The development of the algorithm for lower frequencies involved the integration of data from AMSR and SeaWinds, both of which are onboard the ADEOS-II satellite. An all-weather sea surface wind speed (ASW) algorithm for AMSR3 onboard GOSAT-GW was described, employing the method of utilizing lower frequencies from AMSR instruments, including AMSR, AMSR-E, and AMSR2.

2. Algorithm Overview

ASW retrieval algorithm was developed using 6 and 10 GHz h-pol (6H and 10H) data from the Advanced Microwave Scanning Radiometer (AMSR) onboard the Advanced Earth Observation Satellite-II (ADEOS-II), AMSR-E onboard AQUA, AMSR2 onboard GCOM-W, and AMSR3 onboard GOSAT-GW to retrieve wind speed inside rainstorms, primarily hurricanes and typhoons. The h-pol was used rather than the v-pol because the brightness temperature sensitivity to the ocean wind at h-pol is larger than that at v-pol. The microwave emission change of 6H and 10H corresponding to ocean wind was evaluated in no-rain areas by combining AMSR and SeaWinds data aboard the ADEOS-II (SeaWinds was NASA's scatterometer), and it was found that the ratio of the two 6H to 10H increments due to ocean wind was 0.9. Assuming that this result also holds for higher wind speeds and under rainy conditions, the brightness temperatures at 6H and 10H were simulated using a microwave radiative transfer model. A parameter W6 (unit: Kelvin) was then defined, representing an increment at 6H due to ocean wind. W6 is relevant for regions experiencing rainfall and is applicable across all ranges of sea surface temperature. W6 was compared with wind speed reported by the National Hurricanes Center for several hurricanes in the Western Atlantic Ocean over three years (2002 to 2004). W6 averaged around centers of hurricanes was found to

exhibit a sensitivity to wind speed, such as increasing from 22 K to 65 K as the wind speed rose from 65 to 140 knots (33 to 72m/s), and an empirical relationship relating the averaged W6 to wind speed in hurricanes was derived.

3. Theoretical Description

Ocean Microwave Emissions at 6H and 10H

H-pol was used to retrieve ASW rather than v-pol, because the sensitivity to the ocean wind at h-pol is larger than v-pol (Shibata, 2003). We define two similar parameters: the first one is the difference between the AMSR 6(10)H and calm ocean emission, corrected for the atmospheric effects, which is defined by Eq. (1), and the other is the difference between the AMSR 6(10)H and calm ocean emission. The former parameter is used to quantify the wind speed dependence at 6H and 10H, and the latter is used to develop the wind speed algorithm under degraded conditions where data are not corrected for atmospheric effects. The former parameters 6(10)H* are defined by Eq. (1), and represent the quantity of ocean microwave emission changed by ocean wind at 6(10)H.

$$6(10)H^* = AMSR\_6(10)H - atmos\_effect\_6(10)H - calm\_ocean\_6(10)H \quad (1)$$
$$calm\_ocean\_6(10)H = SST \times (1 - r)$$

where AMSR_6(10)H is Tb of AMSRs at 6(10) GHz h pol, atmos_effect_6(10)H is the atmospheric correction at 6(10) GHz h-pol, and calm_ocean_6(10)H is the ocean microwave emission at 6(10) GHz h-pol under calm ocean conditions. The atmospheric correction was calculated by using data from 23V and 36V (Shibata, 2004). The 23 GHz frequency was used to eliminate the effect of water vapor, and 36 GHz to eliminate the effect of cloud liquid water. In these calculations, we excluded rainy areas by specifying a maximum limit of atmos effect_6H. The coefficient of r in calm_ocean_6(10)H is the reflection coefficient given by the Fresnel formula with an incidence angle of 55.0 degrees and a salinity of 35 PSU. The complex dielectric constant of the ocean water was obtained from Klein and Swift (1977). The reflection coefficient is a function of frequency, polarization, incidence angle, SST, and salinity. We used SST from the Reynolds weekly analysis (Reynolds and Smith, 1994). The weekly SST was interpolated on a corresponding day, and also interpolated spatially into a corresponding point. As for the salinity effect, the sensitivity at 6H is 0.003 K/PSU at 0°C SST, and –0.039 K/PSU at 30°C SST, when the salinity changes from 30 to 35 PSU. The salinity effect at 10H is 0.006 K/PSU and –0.012 K/PSU, respectively. Therefore, the salinity effect is negligible in our study.

Calculation of W6

First, we simulated Tbs under calm ocean surface conditions. The microwave radiative transfer model was obtained from (Shibata 1994, 2004). The Tbs of group A in Fig. 1(a) are the results of the 15°C SST. The Tbs increased from O to P owing to the increase in water vapor and liquid water. We observe that Tbs lie on a single line from O to P, and the two effects due to water vapor and liquid water are almost the same. The Tb increment due to water vapor was small (e.g., 9 K for 10H and much smaller for 6H). Therefore, the Tb increment depicted in Fig. 1(a) was mainly due to liquid water. Second, group B in Fig. 1(a) was obtained by assuming a roughened ocean condition, that is, increasing the emissivity of the ocean surface by 0.2 for 10H and 0.18 for 6H. We assumed that the ratio of 6H to 10H was 0.9 for higher wind speeds and under rainy conditions. The value of 0.18 for 6H was chosen arbitrarily, and it corresponds to a Tb increment of 52 K for 6H. This Tb increment was related to the NHC wind speed. Point O under calm conditions shifts to Q under roughened conditions at the lowest atmospheric opacity. Point P shifts to R at a higher atmospheric opacity. The slope of line PR is larger than that of OQ because of the different atmospheric opacities between 6H and 10H. In Fig. 1(a), the Tb of 6H increases with the length of OQ* at the lowest atmospheric opacity. It increases with the length of PR* at higher atmospheric opacities. These Tb increments represent the ocean wind effect. The lengths of OQ* and PR* are different owing to the different atmospheric effects (mainly due to rain) on 6H. In Fig. 1(a), we set the SST to 15°C. For the other SSTs, lines A and B were shifted in parallel. We can eliminate the dependence of Tb on SST by subtracting the calm ocean emission, and we define a parameter $6(10)H^-$ using Eq. (2).

$$6(10)H^- = \text{AMSR\_6(10)H} - \text{calm\_ocean\_6(10)H}, \quad (2)$$

where AMSR_6(10)H and calm_ocean_6(10)H are the same as in Eq. (1).

In Fig. 1(a), the relations between 6H and 10H are slightly nonlinear; however, we have approximated them as linear for simplicity. Using $6(10)H^-$, we obtained Fig. 1(b), in which line A is approximated as a linear line passing through point O(a, b) with slope c. Now, we have the AMSR observation of ($10H^-$, $6H^-$) at an arbitrary point on line B in Fig. 1(a), and we set it at point F in Fig. 1(b). Then, we obtain an intersecting point E ($10H^-_E$, $6H^-_E$) made by two lines, OP and EF. The slope of line EF is denoted as sl. Finally, we define W6 (unit: Kelvin) as the length of EF* divided by the atmospheric effect (=fac).

$$W6 = EF^*/fac = (6H^- - 6H^-_E)/fac$$

$$= (6H^- - c \times 10H^- + a \times c - b) \times sl/(sl - c)/fac, \quad (3)$$

where a = 15, b = 10.5, c = 0.46

$$sl = 0.90 + 0.40 \times (10H^-_E - a)/80., \quad (4)$$

$$fac = 1 - 0.20 \times (10H^-_E - a)/80. \quad (5)$$

Constants a, b, and c in Eq. (3) are the parameters that define line OP. Equation (4) provides the slope of line EF. The minimum value of sl is 0.9, corresponding to the lowest atmospheric opacity, and it increases as the length of OE* (= $10H^{-}_{E}$ – a) increases. The constant values of 0.4 and 80 in Eq. (4) are determined as shown in Fig. 1(a). The atmospheric effect given by Eq. (5) is the ratio of the two lengths, PR*/ OQ*, as shown in Fig. 1(a). The constant values of 0.2 and 80 in Eq. (5) are determined in Fig. 1(a). Determining the values of sl and fac requires ascertaining the length of the OE*. There may be several methods for determining $10H^{-}_{E}$ of point E*. In this study, we employed an iterative approach to address this issue. Initially, the first $10H^{-}_{(1)}$ was calculated using the observed $10H^{-}$. Subsequently, the second $10H^{-}_{(2)}$ was determined based on the first $10H^{-}_{(1)}$ value. The convergence to E* is fast, such as n = 4 for the absolute difference of ($10H^{-}_{(n)}$ – $10H^{-}_{(n-1)}$) to become less than 0.1 K. The difference in W6, whether lines A and B are treated as linear or nonlinear, is less than 1 K when the length of OE* is 80 K.

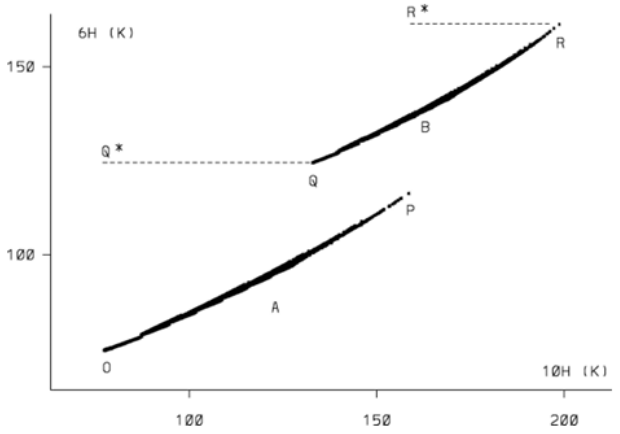

(a)

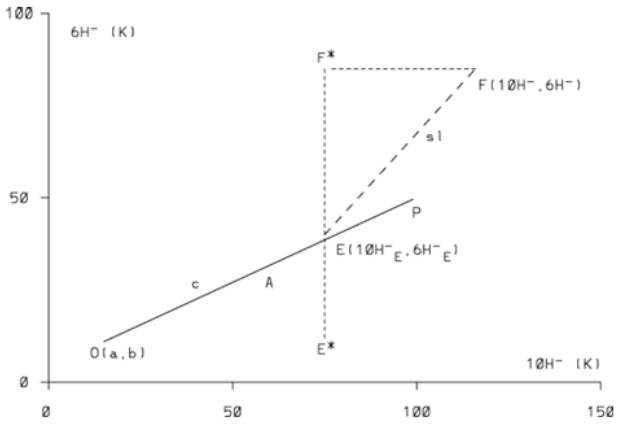

(b)

Fig. 1. (a) Simulations of Tbs of 6H and 10H, group A for calm condition, and group B for roughened condition. (b) Thematic figure drawn from (a). (refer to Ref. shibata (2006))

Conversion of W6 to wind speed

We calculated W6 by Eq. (3). As the hurricane strength, we define Eq. (6), where W6 is averaged for pixels according to the W6 value from the maximum to the minimum until the average number reaches n. W6_ave is a parameter that depends on the average area size. Here, we set n = 100, corresponding roughly to an area of 100 × 100 km^2, because AMSRs spatial sampling is at 10 km intervals. Fig. 2 illustrates the relationship between W6_ave (n = 100) and the NHC wind speed calculated from all cases. Fig. 2 demonstrates that W6_ave increased from 22 K to 65 K as the wind speed escalated from 65 to 140 knots. We see that the relation between W6_ave and wind speed is nonlinear in the range of 65–140 knots. We express this relation as two linear branches, shown by the dotted line in Fig. 2, and numerically by Eq. (7) and (8), respectively. Equations (7) and (8) are applicable to hurricanes and typhoons, particularly for very high wind speeds. Fig. 2 illustrates the relationship between W6 and SeaWinds wind speed. The scales at which W6_ave and W6 are plotted are identical. The SeaWinds wind speed (m/s) was converted to knots and multiplied by 1.12 (SeaWinds wind speed is a 10-minute average). W6 (refer to Eq.(3)) and 6H* (refer to Eq.(1)) correspond one-to-one (Shibata 2006), and by connecting the two curves in Fig. 2, it becomes possible to calculate wind speed from low to high speeds regardless of rainfall.

$$W6\_ave=(W6(1)+W6(2)+\ \ldots\ldots\ldots+W6(n))\ /\ n \qquad (n=1,\ldots..100\ (\ max\ ->\ )\ ) \tag{6}$$

$$\begin{aligned} &\text{Wind\_speed (knots)} \\ &= 2.86 \times W6\_ave && \text{if} \quad W6\_ave < 38.5K \\ &= 1.14 \times (W6\_ave - 38.5) + 110.1 && \text{if} \quad W6\_ave > 38.5K \end{aligned} \tag{7}$$

$$\begin{aligned} &\text{Wind\_speed(m/s)} \\ &= 1.47 \times W6\_ave && \text{if} \quad W6\_ave < 38.5K \\ &= 0.59 \times (W6\_ave - 38.5) + 56.7 && \text{if} \quad W6\_ave > 38.5K \end{aligned} \tag{8}$$

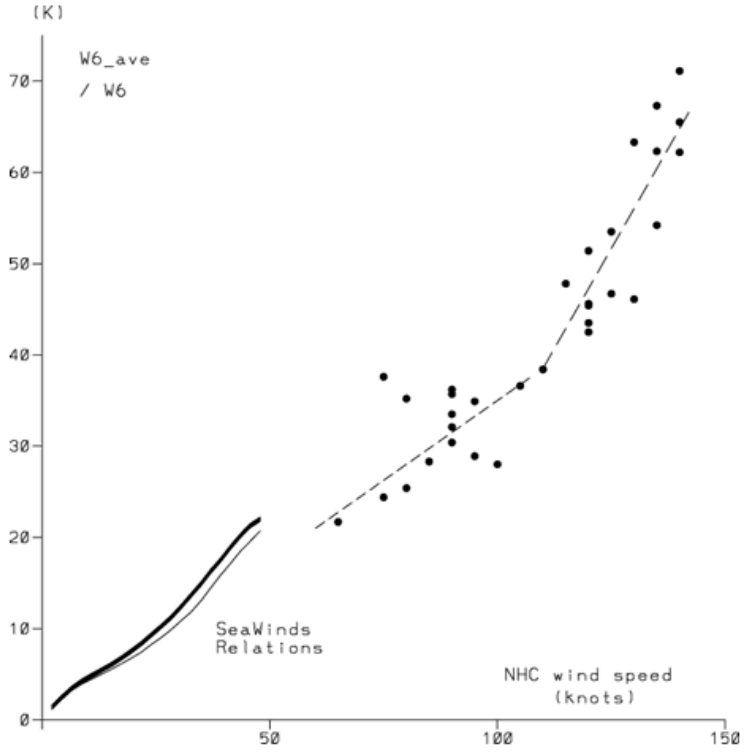

Fig. 2 Relation between W6_ave and NHC wind speed made from all cases.
(refer to Ref. shibata (2006))

4. Algorithm Implementation

The AMSR3 ASW algorithm is written in Fortran 77.

4.1. Implementation

compile the source code with f77, and run “a.out”

4.2. Input/output parameters

Input: L1B and L1R

MGDSST / JMA for the initial SST

GANAL / JMA for air temperature

Output: ASW

Quality flags for missing ASW:

128 — land; land and coastal areas are removed

129 — sea ice; sea ice areas are removed for input SST less than 5℃

130 — sun glitter; sun glitter areas of relative angle 25° or less with the sun are removed

134 — No MGDSST

161 — abnormal L1 or RFI

4.3. Ancillary data

land flag (own data)

W6 specification table (own data)

conversion table (own data)

Tb correction table during orbit, among months, among years, if necessary (own data)

4.4. Processing flow

run several subroutines sequentially

4.5. Example output

see the AMSR3 ASW

4.6. Limitations

range of 0 to 70 m/s

no data for shorelines

no data for sea ice areas

no data inside sun glitter areas

5. Validation Concept

The ASW was validated using wind speed values from the dropsonde. Dropsondes were collected from the National Hurricane Center (NHC) of the National Oceanic and Atmospheric Administration (NOAA) within 6 hours and 500 km from the best track data, which were provided by the International Best Track Archive for Climate Stewardship (IBTrACS) project. The ASW was not validated in the area where the EYE and EYEWALL were present and precipitation was greater than 30 mm/h. When combining the AMSR and dropsonde data, the time difference between the AMSR and dropsonde was limited to within one and half hours and 10 km. The distance between the dropsonde and best track was over 50 km.

References

Klein L. A. and Swift C. T., 1977: An improved model for the dielectric constant of sea water at microwave frequencies. IEEE Trans. Antennas and Propagation, 25: 104-111.

Reynolds, R. W. and T. M. Smith (1994): Improved global sea surface temperature analyses. J. Climate, 7, 929–948.

Shibata A., 1994: Determination of water vapor and liquid water content by an iterative method. Meteorol. Atmos. Phys., 54: 173-181.

Shibata, A. (2003): A change of microwave radiation from the ocean surface induced by air-sea temperature difference. Radio Science, 38(4), 8063–8072.

Shibata A., 2004: AMSR/AMSR-E SST algorithm developments: removal of ocean wind effect.

Italian J. Remote Sensing, 30/31: 131-142.

Shibata, A., 2006: A wind speed retrieval algorithm by combining 6 and 10 GHz data from Advanced Microwave Scanning Radiometer: wind speed inside hurricanes. J. Oceanogr., 52(3), pp.351-359.

Shibata, A., 2012: Ocean wind speed retrieval algorithm using the frequency 36 GHz vertical/horizontal and 6 GHz horizontal data of the Advanced Microwave Scanning Radiometer (AMSR). Italian J. Remote Sensing, 45: 133-140.

Wentz, F. J. (1983): A model function for ocean microwave brightness temperatures. J. Geophys. Res., 88(C3), 1892 1908.

Chapter 8.

Description of the GOSAT-GW AMSR3 Sea Ice Concentration Algorithm

Algorithm developers:

Josefino C. Comiso

Goddard Space Flight Center
National Aeronautics and Space Administration

Kohei Cho

Tokai University

1. Introduction

Sea ice concentration is a key indicator of the Earth's climate system, governing exchanges of heat, momentum, and freshwater between the ocean and atmosphere. It directly affects ocean circulation, surface albedo, and ecosystem productivity, while also serving as a sensitive marker of climate change. Accurate and consistent sea ice concentration products are therefore essential for monitoring long-term variability, detecting trends, and supporting environmental, operational, and policy applications in polar regions.

2. Algorithm description

The Sea Ice Concentration product, one of the AMSR3 standard products, is generated using Bootstrap algorithm as same as AMSR2. For details, please refer to the document (Comiso and Cho, 2012). The O-point in the sea ice concentration retrieval algorithm was replaced with a dynamic tie point (Comiso *et al*., 2017), and an AMSR2 weather filter was applied to enhance the retrieval accuracy (Cho and Naoki, 2023).

3. Validation concept

The validation of sea ice concentration will be conducted through comparisons with optical sensors such as MODIS, VIIRS or SGLI. High-resolution imagery obtained from optical sensors will be used to determine the presence or absence of sea ice, and sea ice concentration data corresponding to the AMSR3 observation footprint will be generated. The evaluation will be performed for each concentration level, including assessments of spatiotemporal consistency and validity.

Reference

Comiso, J. C. and K. Cho, 2012: Description of GCOM-W1 AMSR2 Sea Ice Concentration Algorithm, *Description of GCOM-W1 AMSR2 Level 1R and Level 2 Algorithms*, 6-1-6-28.

Comiso, J. C., W. N. Meier, and R. Gersten, 2017: Variability and trends in the Arctic Sea ice cover: Results from different techniques, *J. Geophys. Res. Oceans*, **122**, 6883–6900, doi:10.1002/2017JC012768.

Cho, K. and K. Naoki, 2023: A New weather filter for reducing weather effect in calculating sea ice concentration from AMSR2 data., *ISPRS Annals of the Photogrammetry, Remote Sensing and Spatial Information Sciences*, **X-1/W1-2023,** 793-798, doi:10.5194/isprs-annals-X-1-W1-2023-793-2023.

Chapter 9.

Description of the GOSAT-GW AMSR3 High Resolution Sea Ice Concentration Algorithm

Algorithm developer:

Gunner Spreen

Bremen University

1. Introduction

Sea ice concentration is a key indicator of the Earth's climate system, governing exchanges of heat, momentum, and freshwater between the ocean and atmosphere. It directly affects ocean circulation, surface albedo, and ecosystem productivity, while also serving as a sensitive marker of climate change. In this context, high-resolution sea ice concentration are particularly important for resolving fine-scale spatial variability, coastal processes, and marginal ice zone dynamics that cannot be captured by conventional passive microwave products. Accurate and consistent sea ice concentration products are therefore essential for monitoring long-term variability, detecting trends, and supporting environmental, operational, and policy applications in polar regions.

2. Algorithm description

The High-Resolution Sea Ice Concentration product, one of the AMSR3 standard products, is generated using the arctic radiation and turbulence interaction study (ARTIST) sea ice (ASI) algorithm utilizes the polarization difference of brightness temperatures at nearly 90 GHz. Granted by the high spatial resolution (4 km × 6 km) of the 89 GHz channels of the advanced microwave scanning radiometer such as AMSR series sensors. For details, please refer to the paper (Gunner *et al.*, 2005).

3. Validation concept

The validation of sea ice concentration will be conducted through comparisons with optical sensors such as MODIS, VIIRS or SGLI. High-resolution imagery obtained from optical sensors will be used to determine the presence or absence of sea ice, and sea ice concentration data corresponding to the AMSR3 observation footprint will be generated. The evaluation will be performed for each concentration level, including assessments of spatiotemporal consistency and validity.

Reference

Spreen, G., L. Kaleschke, and G. Heygster, 2005: Sea ice remote sensing using AMSR-E 89-GHz channels, *J. Geophys. Res.: Oceans*, **113**, C02S03, doi:10.1029/2005JC003384.

Chapter 10.

Description of the GOSAT-GW AMSR3 Snow Depth Algorithm

Algorithm developer:

Richard Kelly

University of Waterloo

1. Introduction

Snow depth is a fundamental variable in the Earth's climate system, playing a critical role in regulating land–atmosphere energy exchanges, hydrological processes, and ecosystem dynamics. As an effective thermal insulator, snow modulates soil temperature and permafrost stability, while its high albedo significantly influences the surface radiation budget. Moreover, snow depth determines the timing and magnitude of snowmelt runoff, which is essential for freshwater availability, river discharge, and water resource management in many regions. It also affects vegetation growth cycles and wildlife habitats, particularly in high-latitude and mountainous environments. Importantly, snow depth exhibits strong spatial and temporal variability, making continuous and large-scale observations indispensable for understanding climate variability and change. Long-term, consistent satellite-based records, such as those provided by passive microwave sensors including AMSR2, are therefore crucial for monitoring regional to global patterns of snow accumulation. These observations enable improved assessment of interannual variability, long-term trends, and their linkage to atmospheric circulation and climate change.

2. Algorithm description

The Snow depth product, one of the AMSR3 standard products, is generated using the Satellite-Based Microwave Snow Algorithm (SMSA) algorithm. This algorithm improved snow depth (SD) retrieval approach that builds on advances in microwave radiative transfer modeling and observational understanding over the past 15 years. The algorithm integrates three key developments: an enhanced snow detection scheme for more accurate discrimination of snow-covered conditions, an improved forest attenuation correction based on forest transmissivity to better account for vegetation effects, and a physically based SD retrieval method using a parsimonious implementation of the Dense Media Radiative Transfer (DMRT) model. For details, please refer to the paper (Kelly *et al.*, 2019).

3. Validation concept

In the validation of snow depth products, it is essential to consider the influence of the following four factors:

① Discrimination between snow-covered and snow-free areas

Snow cover is a seasonal variable, and its presence or absence is itself an important hydrological indicator. In cold regions, frozen soil is often misclassified as snow, leading to significant errors in snow depth retrievals. Therefore, accurate discrimination between snow-covered and snow-free conditions is critical from both validation and algorithm development perspectives.

② Diversity of snow conditions (grain size and stratigraphy)

Snow metamorphism alters grain size and layer structure, which strongly affects microwave radiative transfer properties. Consequently, validation must be conducted under a range of snow conditions that exhibit different scattering and emission characteristics.

③ Microwave properties of the underlying soil

The emission and scattering properties of the soil beneath the snowpack provide boundary conditions for microwave radiative transfer within the snow layer. These conditions vary significantly depending on whether the ground is frozen, undergoing surface melt, or unfrozen beneath the snowpack. Therefore, validation must account for variations in subsurface conditions under diverse snow environments.

④ Vegetation conditions (biomass, type, canopy snow, and heterogeneity)

The distribution of water within vegetation—including biomass, structural characteristics of leaves and trunks, snow accumulation in the canopy, and spatial heterogeneity within the footprint—has a substantial impact on microwave radiative transfer. Thus, validation must consider different vegetation conditions in combination with varying snow and soil environments described above.

To enable validation under the conditions described above, long-term observational datasets across diverse climate regimes are utilized. Validation is conducted over extended periods under varying meteorological conditions, vegetation types, snow characteristics, and soil states.

Reference

Kelly, R., Q. Li and N. Saberi, 2019: The AMSR2 Satellite-Based Microwave Snow Algorithm (SMSA): A New Algorithm for Estimating Global Snow Accumulation, *IGARSS 2019 - 2019 IEEE International Geoscience and Remote Sensing Symposium, Yokohama, Japan, 2019*, pp. 5606-5609, doi: 10.1109/IGARSS.2019.8898525.

Chapter 11.

Description of the GOSAT-GW AMSR3 Soil Moisture Algorithm

Algorithm developer:

Hideyuki Fujii

RESTEC

Prepared by JAXA/EORC

The soil moisture product, one of the AMSR3 standard products, is generated using algorithm version 6. This algorithm was previously used to generate the research product for AMSR2. For details, please refer to the paper below.

Reference: Hideyuki FUJII, Toshio KOIKE, Keiji IMAOKA, Improvement of the AMSR-E Algorithm for Soil Moisture Estimation by Introducing a Fractional Vegetation Coverage Dataset Derived from MODIS Data, Journal of The Remote Sensing Society of Japan, 2009, Volume 29, Issue 1, Pages 282-292, Released on J-STAGE September 01, 2009, Online ISSN 1883-1184, Print ISSN 0289-7911

DOI: https://doi.org/10.11440/rssj.29.282

URL: https://www.jstage.jst.go.jp/article/rssj/29/1/29_1_282/_article/-char/en

Abstract:

Soil moisture is an important component of the hydrology of land surfaces. Accurate monitoring of soil moisture is essential in understanding energy and water cycles and ecological system processes. Microwave remote sensing using satellites is an effective method for collecting global information on land surface hydrology. In this study, the soil moisture algorithm of Koike et al. was revised by focusing on the vegetation component, with the goal of improving the accuracy of the soil moisture product of the Advanced Microwave Scanning Radiometer for the Earth Observing System mounted on the satellite Aqua.

The water content of vegetation affects the sensitivity of the microwave remote sensing of soil moisture. In the Koike algorithm, a semi-empirical vegetation model with the assumption of uniform vegetation coverage was used to evaluate the vegetation effects on the retrieval of soil moisture data. However, satellite microwave radiometer observations have large footprints of several tens of kilometers. There are few land surface regions in the world that are uniformly covered with vegetation at this scale. The results of ground-based experiments demonstrated that non-uniformities in the vegetation coverage have very large effects on horizontally polarized waves. We therefore created a global fractional vegetation coverage dataset from the data gathered by the Moderate Resolution Imaging Spectroradiometer, and attempted to incorporate this into the algorithm. In addition, model parameters in the semi-empirical vegetation model were replaced on the basis of a ground-based experiment.

The results were verified by the comparison of estimated and measured data for three locations with differing vegetation coverage conditions. Compared with results estimated by the Japan Aerospace Exploration Agency standard product version 5 (created by the algorithm before the current revision), the results estimated by the revised algorithm showed a significant improvement in accuracy and reduction in the number of erroneous estimations.

Chapter 12.

Description of GOSAT-GW/AMSR3

Sea Ice Motion Vector Retrieval Algorithm

Eri Yoshizawa
Japan Aerospace Exploration Agency
Earth Observation Research Center

Koji Shimada
Tokyo University of Marine Science and Technology

Table of Contents

1. Introduction 12-3
2. Algorithm description 12-3
3. Algorithm Implementation 12-4
   3.1 Implementation 12-4
   3.2 Input parameters 12-4
   3.3 Output parameters 12-5
   3.4 Ancillary data 12-5
   3.5 Processing flow 12-6
4. Validation Concept 12-9
References 12-10

1. Introduction

This document describes the algorithm and its validation concept for retrieving sea ice motion vectors, which are standard products derived from observation data acquired by the Advanced Microwave Scanning Radiometer 3 (AMSR3) onboard the Global Observing SATellite for Greenhouse gases and Water cycle (GOSAT-GW).

Sea ice motion vectors represent the displacement of sea ice that mediates interactions between the atmosphere and the ocean, and they constitute an essential variable for quantifying atmosphere–ocean kinematic interactions specific to polar oceans. Measurements by microwave radiometers such as AMSRs, owing to their all-weather capability and their ability to provide daily coverage of the entire Arctic and Antarctic Oceans, represent the only means of routinely acquiring gridded vector fields over these regions. Furthermore, compared with other similar radiometers, AMSRs offer the advantage of higher spatial resolution, which contributes to improving the velocity resolution of the retrieved motion vectors.

To exploit these advantages of AMSRs and to retrieve highly accurate sea ice motion vector data, an algorithm based on the Particle Image Velocimetry (PIV) method—an image correlation–based motion tracking technique applied to temporally consecutive images (see Raffel et al., 2016 for a review)—was developed (Yoshizawa et al., 2023). This document provides an overview of the algorithm, including several modifications introduced to adapt it for implementation within the GOSAT-GW/AMSR3 Mission Operation System (MOS).

2. Algorithm description

Sea-ice displacement is estimated by applying a cross-correlation-based motion tracking technique to pairs of successive daily brightness temperature images. The estimated displacement is subsequently converted into a velocity vector by dividing it by the temporal interval between the image pair. Let the pixel length be denoted by l, the search area length by L, and the time separation between paired images by Δt. Under these definitions, the dynamic range of the retrievable velocity components is dictated by these parameters: the lower bound is given by $l/\Delta t$, while the upper bound is determined by $L/\Delta t$. These bounds define the slowest and fastest detectable components of sea-ice motion, respectively.

When daily retrievals are performed at the spatial resolution of a microwave radiometer, the lower bound of the dynamic range is constrained from several kilometers per day (on the order of 10^{-2} m s^{-1}) to several tens of kilometers per day (on the order of 10^{-1} m s^{-1}). In contrast, sea-ice velocity is empirically known to be on the order of a few percent of the surface wind speed, which is itself on the order of 10 m/s. Therefore, improving retrieval accuracy requires lowering the minimum detectable velocity, i.e., reducing the lower bound of the dynamic range.

To this end, the algorithm is designed to make effective use of motion vector candidates derived from

the 89-GHz channel, which, among the channels sensitive to the Earth's surface, provides images with the highest spatial resolution. However, the 89-GHz channel exhibits high sensitivity to atmospheric water vapor, and the resulting brightness temperature images often contain mixed signals from sea ice and overlying clouds. This characteristic leads to the generation of multiple candidate motion vectors and makes it difficult to identify a physically plausible solution based solely on the cross-correlation coefficient.

To address this limitation, the algorithm also performs motion tracking using the 37-GHz and 19-GHz channels, which are less sensitive to atmospheric water vapor. The multiple candidate vectors obtained from these frequencies are subjected to a screening process to remove outliers based on comparisons with objective analysis surface wind fields and consistency checks with neighboring candidate vectors. This process yields a reference vector field, which serves as a basis for selecting physically reasonable solutions. For each pixel, the candidate motion vector that is closest to the reference vector is selected as the valid sea-ice motion vector. In total, 54 candidate vectors are generated and evaluated at each pixel, derived from combinations of three frequencies, two polarizations, three template sizes, and the top three ranked cross-correlation peaks.

Although Yoshizawa et al. (2023) describe the application of the algorithm to the Arctic Ocean, essentially the same algorithm is applied to the Southern Ocean. However, in the Antarctic region, where divergent motion fields frequently develop due to katabatic winds, filtering based on surface wind fields is applied with relaxed constraints to accommodate these region-specific dynamical characteristics.

3. Algorithm Implementation

3.1 Implementation

The algorithm is implemented in the GOSAT-GW/AMSR3 MOS and is operated in near–real–time. In addition, quality flags indicating retrieval reliability are provided based on the selection process of motion vector candidates. The daily sea ice motion vector products with a 50-km resolution are generated for both Northern and Southern Hemispheres and are gridded onto polar stereographic coordinates. The generation of products mapped onto the Equal-Area Scalable Earth Grid (EASE-Grid) is currently under consideration and coordination.

3.2 Input parameters

Level-1B brightness temperatures measured by the AMSR3 89-, 37-, and 19-GHz channels with horizontal and vertical polarizations are used as input parameters to the algorithm. These data are internally projected onto a polar stereographic grid with a spatial resolution of 5 km, and the resulting brightness temperature images are used for cross-correlation–based motion tracking. Both ascending and descending data from 00:00–23:59 UTC are used to create daily images. Motion tracking is

performed only for 50-km templates fully composed of pixels with sea-ice concentration equal or greater than 15%. This condition is determined using sea-ice concentration information that is upscaled from Level-3 sea-ice concentration products with a spatial resolution of 10 km.

3.3 Output parameters

In addition to the u and v components defined in the polar stereographic x–y coordinate system, the algorithm outputs the corresponding eastward and northward velocity components, obtained through coordinate transformation. These variables are provided as separate fields in the NetCDF product.
The NetCDF product also includes quality flags that describe the characteristics of the retrieved sea-ice motion vectors. For 50-km templates identified as sea-ice areas based on sea-ice concentration thresholds, the quality flags encode which frequency channel (89, 37, or 19 GHz) contributed the selected motion vector candidate. In addition, flags are used to indicate cases where no optimal candidate was available, distinguishing whether the stored value was derived through interpolation or extrapolation. Grid points corresponding to the open ocean, land areas, or regions outside the predefined latitude limits for the Northern and Southern Hemispheres, respectively, are assigned missing values in the NetCDF output.

3.4 Ancillary data

The 10-m wind fields from the Japan Meteorological Agency global atmospheric analysis are used as ancillary data for screening erroneous motion vector candidates.

3.5 Processing flow

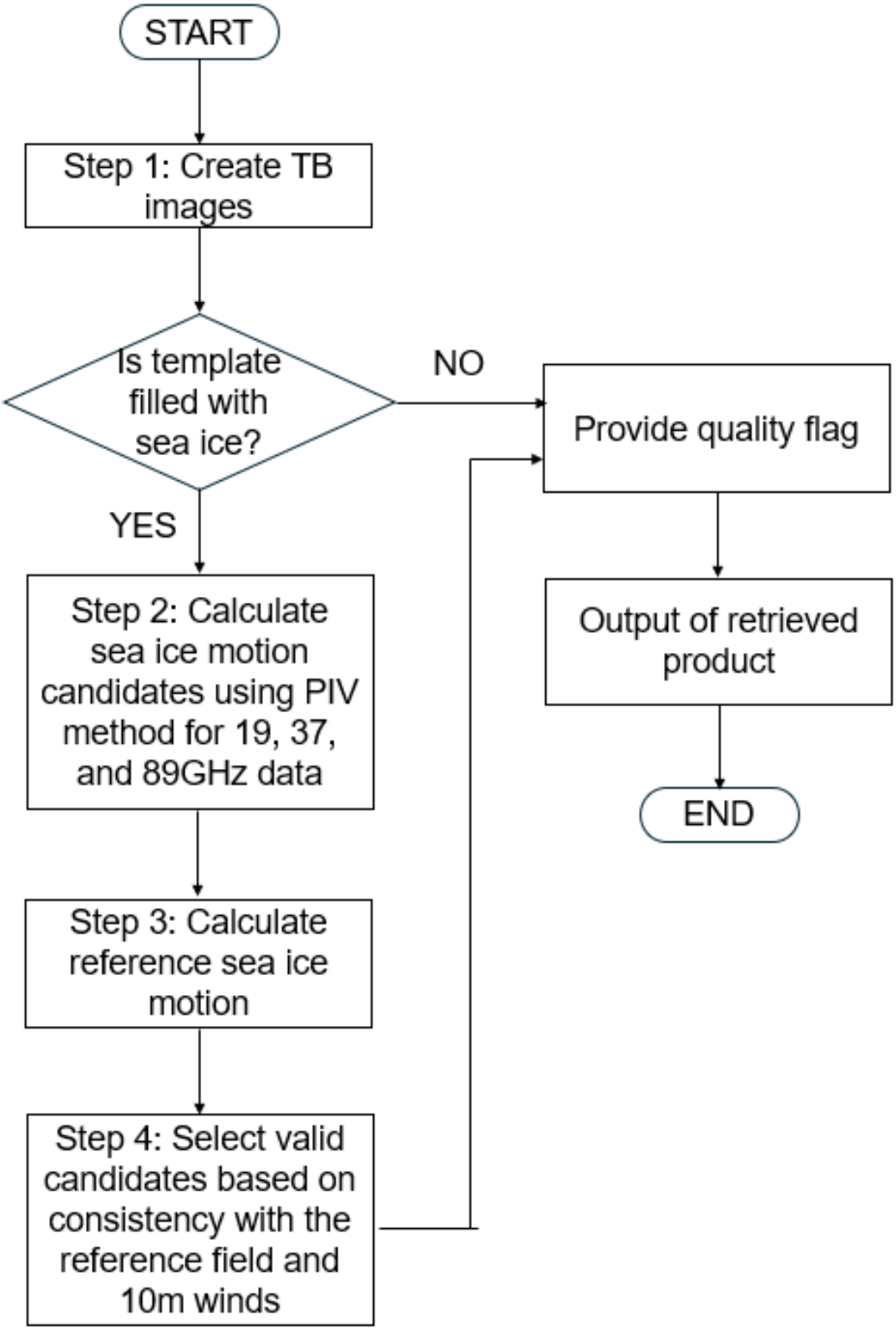

Figure 1. Schematic diagram of sea ice motion vector retrieval algorithm

3.6 Example output

Figure 2 shows sample sea ice motion vector fields for the Northern and Southern Hemispheres projected onto polar stereographic coordinates. In the Arctic Ocean, the anticlockwise sea ice circulation is clearly captured in the central Arctic (upper panel). In the Southern Ocean, the vector fields demonstrate the dominance of offshore sea ice motion in the Weddell Sea and anticyclonic circulation in the Ross Sea (lower panel).

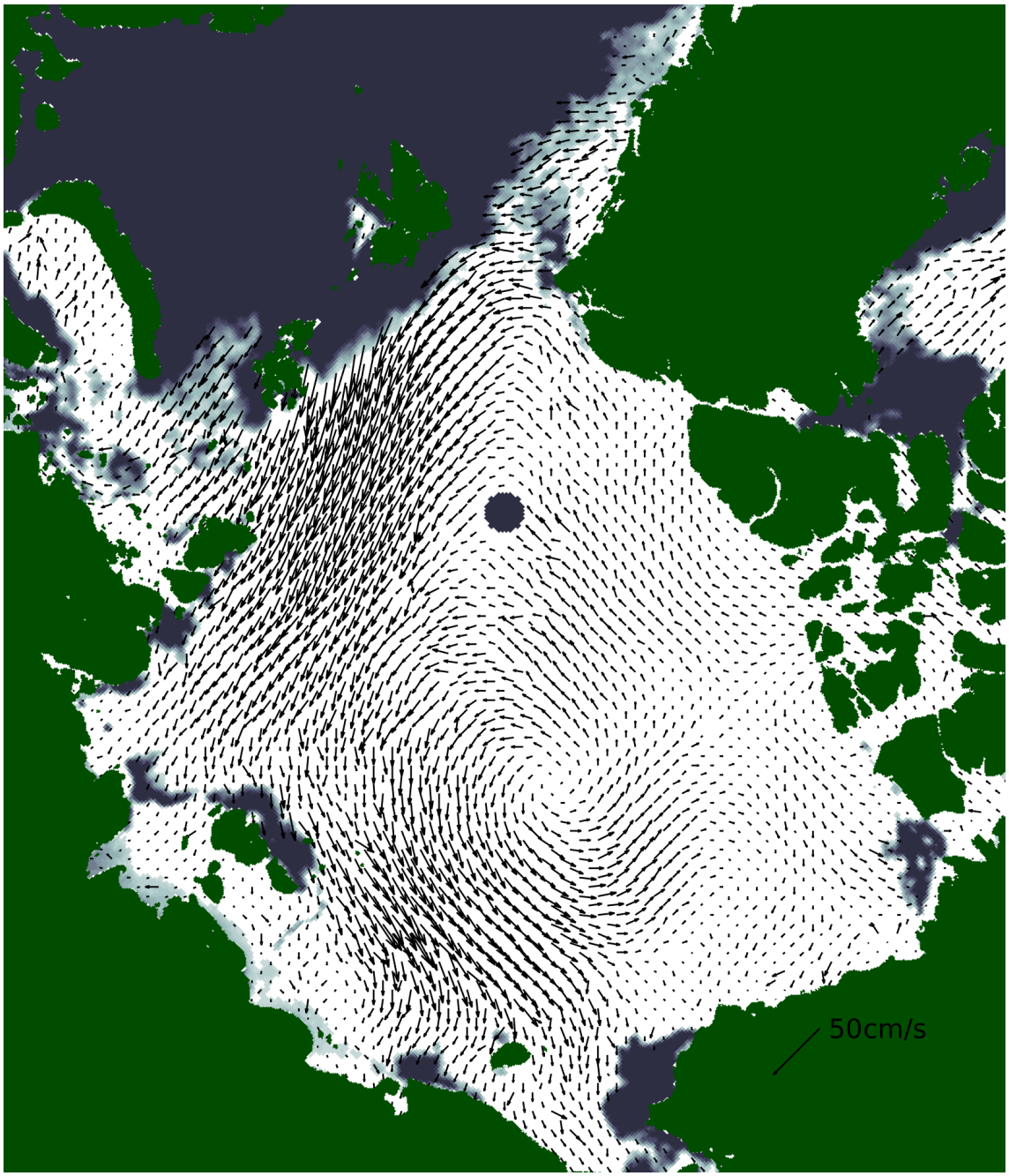

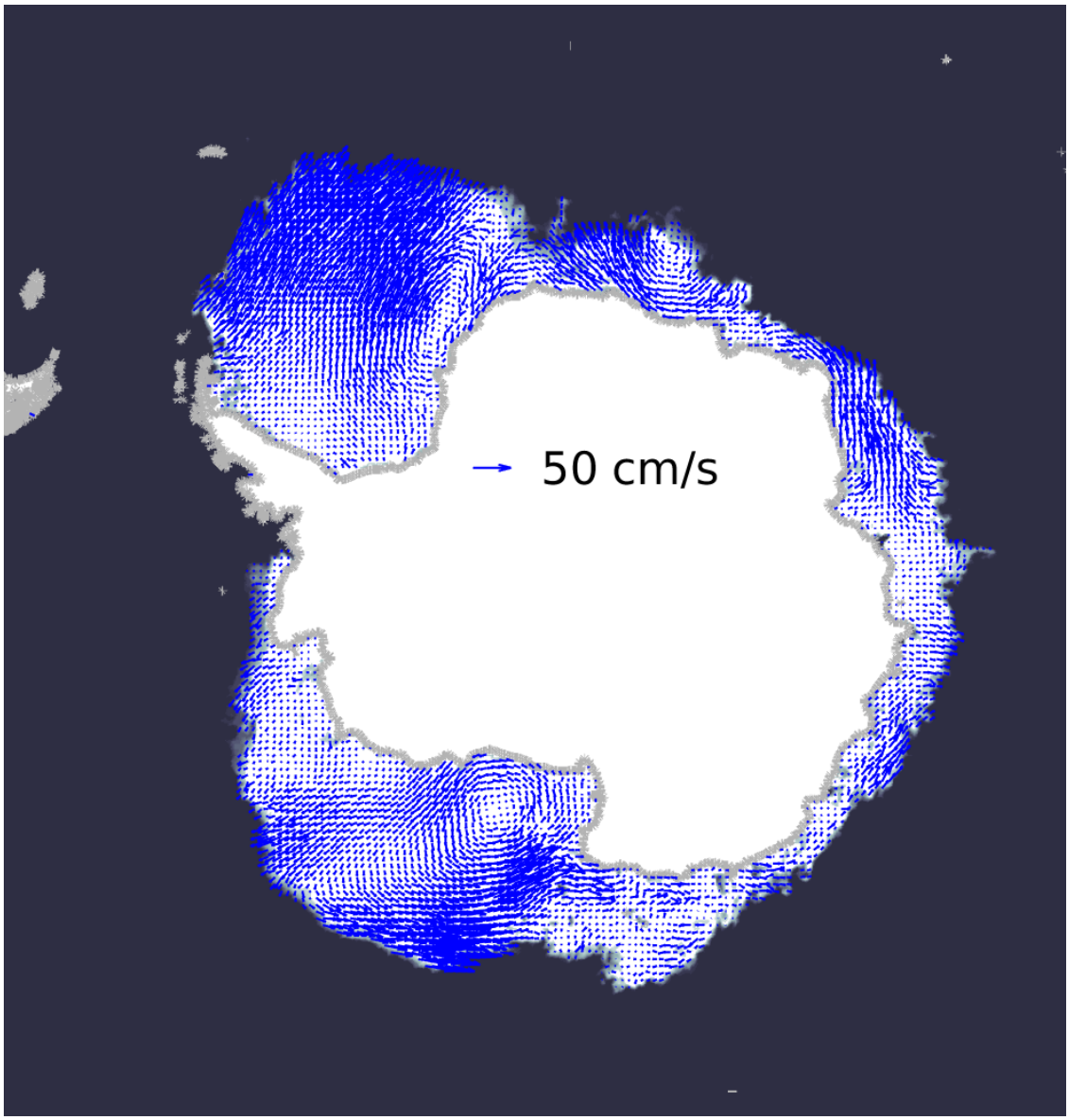

Figure 2 Sea ice motion vector fields in the (upper) Northern Hemisphere and (lower) Southern Hemisphere on June 8, 2026, with sea ice concentrations averaged over June 7-8, 2026.

3.7 Limitation

The retrieval accuracy of sea-ice motion vectors generally degrades during summer compared to winter. This is primarily because changes in brightness temperature pixel arrays over the temporal interval Δt, caused by surface melt–refreeze processes and increased sea-ice mobility, make it more difficult to identify well-matched patterns in the cross-correlation analysis. For similar reasons, retrieval accuracy may also be reduced in the vicinity of the ice edge, where rapid changes in surface conditions and ice mobility frequently occur regardless of the season. In addition, within this algorithm, values assigned near the ice edge are, in many cases, derived through extrapolation, which can further contribute to increased uncertainty in the retrieved vectors.

Furthermore, the dominance of physical processes that cannot be adequately resolved with daily temporal sampling may further degrade retrieval accuracy. For example, the increasing amplitude of sea-ice inertial oscillations observed over the past two decades (Gimbert et al., 2012, Yuan et al., 2023), represents one of the potential factors contributing to reduced performance of the daily sea-ice motion retrieval.

Finally, we note an important limitation related to cases in which observations are largely missing on a per-orbit (pass) basis. The present algorithm is developed under the assumption that brightness temperature images covering the pan-Arctic/Antarctic are provided without large-scale data gaps. Consequently, on days immediately before and after an orbit-level data loss (which occurs only rarely), erroneous values may appear in the surrounding regions that cannot be identified by the quality flag. Although these erroneous values are expected to be reduced in future versions of the algorithm, users are advised at present to exercise caution when using the product for periods adjacent to days on which the Level-1B product is missing, as indicated by the product data-gap information on the G-Portal.

4. Validation Concept

In situ buoy observations provided for both Arctic and Antarctic Oceans from the International Arctic Buoy Program (IABP) (https://iabp.apl.uw.edu/WebData/, accessed on 15 May 2026) are used as reference data for product validation. The buoy observations provide positional information from which sea ice velocities are derived. However, these data are recorded at irregular time intervals and are affected by GPS-related uncertainties, which can introduce errors in velocity estimation. To ensure the reliability of the in situ reference velocities, a quality control and averaging procedure is applied as described below.

First, the raw latitude and longitude coordinates from the IABP are screened to remove duplicated records with identical or nearly identical timestamps. Horizontal velocity components (u and v) are then calculated using central differencing of the x and y positions over the original observation time intervals. Any velocity component exceeding 2 m s^{-1} is regarded as erroneous; in such cases, the corresponding x and y position samples are considered unrealistic and are excluded from further analysis. The remaining data are subsequently resampled at 3-hour intervals, and daily in situ velocities are calculated as averages over a ±12 h window centered at 00:00 UTC. The corresponding daily eastward and northward velocity components are also calculated.

The validated daily in situ position and velocity data are then matched with satellite-derived sea ice motion vectors. For each daily in situ reference data point, the nearest satellite grid cell is selected. For every matchup, the spatial separation between the in situ reference position and the satellite grid point, as well as the temporal difference between the satellite overpass time and the in situ reference time, are recorded. Statistical analyses are performed by conditioning the matchup samples on both spatial and temporal separations.

It should be noted that the reference time of the in situ buoy data is fixed uniformly at 00:00 UTC, independent of geographic location, whereas the observation time of the satellite data, expressed in UTC, depends on longitude because AMSR3 observations are acquired at orbit-dependent overpass times and vary slightly depending on the repeat cycle of the orbit. As a result, the time difference in UTC between the in situ reference data and the satellite observations varies systematically with longitude, becoming relatively small in some longitude bands and larger in others.

In this study, such regional characteristics in temporal mismatch are not explicitly considered. Instead, a uniform temporal difference threshold of ±6 h is applied globally so that matchups can be consistently defined and retained across all ocean regions. Accordingly, validation is performed using matchups within a 25-km spatial radius and within a ±6 h time difference.

References

Gimbert, F., D. Marsan, J. Weiss, N. C. Jourdain, and B. Barnier (2012): Sea ice inertial oscillations in the Arctic Basin. The Cryosphere, 6, 1187–1201. https://doi.org/10.5194/tc-6-1187-2012

Raffel, M., C. J. Kähler, C. E. Willert, S. T. Wereley, F. Scarano, and J. Kompenhans (2018): Particle Image Velocimetry: A Practical Guide (3rd ed.). Springer. https://doi.org/10.1007/978-3-319-68852-7

Yoshizawa, E., et al. (2023): Sea Ice Motion Vector Retrievals from AMSR2 89-GHz Data: Validation Algorithm with Simultaneous Multichannel Observations. Journal of Atmospheric and Oceanic Technology. https://doi.org/10.1175/JTECH-D-22-0049.1

Yuan, D., Z. Hao, J. You, P. Zhang, B. Yin, Q. Li, and Z. Xu (2023): Enhancing Sea Ice Inertial Oscillations in the Arctic Ocean between 1979 and 2019. Water, 15(1), 152. https://doi.org/10.3390/w15010152